國 立 交 通 大 學
電 子 物 理 系
博 士 論 文

兆赫輻射波的產生與應用於釔鋇銅氧超導薄膜
特性之研究

Generation and Application of Terahertz Radiation in

Superconducting YBa$_2$Cu$_3$O$_{7-\delta}$ Thin Films

研 究 生 ： 林博瑛

指導教授 ： 吳光雄 教授

中華民國九十三年十月

兆赫輻射波的產生與應用於釔鋇銅氧超導薄膜

特性之研究

Generation and Application of Terahertz Radiation in

Superconducting YBa$_2$Cu$_3$O$_{7-\delta}$ Thin Films

研 究 生 ： 林博瑛　　　　　　　Student : Po-Iem Lin

指導教授 ： 吳光雄 教授　　　　　Advisor : Prof. Kaung-Hsiung Wu

國 立 交 通 大 學

電 子 物 理 系

博 士 論 文

A Dissertation
Submitted to Department of Electrophysics
College of Science
National Chiao Tung University
in Partial Fulfillment of the Requirements
for the Degree of
Doctor of Philosophy
in
Electrophysics
October 2004
Hsinchu, Taiwan.

中華民國 93 年 10 月

兆赫輻射波的產生與應用於釔鋇銅氧超導薄膜特性之研究

研 究 生：林博瑛　　　　　　　　指導教授：吳光雄 教授

國 立 交 通 大 學

電 子 物 理 系

中 文 摘 要

在本論文中，我們研究利用飛秒級超快雷射光激發半導體或高溫超導體製作光致兆赫茲輻射脈衝產生源，且在國內外首次利用自由空間電光取樣技術量取高溫超導薄膜在以飛秒脈衝雷射激發下，產生之兆赫茲電磁輻射波的時域暫態波形。另外，由已建立之兆赫茲時域頻譜量測分析技術，研究氧化物薄膜與基板材料在兆赫茲波段之時域頻譜，以瞭解材料在此波段下之高頻電磁特性。

將半絕緣性之砷化鎵半導體微影蝕刻，鍍金後成為光導開關，在外加偏壓下此光導開關受雷射光激發後，由於光電流隨時間的瞬變，將產生高頻之兆赫茲輻射波，藉由利用自由空間電光取樣技術可將此高頻輻射波形完整取出，經由快速傳力葉轉換可得一輻射頻譜分佈。從改變不同的操作條件，我們已完整的研究分析利用半導體產生

兆赫茲輻射。利用不同的外加偏壓、超快雷射光的能量密度與光導開關的孔隙大小，皆可獲得相同的兆赫茲輻射波形輸出。其頻率介於 dc 至 3 THz 之間。由此可知，利用光激發半導體產生高頻之兆赫茲輻射波的輻射機制在上述之操作條件下是一致的。

在偵測方式上，我們以厚度 1 釐米的 ZnTe(110)電光晶體為偵測器來感應兆赫茲輻射訊號。作用在 ZnTe 晶體上之兆赫茲輻射電場強度與差分後之光電二極體所讀取到的信號有關。在我們的系統中，兆赫茲輻射與探測光沿 ZnTe(110)面的法線分向傳播。隨著改變兆赫茲輻射電場與探測光的偏振方向相對於晶體的 z 軸之夾角時，輻射場強度大小和時域暫態波形的極性方向將會改變。當兆赫茲輻射電場與探測光的偏振方向皆垂直於晶體的 z 軸時，可偵測到最大的強度值。

我們完成以釔鋇銅氧高溫超導薄膜作兆赫茲輻射源的特性量測，包括改變不同雷射光能量、不同外加偏電流及不同量測溫度下之兆赫茲時域瞬變波形。另外，薄膜在超導態時，超導載子會因外受輻射光下，引起薄膜本身感應係數的變化，使得原來入射之輻射時域波形會有再成形的現象。藉由適當的轉換函數，可模擬出輻射時域波形的變化，並與實驗數據結果相符合。由結果顯示，光致超導體泰拉赫茲輻射的機制是來自於超導電流密度隨時間的調變，從這些時間解析量測所獲得的兆赫茲瞬間電場輻射波形，可以觀察到載子在非平衡狀

態下的動力行為。在超快雷射光激發下，超導電流密度變化量會先減少，持續時間約為 1.0 ps；接續，超導電流密度變化量開始回升，持續時間約為 2.5 ps，此回復時間大小和超導能隙是相關的。

　　另外，我們將使用半導體材料來產生兆赫茲輻射源，並且從已建立之兆赫茲時域頻譜量測分析技術，研究氧化物薄膜與基板材料在兆赫茲波段下之高頻電磁特性。利用量測結果與理論的分析比較，可以獲到溫度與頻率相關之薄膜與基板材料之複數折射率，並進一步地求得氧化物薄膜之介電係數、光導係數、穿透深度、準粒子的散射時間等隨溫度、頻率的變化情形。

Generation and Application of Terahertz Radiation in Superconducting YBa$_2$Cu$_3$O$_{7-\delta}$ Thin Films

Student : Po-Iem Lin   Advisor : Prof. Kaung-Hsiung Wu

Department of Electrophysics

National Chiao Tung University

ABSTRACT

In this dissertation, three major parts are included. First, the observation of terahertz generation and detection from current-biased superconducting YBCO thin films excited by femtosecond optical pulses by using a free-space electro-optic sampling (FSEOS) technique is reported. The transient terahertz pulse was found to originate from the nonequilibrium superconductivity. Secondary, we also carried out systematic comparisons between the emissions generated with different operating parameters when using the semiconducting photoconductive switches as radiation source. Lastly, in relation to terahertz applications, we studied the terahertz frequency response in superconducting YBCO thin films by carrying out the terahertz time-domain spectroscopy (THz-TDS) measurements.

The characteristics of optically induced bipolar terahertz radiation in biased photoconductive switches and the emitted frequency spectrum distribution were found to remain unchanged even when the optical excitation fluence, strength of the biased field and the emitter gap spacing were varied. This suggests that the terahertz radiation obtained in the current setup must have originated from the same mechanism

which is believed to be associated with the ultrafast charge transport process during pulsed laser illumination.

On the other hand, the efficiency of terahertz detection strongly depends on the orientation of the terahertz polarization with respect to the ZnTe crystal (001) axis and on the angle between the polarization of the probe beam and that of the terahertz radiation. These results give the optimal operating parameters for terahertz pulse detection using the ZnTe sensor crystal.

The origin of photogenerated terahertz radiation pulse emitted from current-biased superconducting YBCO thin films excited by femtosecond optical laser pulses is delineated using a FSEOS technique. Picosecond electromagnetic pulses about 450 fs wide were obtained. The frequency spectrum derived by Fourier transforming the picosecond pulses spans over 0.1-4 THz. By investigating the performances of the transient terahertz radiation generated under different operating parameters, pulse reshaping in the measured terahertz electric field caused by the kinetic inductance of the superconducting charge carriers is identified. After recovering the original waveforms of the emitted terahertz pulses, the transient supercurrent density directly correlated to the optically excited quasiparticle dynamics is obtained. A fast decreasing component of about 1.0 ps and a slower recovery process with a value of 2.5 ps are unambiguously delineated in the optically induced supercurrent modulation. The radiation mechanism of the transient terahertz pulse related to nonequilibrium superconductivity is discussed.

Finally, we have used the established coherent terahertz time-domain spectroscopy technique to investigate the properties of the electrodynamics of

superconductor at terahertz frequencies. The temperature and frequency-dependent complex index of refraction of the materials, such as NdGaO$_3$ substrate and YBCO thin films, were determined by analyzing the complex transmittance. We used these analysis to explain the variation of the amplitude and phase of pulse shape of terahertz generation in current-biased YBCO thin film a FSEOS technique, and in observing the effect of pulse reshaping of terahertz transmission in YBCO thin films detected in the THz-TDS measurements. The temperature dependence of the real component of complex conductivity revealed a large broad peak over the whole measured terahertz range. It is attributed to a competition between an increase in the normal carrier relaxation time and a decrease in the number of normal carriers with decreasing temperature below *Tc*. By fitting the measured complex optical conductivity $\sigma(\omega,T)$ with the aid of a two-fluid model, we were able to extract the temperature dependent of the London penetration depth $\lambda_L(T)$ and the temperature dependence of quasiparticle scattering rate $1/\tau(T)$.
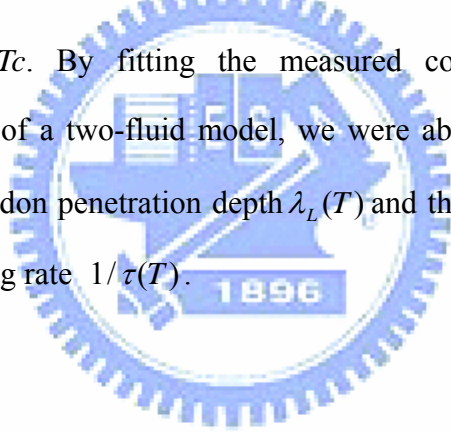
致　謝

　　論文能夠順利完成，要感謝的人太多太多了。有大家的幫忙與扶持，才會有今天的表現。首先要感謝指導老師吳光雄教授及研究群莊振益教授、林俊源教授、溫增明教授、郭義雄教授耐心的指導與栽培。

　　另外，非常感謝口試委員清華大學齊正中教授、交通大學潘犀靈教授、清華大學洪勝富教授以及中山大學周雄教授的指導與肯定。

　　實驗室裡裏的伙伴們，大家就像是一家人。雖然來自不同的地方，卻是有緣共同在這兒相聚，名為"固態實驗室"。由於彼此相互的扶持與勉勵，生活六年多以來的點點滴滴，不知不覺地在我的心中已然建造成一座城堡。老師們的指導與教誨漸漸地使我成長與茁壯。在此感謝德峻學長、世溥學長、中裕學長、慧愷學長、旭禎學長、世烽學長們在研究及生活上的相助與關懷。有志偉學弟的合作，使得超快雷射光譜實驗室有了初步的雛型及成果。志昌學弟、璨耀學弟、維仁學弟們如兄弟般的情感，義氣當頭，為了共同的目標而努力。感謝新山、雯妃、家汶、宜蓁、美杏學弟妹們在實驗上的討論與幫忙。良星、彥瑞、佩君、峙文、育全、維娟、瓊絹、東漢、沛宏、俐君、伯宗學弟妹們，有你們相伴，為我的研究生涯增添色彩。

　　感謝珮雯多年來的體貼與照顧。在完成論文研究的這段時光，最需感謝的是青慧的鼓勵，有妳的陪伴，讓我心中充滿了勇氣去面對未來。最後感謝的是我最親愛的爸媽及兄弟們，有你們的支持與照顧，一路走來，始終無悔。

Contents

Chapter 1

Introduction

Terahertz (THz) radiation, often called T-rays, loosely defined by the frequency range of 0.1 to 10 THz (10^{12} cycles per second), lies between infrared light and microwave radiation in the electromagnetic (EM) spectrum. There has been a revolution in terahertz systems in the past 20 years. Terahertz signals emanate from objects naturally, going through clothes, skin, plastics, cardboard, and semiconductors. Thus they enable a dizzying array of "X-ray vision" style application. For instance, terahertz signals naturally emanate from inside the human body, enabling X-ray-like imaging but without the side effects. What's more, a terahertz scan could simultaneously analyze tissues to pinpoint abnormalities, like skin cancer, in the resulting 3-D model. Owing to the advanced materials research provided new and high-power terahertz sources, and the potential of terahertz for advanced physics research and applications was demonstrated [1-3]. In this terahertz gap, the last frontier in the EM spectrum, neither optical nor silicon solutions exist today. Most broadband pulsed terahertz generation are based on the excitation of different materials with ultrafast laser pulses. Photoconductive switching and optical

rectification are two of the most common approaches for generating pulsed terahertz beams.

The photoconductive technique is based on using high-speed photoconductors as transient current sources for radiation antennas [4,5]. Typical photoconductors include high-resistivity GaAs, InP and radiation-damaged silicon wafers. Metallic electrodes are used to bias the photoconductive gap and form an antenna. The optical rectification approach using electro-optic crystals as rectification media [6,7] is based on the process of the electro-optic effect. There, materials like ZnTe, GaAs, GaP and organic crystal have been chosen as the nonlinear medium. Recently, photoresistive devices based on the transient supercurrent density in high-temperature superconductor have been explored by several groups and can be considered as a useful manner to probe the nonequilibrium superconductivity with the femtosecond time-resolved spectroscopy [8,9].

Coherent terahertz radiation emitted from biased photoconductive switches has been extensively investigated [4,5,10]. In general, the externally biased constant voltage drives the photogenerated carriers to form a transient photocurrent across the field region. A radiated terahertz electric field is obtained by the time derivative of the net current. It acts as the source term in Maxwell's equation, given as

$$\vec{E}_{THz} \propto \frac{\partial \vec{J}}{\partial t},$$
Eq. (1-1)

Terahertz emission from photoresistive devices, particularly, high-T_c superconductors (HTSC), $YBa_2Cu_3O_{7-\delta}$ (YBCO), has also been a topic of considerable attention. It is possible to characterize the dynamics of Cooper pairs breaking and recombination. Also, HTSC devices show promise as high-speed optical detectors. However, understanding on the relaxation of photoexcited quasiparticles is required. The observation and detection of terahertz pulses emitted from optically excited

superconducting bridges have further revived the interest of using HTSC films as potential terahertz radiation sources [8,9,11,12]. Unfortunately, the radiation mechanism of photogenerated terahertz radiation in YBCO so far is still obscure because it is largely inconsistent with the characteristics of optically excited quasiparticle dynamics obtained by femtosecond time-resolved spectroscopy [13,14].

For pulsed terahertz detection, photoconductive sampling and free-space electro-optic sampling are the two most common methods. Fundamentally, the electro-optic effect is a coupling between a low-frequency electric field (terahertz pulse) and a laser beam (optical pulse) in the sensor crystal. Using a (110)-oriented Zincblende crystal as a sensor crystal; this in turn modulates the polarization ellipticity of the optical probe beam passing through the crystal. It is based on the Pockels effect in which an applied voltage causes the sensor crystal to become birefringent. The ellipticity modulation of the optical beam can then be analyzed to provide information on both the amplitude and phase of the applied terahertz electric field. Photoconductive sampling is widely used for pulsed terahertz detection. A similar structure to the photoconductive switches, with a gap in the center, may be used. Rather than applying a bias voltage to the electrodes of the switches, the transient terahertz field itself provides the bias voltage. As applying the terahertz field on the gap, carriers will move from one side of the antenna to the other. Finally, the current amplifier and meter are used to measure the transient current. The material used for the antenna is typically radiation-damaged silicon-in-sapphire or LT-GaAs, and has a very short carrier lifetime.

One breakthrough came in the form of a technique known as terahertz time-domain spectroscopy (THz-TDS), which was developed at Bell Laboratories in Murray Hill, New Jersey, in the mid-1990. The terahertz temporal waveform transmitted through the sample, for example a fresh leaf, can be analyzed in real time

to provide the information of the material's characteristics [15]. Furthermore, THz-TDS allows a material's far-infrared optical properties to be determined as a function of frequency. The Drude model may then be used to link to the material free-carrier dynamic properties, including the plasma angular frequency and the damping rate. HTSC characterization is another important application in terahertz fields. Owing to its unique capacity in uncovering the nonequilibrium superconductivity, particularly in YBCO, has been a topic of considerable attention in understanding the relaxation of photoexcited quasiparticles [3]. A new type of terahertz radiation imaging has been proposed [16]. The supercurrent distributions were visualized by detecting the radiation from optically excited HTSC. In addition, in THz-TDS applications, the superconducting thin films have been analyzed to determine material parameters including the magnetic penetration depth and scattering rate [17,18].

In 1990, Han et al. and Eesley et al. discovered the femtosecond dynamics of photogenerated quasiparticles in $YBa_2Cu_3O_{7-\delta}$ superconducting thin films in femtosecond time-resolved spectroscopy measurements [19-22]. Two main dynamic processes are involved: one is the avalanche multiplication of quasiparticle following photon absorption and the other one is the recombination of the quasiparticles to form Cooper pairs [8,23,24]. Recently, Demsar and Mihailovic et al. [13] further demonstrated that the photogenerated transient reflectivity change also consists of two distinct characteristic relaxation times in the superconducting state. In that the fast component dominantly occurred in subpicosecond range appears to be insensitive to temperature while the slow component in the range of several picosecond usually diverges near Tc, displaying signature of an energy gap opening [25,26].

From the application point of view, the pico- to subpicosecond relaxation back from nonequilibrium by recombination of the quasiparticles defines the principal

frequency limit of devices based on the dynamical changes of Cooper-pair densities. The typical nonequilibrium kinetic inductance photoresponse of voltage transient [27,28] was ascribed to the nonequilibrium quasiparticle generation and recombination in the presence of an applied dc bias current by using a subpicosecond electro-optic sampling technique [29,30]. The modulation of kinetic inductance by ultrafast laser pulses has been utilized recently as a sampling technique for measuring ultrafast electric waveforms [31]. On the other hand, the reshaping of terahertz pulses upon transmission through superconducting thin films caused by the kinetic inductance of the superconducting charge carriers was detected by using the coherent THz-TDS [32-36]. In general, the kinetic inductance of charge carriers in normal state can be neglected since the intrinsic impedance is usually dominated by the resistance in this regime. In superconducting state, however, the kinetic inductance becomes more significant and must be considered as an important parameter.

In this dissertation, in addition to investigating the origin of photogenerated terahertz radiation from current-biased superconducting YBCO thin films, we will focus specially on exploring dynamics in the far-infrared with THz-TDS technique [37-51]. Based on the analysis of THz-TDS measurements, one can directly, extract the complex index of refraction from the measured complex transmission of the superconducting thin film. In addition, the pulse reshaping effect in the measured terahertz temporal profile caused by the kinetic inductance of the superconducting charge carriers can be identified with the aid of a transmission line analog. The THz-TDS transmission measurements enable us to extract directly the temperature- and frequency-dependent complex optical conductivity, temperature-dependent London penetration depth, and the quasiparticle scattering time.

In what follows, the dissertation is composed of six chapters. In chapter 2, we introduce the fabrication and characterization of samples (both SI-GaAs and YBCO

thin films) to generate terahertz radiation.

Chapter 3 presents the characteristics of the optically induced bipolar terahertz radiation generated from biased SI-GaAs photoconductive switches and detected by using a free-space electro-optic sampling technique. The dynamics of the emitted terahertz transient is discussed. In addition, the orientation dependence of the terahertz detection in ZnTe (110) sensor crystal was analyzed to optimize the operation parameters for terahertz pulse detection.
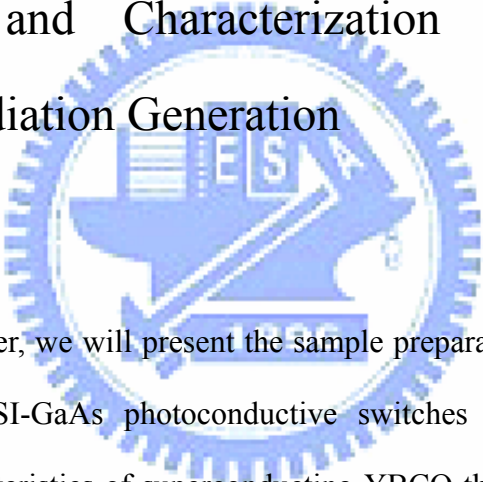
In chapter 4, we present the characteristics of photogenerated terahertz radiation in HTSC. The results delineate clearly the origin of photogenerated terahertz radiation pulse emitted from current-biased superconducting YBCO thin films excited by femtosecond laser pulses. By taking into account the effect of the pulse reshaping caused by the kinetic inductance of the superconducting charge carriers, we demonstrate the direct connection between the quasiparticle dynamics and the detected terahertz radiation based on the supercurrent modulation.

In chapter 5, we describe the development of the THz-TDS technique and the applications of the means to investigate the properties of the electrodynamics of superconductors at terahertz frequencies. The temperature- and frequency-dependent complex index of refraction of the samples, such as $NdGaO_3$ substrate and YBCO thin films, are extracted by analyzing the complex transmittance. Besides, we are able to obtain the complex optical conductivity of the YBCO thin films due to the provided frequency-dependent information by the method of the THz-TDS.

Finally, in chapter 6, we give a summary of the prominent results discussed in this dissertation.

Chapter 2

Preparation and Characterization of Samples for Terahertz Radiation Generation

In this chapter, we will present the sample preparation of two typical types of terahertz emitters SI-GaAs photoconductive switches and YBCO photoresistive devices. The characteristics of superconducting YBCO thin films deposited on MgO substrate were carefully studied. The films were then patterned into the antenna structure for further measurements. Meanwhile, pre-treatment of the MgO substrate prior to depositing YBCO thin film is necessary to improve the quality of films. The ultrafast photoresponse and quasiparticle relation dynamics of the YBCO films were measured by the femtosecond time-resolved spectroscopy.

2.1 Characterization of superconducting $YBa_2Cu_3O_{7-\delta}$ thin films deposited on MgO (100) substrate

MgO substrate is considered to be the ideal substrate for our purposes, since it remains transparent and non-dispersive at terahertz frequency measurements. Grischkowsky et al. reported that MgO is an excellent material in terms of its low loss and allows for the extended propagation of subpicosecond electromagnetic pulses at 85 K [52]. However, owing to the relatively large lattice mismatch between YBCO films and MgO substrate, quality of the epitaxial films depends substantially on the operating parameters including film's deposition conditions and pre-treatment of the polished substrate [53,54]. As mentioned by Hsu et al. in our group [55], thermal annealing of the substrate is found to be highly effective in producing epitaxial c-axis films with good superconducting properties. The temperature is optimized such that sufficient structure mobility enables formation of a surface consisting of a series of steps [56,57]. This is partly due to the fact that the initial stage of YBCO growth on MgO substrates is predominantly by an island growth mechanism. It is, hence, highly favorable for these islands to nucleate at the edge of steps formed on the surface of the MgO (100) substrate. In our case, the MgO substrate was annealed at the temperature 1100 ^{o}C in 760 Torr of pure oxygen for 24 hrs.

YBCO thin films were deposited on 0.5-mm-thick MgO (100) substrates by conventional on-axis pulsed laser deposition (PLD) using a KrF excimer laser source with $\lambda = 248$ nm operating at an energy density of 2.9 J/cm^2. The substrate temperature was held at 750 ^{o}C and oxygen pressure was kept at 0.3 Torr during deposition. After deposition was completed, oxygen gas was introduced into the PLD chamber to 1 atm, and was cooled down to room temperature. The films with a typical thickness of 110 nm were c axis oriented. The transport properties of typical

temperature dependent resistance curve of YBCO thin film measured by standard four-probe method is illustrated in Fig. 2-1. The film exhibits good metallic behavior with a critical temperature Tc of about 88 K after it annealing separately at the temperature 450 ^{o}C in 760 Torr of pure oxygen for 30 min.
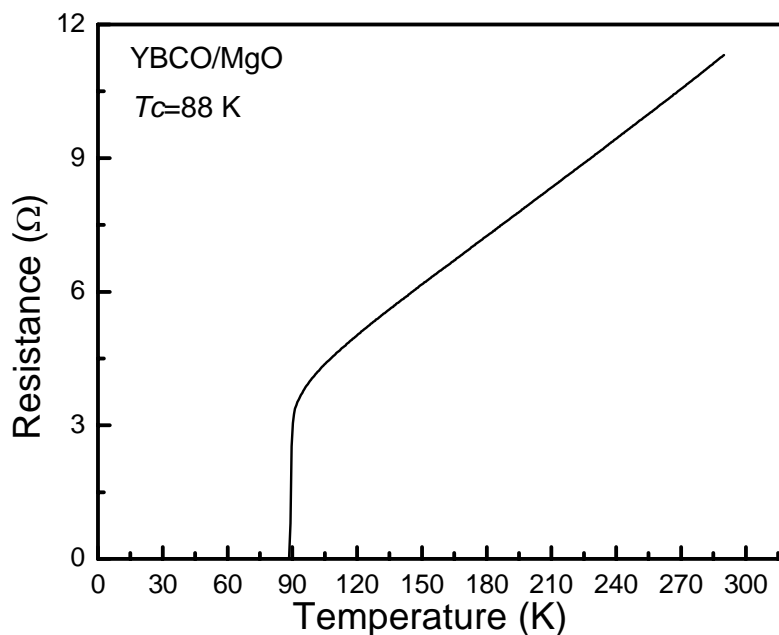
FIG. 2-1 *Resistance versus temperature curve for typical YBCO thin film grown on MgO (100) substrate. The substrate has been thermal annealing previously.*

The real-time measurements of the relaxation dynamics of YBCO superconducting films was investigated by using the femtosecond time-resolved spectroscopy. Usually, the optical reflectivity measured by the optical pump-probe method has the time scale ranging from few hundred femtosecond to picosecond range. While the gap opening is manifested by a rapid increase in the amplitude of the

FIG. 2-2 *Optical response of a YBCO thin film after excitation with fs laser pulses at 60 K. The inset shows reflectivity transient $\Delta R / R$ with time on a logarithmic scale. The solid line is drawn to indicate the trend. Here, the 300-nm-thick YBCO film was deposited on SrTiO$_3$ (100) substrate for optical measurements [58].*

photogenerated transient reflectance in the superconducting state as illustrated in Fig. 2-2, the relaxation apparently consists of two time scales. The ultrafast rise of the reflectivity after photoexcitation of the YBCO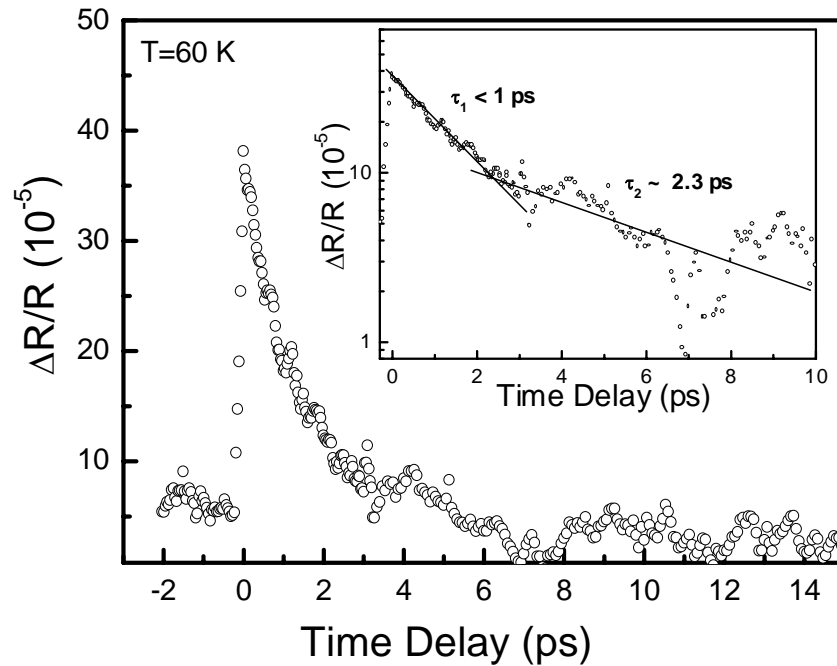 is attributed to quasiparticle generation (including the Cooper pairs breaking and photoexcitation of lower energy quasiparticles), and the subsequence decrease of the reflectivity results from quasiparticle relaxation mainly limited by recombination to Cooper pairs. The higher energy quasiparticles will relax to the lower energy quasiparticles via emitting phonons or quasiparticles; meanwhile, the lower energy quasiparticles could also recombine to form the Cooper pairs [14].Within this scenario, two distinct characteristic relaxation times in the superconducting state have been identified. Below *Tc*, as shown in the inset of Fig. 2-2, the logarithmic plots of $\Delta R / R$ reveal a break in slope near *t*=2.5 ps. Two relaxation processes [13,14] (fast component τ_1

and slow component τ_2) in our measured data can be clearly observed in YBCO films. In this case, the two-component fit to the data yields two relaxation times with $\tau_1 \sim 0.7$ ps and $\tau_2 \sim 2.3$ ps at 60 K. The slow relaxation component τ_2 of $\Delta R / R$ is considered to relate to the superconducting gap.

2.2 Fabrication of YBCO superconducting antenna as terahertz emitters

The as-deposited YBCO thin films were then patterned into a bow-tie antenna structure using standard photolithography and wet chemical etching. The critical temperature Tc (at R=0) remained 88 K after patterning into the antenna structure showing practically no shift in critical temperature comparing to the original film. Figure 2-3 displayed the configuration of the antenna that the center bridge is 200 μ m long and 100 μ m wide with the bow-tie angle of 60 °. Where, low resistivity electrical contacts to the film were made by evaporating approximately 200-nm-thick gold pads on the YBCO surface, which were subsequently annealed in 760 Torr of pure oxygen at 450 °C for 30 min [59].

Regarding to the electric properties of YBCO antenna, the *I-V* characteristic was shown in Fig. 2-4 which the critical current density *Jc* was about 1.7*10^6 A/cm^2 at 77 K. we note that the film grown on the polished substrate typically exhibit a *Jc*
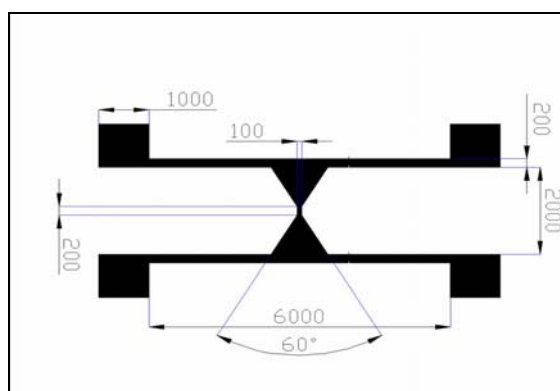
FIG. 2-3 *Configuration of bow-tie antenna structure of YBCO thin films (dark area) deposited on MgO substrate. The locations of god pads were displayed in square region. The optical pulses will incident normal to the center bridge of YBCO antenna.*

$(9.7*10^4 \text{ A/cm}^2)$ which is slightly smaller than that of films deposited on the annealed substrate $(2.3*10^5 \text{ A/cm}^2$ at 84 K), indicating the significant enhancement of transport properties by step-mediated growth.
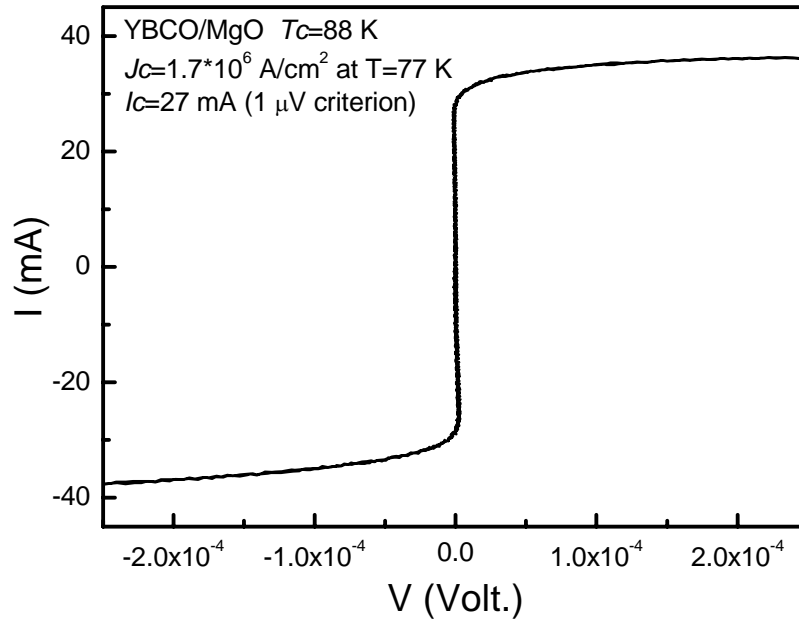
FIG. 2-4 *I-V characteristic taken at 77 K of antenna fabricated in a YBCO thin film.*

2.3 Fabrication of photoconductive switches as terahertz emitters

We also chose undoped semiconductor material (SI-GaAs wafer) to fabricate the emitters of terahertz radiation. The thickness of the high resistivity wafer ($\rho > 10\text{k}\,\Omega\text{-cm}$) is about 0.35 mm for the highly efficient terahertz propagation. The Au/Ge metal patterns of about 150-nm-thick used as electrodes are obtained by standard lift-off procedures. Figure 2-5 illustrated the layout of the fabricated photoconductive switches. A DC voltage bias was applied across the emitter, and the pump beam was normally incident. Characterization of the gap spacing of emitters was achieved by pattering the geometry. One can take the semiconductor material as the ideal photoconductive switch to generate terahertz radiation not only for understanding the fundamental properties of pulse shape of radiation but also employing in the study of the electrodynamics of superconductors analyzed by the terahertz time-domain transmission spectroscopy.

The characteristics of terahertz pulses generated from the YBCO photoresistive switches and SI-GaAs photoconductive switches will be presently and discussed in chapter 3 and 4, respectively.
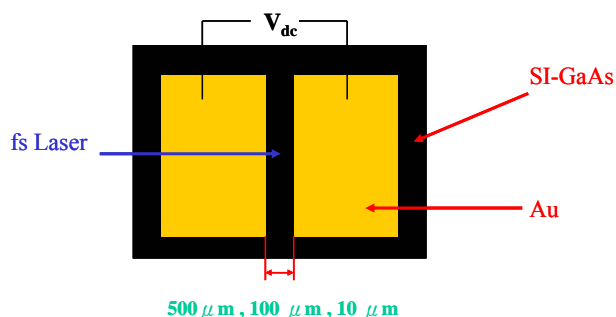
FIG. 2-5 *Schematic illustration of the top view of the SI-GaAs photoconductive switches.*

Chapter 3

Generation and Detection of Terahertz Pulses
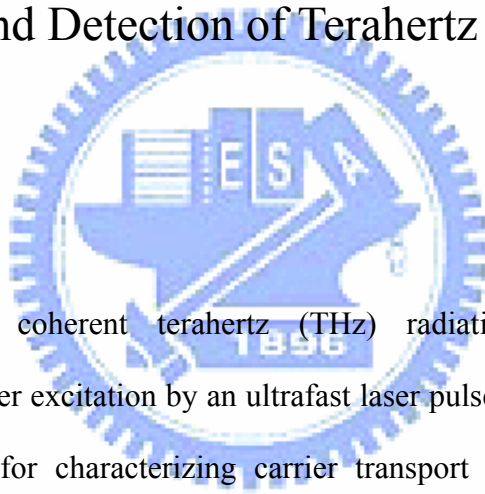
3.1 Introduction

Broad-band coherent terahertz (THz) radiation emitted from biased photoconductors after excitation by an ultrafast laser pulse [60-63] has been used as a spectroscopic tool for characterizing carrier transport in semiconductors [64,65], examining gap and subgap features of superconductors [66,67], and for the emerging applications of coherent terahertz imaging [68]. The emitted terahertz waveforms and frequency spectrum of the biased photoconductive switches have been studied by several groups [65,69]. Under some particular conditions, bipolar terahertz waveforms were obtained both in large- and small- aperture photoconductive switches. Usually, both large- and small-aperture photoconductive switches are defined to have an optically illuminated area of dimensions comparable to the center wavelength of the emitted radiation. The mechanism of the photoinduced terahertz radiation, however, is still a matter of debate. For instance, the reason why the emitted waveforms can exhibit unipolar and bipolar characteristics has provoked some exotic interpretations

[69]. In order to clarify some of the controversial issues, it is of interest to carry out systematic comparisons between the emissions generated with different operating parameters.

In this chapter, terahertz radiations obtained from biased photoconductive switches with various emitter gap spacings, applied bias fields and optical excitation fluences are reported. Our results showed that with the gap spacing ranging from 10 to 500 μm, the emitted radiations are all bipolar in nature. Furthermore, the waveform and the frequency spectrum distribution do not depend on the optical excitation fluence or strength of the biased field. This suggests that the terahertz radiation obtained in the current setup originates from essentially the same mechanism as that associated with the ultrafast charge transport process during pulsed laser illumination.

Depending on the radiation and detection schemes employed, the resultant waveforms and frequency bandwidths were different and had been a subject of extensive research. For instance, Cai *et al.* [70] and Park *et al.* [71] have made a direct comparison between the performances and detected waveforms of free-space electro-optic sampling and photoconductive antenna detection schemes to detect coherent terahertz radiation emitted from biased low-temperature-grown GaAs emitters.

In terahertz detection measurements, we use a free-space electro-optic sampling (FSEOS) system to observe the transient terahertz radiation from the semi-insulating GaAs (SI-GaAs) photoconductive switches. The polarization change of the probe beam occurs when the ZnTe sensor crystal, based on the Pockels effect, is irradiated by the terahertz electric field. The terahertz-induced phase retardation of the probe beam is converted into an intensity modulation and detected by using balanced photodiodes. Picosecond electromagnetic pulses will be obtained. Besides, the orientation dependence of the terahertz detection in ZnTe was analyzed to optimize

the operation parameters for terahertz pulse detection.

The FSEOS system can also be used to measure the characteristics of terahertz radiation generated from the photoconductive materials and to study the nonequilibrium processes in high-Tc superconductors. Furthermore, based on the set up of technique of terahertz generation and detection, we can establish coherent terahertz time-domain spectroscopy technique, which uses SI-GaAs photoconductive switch as the terahertz radiation source, to measure the high frequency response such as the temperature- and frequency-dependent of the index of refraction, optical conductivity, and penetration depth in HTSC films. These results will be presented in chapter 4 and 5.

3.2 Optical setup

The experimental setup of the free-space electro-optic sampling system [68,72] is illustrated schematically in Fig. 3-1. A CW argon-laser-pumped, compact mode-locked Ti:sapphire laser (femtosource C20) provides 20 fs optical pulses at 800 nm (1.55 eV) with a 75 MHz repetition rate. The pump beam aligned at normal incidence is modulated by a mechanical chopper operated at 1.3 kHz. The electric field of a terahertz pulse is sampled by scanning the delay between the pump and probe beam. An undoped SI-GaAs photoconductive emitter, triggered by femtosecond laser pulses, radiates the THz beams. The emitted radiation is collimated and focused by a pair of off-axis paraboloidal mirrors onto the ZnTe sensor crystal. The Au/Ge metal patterns of the planar emitters are obtained by standard lift-off procedures. A

16

5-μm-thick pellicle beam splitter, which is transparent to the terahertz beam, is used to reflect 50% of the synchronized optical probe beam collinearly along the terahertz beam. The polarized terahertz and probe beams are aligned to a 1-mm-thick <110>-oriented ZnTe sensor crystal. We used a quarter-wave plate to impart a $\pi/2$ optical bias to the probe beam, which allows the system to be operated in the linear range. A Wollaston polarizer is used to convert the terahertz-field-induced phase retardation of the probe beam into an intensity modulation between the two mutually orthogonal linearly polarized beams. The optical intensity modulation is detected using balanced photodiodes in a digital lock-in amplifier (SR830).
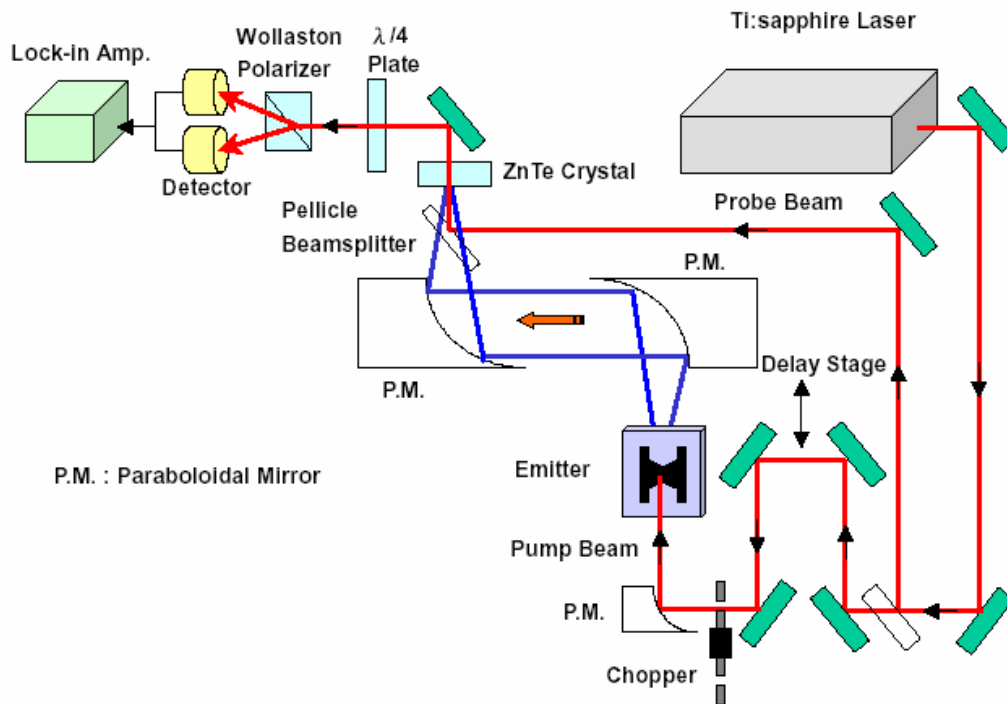

FIG. 3-1. *Schematics of the experimental setup of free-space electro-optic sampling system.*

3.3 Bipolar photogenerated terahertz radiation in biased SI-GaAs photoconductive switches

3.3.1 Origin of the transient terahertz generation

In general, when a femtosecond laser pulse illuminates the semiconductors with a photon energy greater than the band gap (for SI-GaAs, band-gap E_g=1.42 eV), photons are absorbed, thus creating electrons and holes. The external biased field drives the photogenerated carriers to form a transient photocurrent across the field region. Namely, a radiated terahertz electric field is obtained by the time derivative of the net current. It acts as the source term in Maxwell's equations.

$$E_{THz} \propto \frac{\partial J}{\partial t} ,$$ Eq. (3-1)

By biasing a constant voltage across the gap spacing of the emitter, carriers photoinjected into the gap by ultrafast laser pulse will be accelerated, leading to the emission of a transient and broad-band frequency terahertz radiation [Fig. 3-2].
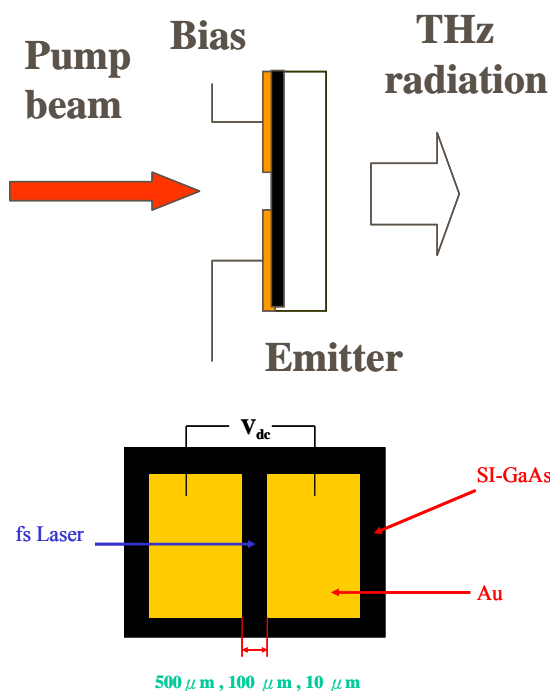

FIG. 3-2. *Schematics of terahertz generation as a femtosecond laser pulses illuminates the biased photoconductive switches. The gap spacing of emitters is illustrated in the lower panel.*

3.3.2 Optical fluence and biased voltage dependence

Figure 3-3 shows the typical photogenerated terahertz signals as a function of the scanning delay time obtained from the SI-GaAs photoconductive switches with a biased field of 2 kV/cm. The average pumping powers (fluences) are (a) 130 mW (0.8 μJ/cm^2) and (b) 1 mW (60 nJ/cm^2). The gap spacing of this emitter is 500 μm. Nearly symmetrical terahertz waveforms are observed. The signal-to-noise ratio (SNR) is about 10^3 (10^6 in power) for the 130 mW case. In contrast, for the 1 mW case, strong noise is observed before delay time t=0. There are some secondary peaks not shown here that appeared after about 15 ps delay of the main terahertz signals, which are believed to arise from substrate multiple reflections.
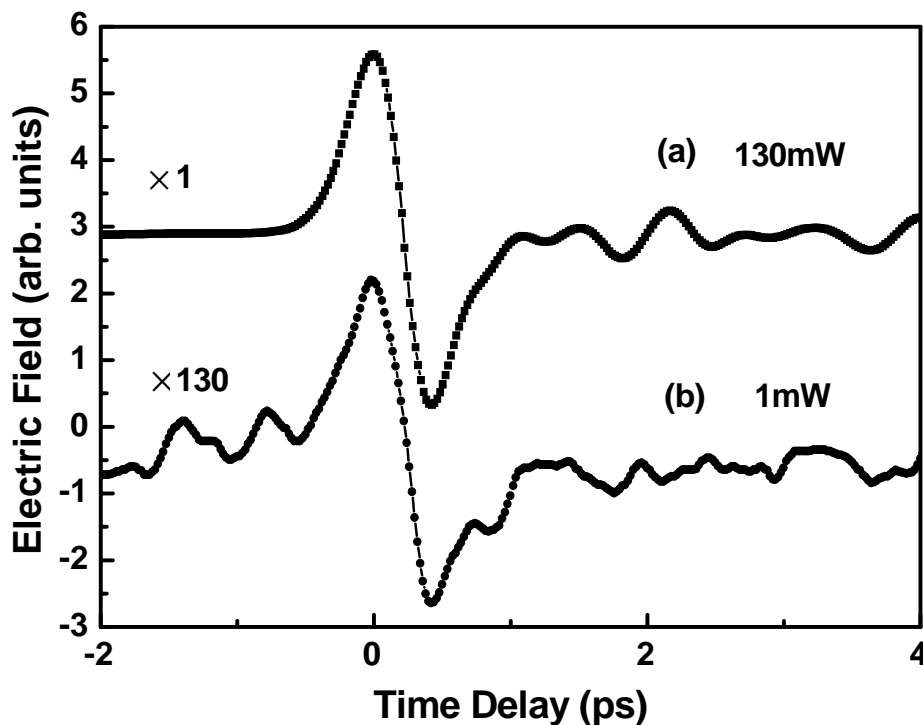
FIG. 3-3. *Transient terahertz waveforms for 500 μm gap spacing photoconductive switches. The average pumping power is (a) 130 mW and (b) 1 mW.*

In Fig. 3-3, an integrated terahertz pulse is sampled about 2 ps. The time integral of the measured terahertz electric field of SI-GaAs photoconductive switches shown in Fig. 3-4 will be separated into two parts: the rise time and the fall time components. The rise time (the full width of half-maximum (FWHM) is 310 fs) and fall time of the photocurrent are 0.9 ps and 1.2 ps, respectively. The induced photocurrent produced and vanished with a time of about 2.1 ps. The carrier transient time across the biased field width is obviously much shorter than the carrier lifetime (~100-300 ps). This cannot be explained by attributing the effects to carrier lifetime as was proposed by Budiarto *et al* [73].
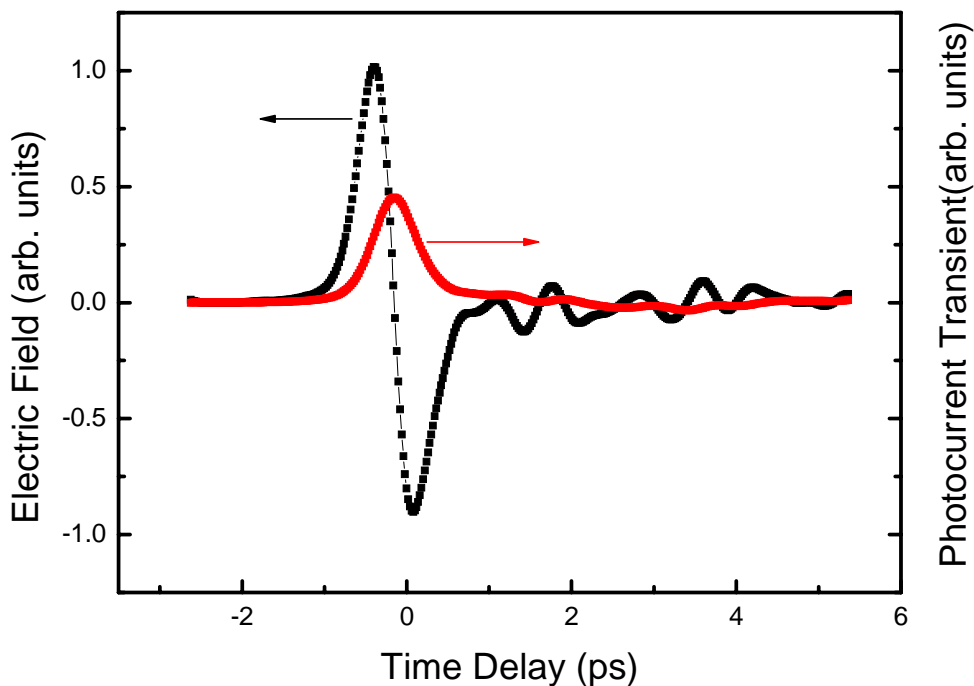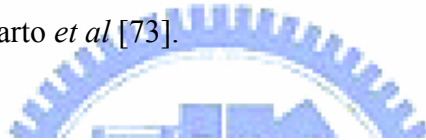
FIG. 3-4. *Time integral of the measured terahertz electric field of SI-GaAs photoconductive switches. The induced photocurrent produced and vanished with a time of about 2.1 ps.*

Figure 3-5 shows the representative power spectrum derived by Fourier transform of the terahertz waveforms. The radiation frequency spectrum extends from 0.1 THz to 3 THz. The central frequency is 0.7 THz and the region of maximum intensity distribution of the spectral pattern lies in the range of 0.4~0.9 THz. The bandwidth of half-maximum (BWHM) of the frequency spectrum is around 1.1 THz. Fig. 3-6 shows plots of a series of emitted bipolar terahertz radiations as a function of average pumping power for the 0.5-mm-wide photoconductive switch. It is evident that the symmetrical terahertz waveforms remain intact over the whole range of optical excitation fluences studied. Moreover, the peak strength of the emitted terahertz field increases linearly with optical excitation fluence. The absence of amplitude saturation, as observed by Darrow *et al.*, [60] may be due to the smaller excitation fluences used here.

FIG. 3-5. *Corresponding frequency spectrum by Fourier transform of the terahertz waveforms.*

FIG. 3-6. *The figure shows a series of emitted terahertz waveforms obtained at various average pumping powers for 500 μm gap spacing photoconductive switches.*
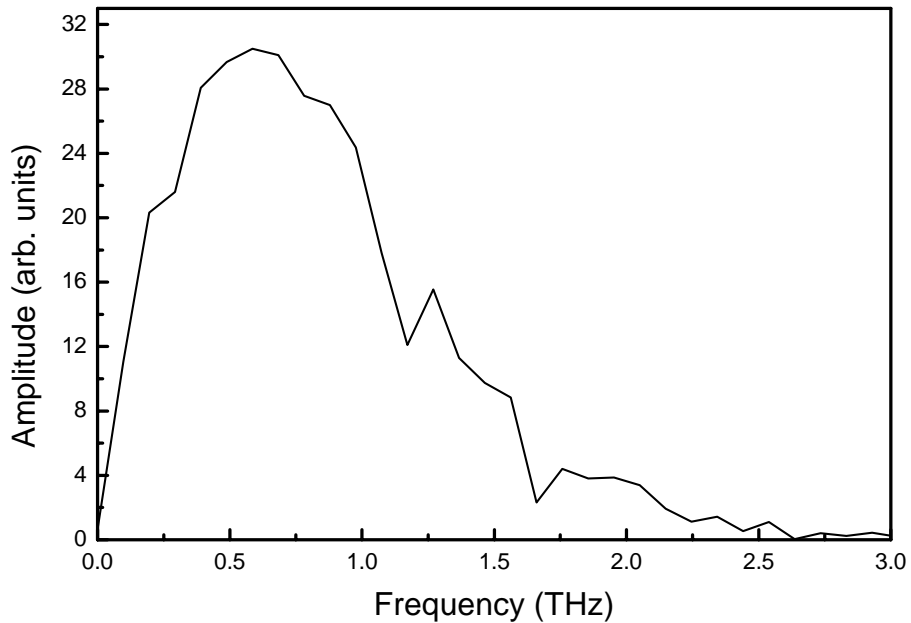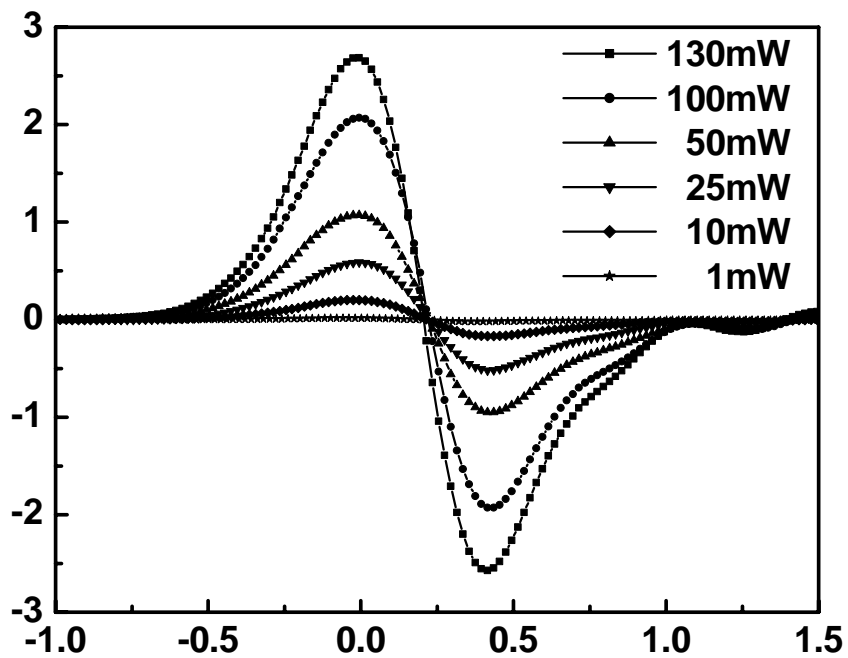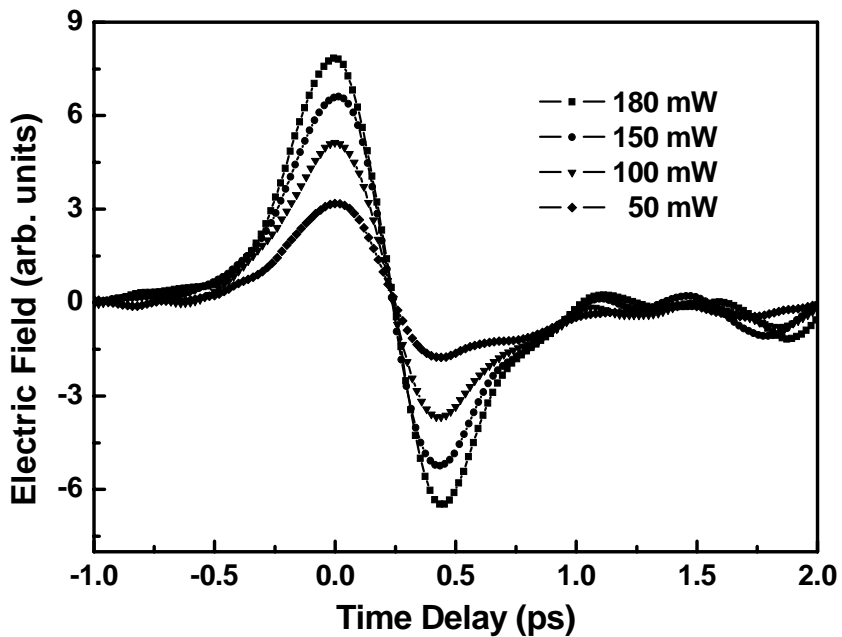

FIG. 3-7. *A series of emitted transient terahertz waveforms for 10-μm-wide photoconductive switch.*

3.3.3 Emitter gap spacing dependence

From the above results, it is evident that, in large-aperture photoconductive switches, the bipolar nature of the terahertz radiation waveforms is independent of pumping power. It is thus interesting to see whether the waveforms and frequency spectra would change with the emitter gap spacing. Fig. 3-7 shows a series of emitted bipolar terahertz radiations as a function of average pumping power for the 10-μm-wide photoconductive switch. As can be seen, the slightly unsymmetrical terahertz waveforms remain intact over the whole range of optical excitation fluences studied. Nearly the same ratio of the terahertz pulse for the positive lobe to that for the negative lobe is obtained under different optical excitation fluences for a 10 μm emitter gap spacing. For 100 μm gap spacing photoconductive switches (not shown here), similar behaviors are also observed. Since the size of the laser spot is about 500 μm and 30 μm for 500 μm and 10 μm gap spacing switches, respectively, the current results display no signature of unipolar to bipolar waveforms transitions [65].

Since the waveforms are essentially the same for all cases, it is suggested that the broad-band frequency spectrum of the emitted radiation is not dependent on either the excitation fluences or the emitter gap spacing. In addition, experiments have shown that the waveforms and frequency spectrum of the emitted radiation display no dependence on the strength of the biased field. In our measurement configuration, the optical pumping (800 nm) is incident normal to the emitter substrate so that the radiation output is independent of surface depletion and different frequency mixing due to the surface $\chi^{(2)}$ of photoconductors. [74] The robust characteristics of the emitted radiation indicate that the same underlying physical mechanism prevails in all cases.

In fact, similar results have been reported by Lu *et al*. [68] for a 2.5-mm-wide emitter using the free-space electro-optic sampling technique. These, however, are in sharp contrast with some of the results reported in literature. It has been proposed that bipolar waveforms of terahertz radiation, which can only appear in large-aperture photoconductors with high optical excitation fluences, are a consequence of space-charge screening of the bias field. [69] On the other hand, Pederson *et al*. [65] studied the effects of carrier density on the emitted waveform for a 50-μm-wide emitter and concluded that the emitted radiation changes from unipolar to bipolar with increasing photoexcited carrier density. In our case, a bipolar nature of terahertz radiation is obtained, and the fall time of the transient photocurrent seems to be independent of the different operating parameters. In other words, the carrier transient time across the biased field width, in either the 500-μm- or 10-μm-wide photoconductive switches, is very fast and much shorter than the carrier lifetime. Since the bipolar nature of the terahertz radiation obtained in the current setup persists in virtually every case studied, the current results can be interpreted consistently in terms of the mechanism associated with the ultrafast charge transport process during pulse laser illumination. The apparent discrepancies mentioned above may arise merely from detection and sampling techniques. It is noted that the alignment for the generation and detection of terahertz radiation must be handled very carefully for the 10 μm gap spacing emitter in the experimental process. The laser spot of focused optical normal incidence may partly pass through the substrate and be detected by the system at higher fluences. Such a situation may have blurred the actual signals from the photogenerated radiation.

In conclusion, the characteristics of optically induced bipolar terahertz radiation in biased photoconductive switches were investigated systematically by a free-space electro-optic sampling technique. It was observed that the bipolar nature

and the emitted frequency spectrum distribution remained unchanged on varying the optical excitation fluence, strength of the biased field and the emitter gap spacing. These results are in agreement with the dynamics of the optically induced ultrafast charge transport driven by the biased field.

3.4 Detection of terahertz pulses of FSEOS system

Developed originally for the characterization of ultrashort electrical transients, the electro-optic sampling (EOS) reported by Zhang *et al*., [see Fig. 3-8] as developed into a powerful method of the detection of terahertz pulses [72]. The EOS is based on the electric field of a terahertz pulse inducing an instantaneous birefringence in an electro-optic crystal through a non-linearity of the first order (Pockels effect). Passing through such crystal, the initially linearity polarized optical probe beam gains small elliptical polarization. The starting point of the calculation of the terahertz detection is the refractive-index ellipsoid that arises when an electric field is applied to the crystal. Since the terahertz pulse is much longer than the laser pulse (several ps versus tens of fs), the terahertz pulse can be approximately treated as a dc bias field. Thus, by varying the delay between terahertz- and optical probe pulses the whole time profile of the pulse can be traced.
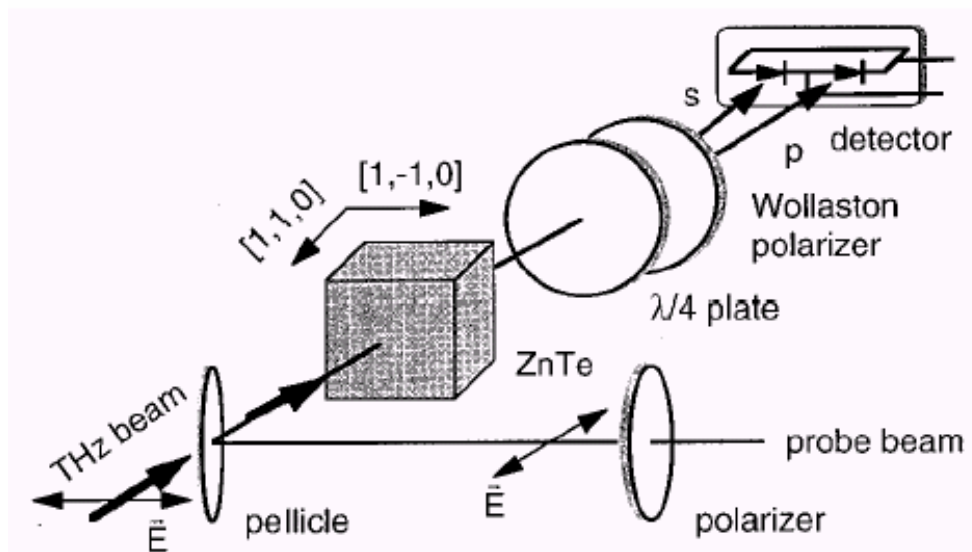

FIG. 3-8. *Free-space electro-optic sampling*

3.4.1 Calculation of the refractive-index ellipsoid of the terahertz detection [75,76]

The orientation of the 1-mm-thick <110>-oriented ZnTe crystal with respect to the propagation direction and polarization of the terahertz and optical probe beam is shown in Fig. 3-9. k_{THz} and k_p give the propagation directions of the terahertz and the probe beam, respectively. We define α as the angle of the terahertz beam polarization with respect to the (001) axis (z axis) and φ as the angle of the probe beam polarization with respect to the crystal (001) axis. The index ellipsoid defines the refractive index in the crystal that is experienced by visible-near-IR light propagating through the crystal with a given propagation direction and polarization. With no electric field applied, the material (ZnTe) is isotropic so that the refractive-index ellipsoid is simply a sphere i.e. $n_{i,j} = n$ for every i and j. The coordinate system x', y', and z' is linked to the propagating beams: the beams travel along the $x' = <-1,-1,0>$ direction, the optical probe and the terahertz beams are polarized with an angle respect to the crystal (001) axis. Under the influence of the applied terahertz field, the sphere [Fig. 3-10(b)] turns to an ellipsoid [Fig. 3-10(c)] with the main oriented along x'', y'', and z'' directions [Fig. 3-10(a)].
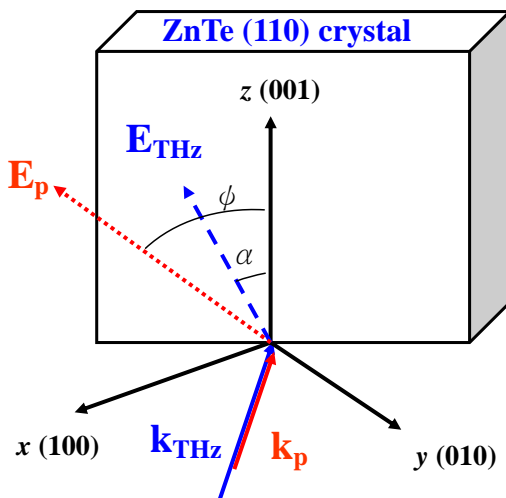

FIG. 3-9. *Relative orientation of the terahertz electric field and the polarization of the laser probe- and the terahertz beams with respective to the ZnTe crystal. k_{THz} and k_p give the propagation directions of the terahertz and the probe beam, respectively. x corresponds to the (100) axis, y to the (010) axis, and z to the (001) axis.*
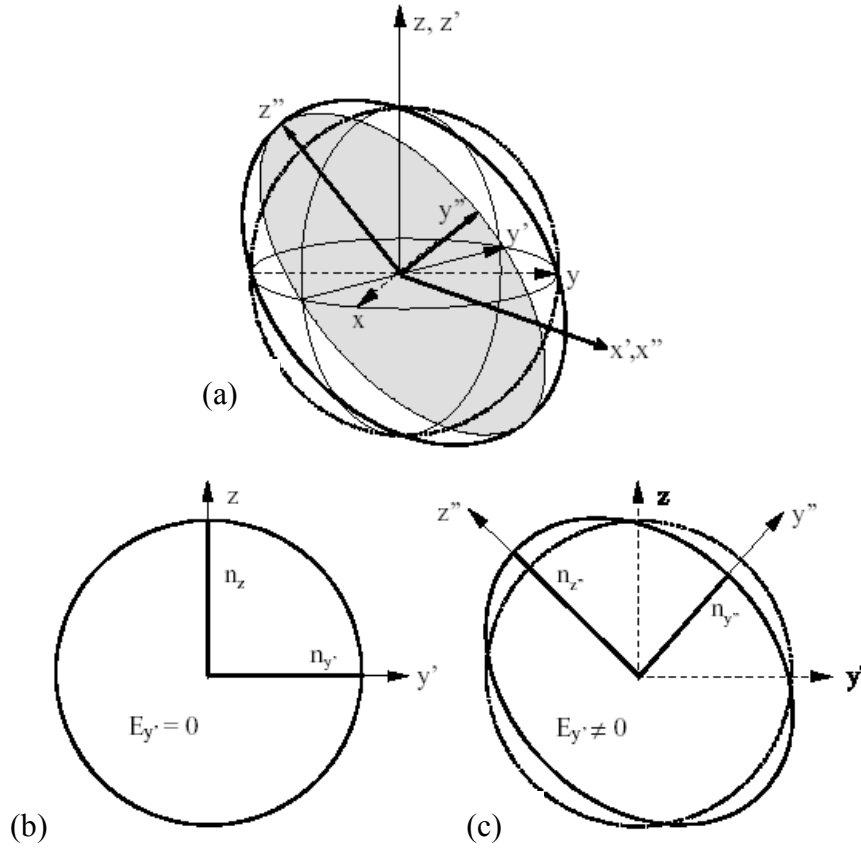
FIG. 3-10. *(a) The refractive-index ellipsoid. The x, y, z coordinates are set along the main ZnTe crystallographic direction; the primed axes are defined as the terahertz- and the optical probe beams propagation(x'), the terahertz- and the probe beams(z'=z) polarization directions. The double-primed axes correspond to the orientation of the main axes of the refractive-index ellipsoid under the terahertz field applied. (b) and (c) depict the projection of the ellipsoid on the surface of the crystal (i.e. as it is seen by the incident laser probe beam): without the terahertz field (b) and with terahertz field present (c).*

Its optical properties can be described with the refractive-index ellipsoid

$$\frac{x^2}{n^2} + \frac{y^2}{n^2} + \frac{z^2}{n^2} = 1,$$ Eq. (3-2)

where *x, y,* and *z* define the coordinate axes in the crystal, with the *z* axis corresponding to the (001) crystal axis. Now, if a terahertz field is applied to the crystal, the electric field would modify the refractive index of the crystal. This is so

called electro-optic effect and the Eq. (3-2) of index ellipsoid can be modified to Eq.

(3-3) where γ_{41} ($\gamma_{41} = 3.9 \times 10^{-12} \, m/V$) is the electro-optic coefficient [77].

$$\frac{x^2}{n^2} + \frac{y^2}{n^2} + \frac{z^2}{n^2} + 2E_{THz,x}\gamma_{41}yz + 2E_{THz,y}\gamma_{41}xz + 2E_{THz,z}\gamma_{41}xy = 1, \qquad \text{Eq. (3-3)}$$

where $E_{THz,x}$, $E_{THz,y}$, and $E_{THz,z}$ are the components of the applied terahertz field E_{THz}

along the x, y, and z directions, respectively, and where n is the unperturbed refractive

index. The presence of the mixed terms yz, xz, and xy in Eq. (3-3) indicates that the

axes of the ellipsoid do not coincide with the coordinate axes. The main problem is to

find a coordinate transformation such that the main axes of the ellipsoid are aligned

with the new coordinate axes. Then, by projecting the probe-laser polarization on

these axes, we can calculate the effect that the field-induced refractive-index change

has on the pulse polarization as it propagates through the crystal. We can make an

immediate simplification by noting that, for a terahertz pulse propagating along the

(110) axis, $E_{THz,y} = -E_{THz,x}$. After studying Eq. (3-3), we find that we need two

coordinate transformations to align the index ellipsoid with the new coordinate axes.

The first transformation is a rotation of 45° around the z axis,

$$x = x^{'}\cos 45^o - y^{'}\sin 45^o = \frac{1}{\sqrt{2}}x^{'} - \frac{1}{\sqrt{2}}y^{'},$$

$$y = x^{'}\sin 45^o + y^{'}\cos 45^o = \frac{1}{\sqrt{2}}x^{'} + \frac{1}{\sqrt{2}}y^{'}, \qquad \text{Eq. (3-4)}$$

$$z = z^{'},$$

Equations (3-4) transform the ellipsoid into the form

$$x^{'2}(\frac{1}{n^2} + E_{THz,z}\gamma_{41}) + y^{'2}(\frac{1}{n^2} - E_{THz,z}\gamma_{41}) + \frac{z^{'2}}{n^2} + 2\sqrt{2}E_{THz,x}\gamma_{41}y^{'}z^{'} = 1, \text{Eq. (3-5)}$$

From the remaining mixed $y^{'}z^{'}$ term in Eq. (3-5) we deduce that a final

rotation of the $(x^{'}, y^{'}, z^{'})$ system with the $x^{'}$ axis is needed to align the coordinate

system with the main axes of the index ellipsoid. Taking the angle over which the

coordinate system is rotated to be θ, we can write for the transformation

$$x' = x'' \, ,$$

$$y' = y'' \cos\theta - z'' \sin\theta \, ,$$ Eq. (3-6)

$$z' = y'' \sin\theta + z'' \cos\theta \, ,$$

We express the components of the electric field in terms of the angle α:

$$E_{THz,z} = E_{THz} \cos\alpha \, ,$$

$$E_{THz,x} = \frac{1}{\sqrt{2}} E_{THz} \sin\alpha \, ,$$ Eq. (3-7)

with $E_{THz} = |\boldsymbol{E}_{THz}|$. With these definitions and after some algebra, we find for the index ellipsoid

$$x''^2 \left(\frac{1}{n^2} + E_{THz}\gamma_{41} \cos\alpha \right) + y''^2 \left\{ \frac{1}{n^2} - E_{THz}\gamma_{41} \left[\cos\alpha \sin^2\theta + \cos(\alpha + 2\theta) \right] \right\}$$

$$+ z''^2 \left\{ \frac{1}{n^2} - E_{THz}\gamma_{41} \left[\cos\alpha \cos^2\theta - \cos(\alpha + 2\theta) \right] \right\} = 1$$

Eq. (3-8)

in which $\cos\alpha \sin\theta \cos\theta + \sin\alpha(\cos^2\theta - \sin^2\theta) = 0$

provided that

$$\tan 2\theta = -2\tan\alpha$$ Eq. (3-9)

$$2\theta = -\arctan(2\tan\alpha) - n\pi$$

$$\left(n - \frac{1}{2} \right)\pi \le \alpha < \left(n + \frac{1}{2} \right)\pi \, , \qquad n=0,1,\dots$$

The angle θ over which we rotate the coordinate system around the axis x' is thus a function of the angle α between the terahertz polarization and the (001) axis. This ellipsoid can be alternatively be written as

$$\frac{x''^2}{n_{x''}^2} + \frac{y''^2}{n_{y''}^2} + \frac{z''^2}{n_{z''}^2} = 1 \, ,$$ Eq. (3-10)

For small electric fields, $\gamma_{41} E_{THz} \ll 1/n^2$, we obtain from Eq. (3-8) the refractive indices for visible-near-IR light propagating along the x'' direction

$$n_{y''}(\alpha) \approx n + \frac{n^3}{2} E_{THz} \gamma_{41} \left[\cos\alpha \sin^2\theta + \cos(\alpha + 2\theta) \right],$$

$$n_{z''}(\alpha) \approx n + \frac{n^3}{2} E_{THz} \gamma_{41} \left[\cos\alpha \cos^2\theta - \cos(\alpha + 2\theta) \right], \qquad \text{Eq. (3-11)}$$

where θ is given by Eq. (3-9).

Figure 3-10 shows the curve formed by the interaction of the plane perpendicular to the direction of propagation (i.e. as it is "seen" by the incident laser probe beam) with the index ellipsoid. For the case in which no terahertz field is applied, the curve has the form of circle [Fig. 3-10(b)], showing that the refractive index has the value n for any direction of polarization. For the case in which a terahertz field is applied, this curve has the form of an ellipse [Fig. 3-10(c)]. Consequently the semiminor and semimajor axes of this ellipse are along the y'' and z'' direction and have lengths $n_{y''}$ and $n_{z''}$ respectively.

A wave polarized in the y'' direction propagates with a different phase velocity than a wave polarized in the z'' direction. In propagating through the length of the modulator crystal, the y'' and z'' polarization components will thus acquire the phase shift Γ:

$$\Gamma = \frac{\omega}{c}(\Delta n)L = \frac{\omega}{c}\left[n_{y''}(\alpha) - n_{z''}(\alpha) \right]L, \qquad \text{Eq. (3-12)}$$

where L is the crystal length. We get

$$\Gamma = \frac{\omega n^3 E_{THz} \gamma_{41} L}{2c}\left[\cos\alpha \cos 2\theta - 2\sin\alpha \sin 2\theta \right], \qquad \text{Eq. (3-13)}$$

which is known as the retardation. In the absence of the terahertz field (E_{THz}=0), the phase shift is zero and the polarization of the probe beam stays linear. When, however, the terahertz pulse is present the phase shift Γ leads to a slightly elliptical polarization.

From Eqs. (3-11) and (3-13) it is clear that $n_{y''}$ and $n_{z''}$ are different and therefore that the electric field polarization components of the probe-laser field, E_p, in

31

the y'' and z'' direction, the probe field becomes elliptically polarized. The intensity difference, ΔI, of the polarization components that correspond to the ellipse can be calculated [75]:

$$\Delta I(\alpha,\varphi) = I_p \sin[2(\varphi - \theta)]\sin\left\{\frac{\omega}{c}\left[n_{y''}(\alpha) - n_{z''}(\alpha)\right]L\right\},\qquad\text{Eq. (3-14)}$$

where L is the crystal length, I_p, is the probe intensity, c is the velocity of light in vacuum, and ω is the angular frequency of the probe pulse. When the field-induced phase difference is small, we can replace the second sine in Eq. (3-14) with its arguments. Using Eq. (3-9) and relation (3-11), we can then simplify the equation to

$$\Delta I(\alpha,\varphi) = I_p \frac{\omega n^3 E_{THz}\gamma_{41}L}{2c}(\cos\alpha\sin 2\varphi + 2\sin\alpha\cos 2\varphi),\qquad\text{Eq. (3-15)}$$

Equation (3-15) shows that the signal from the balanced detectors is proportional to the applied electric field. Thus, by the variation of the delay between terahertz- and optical probe pulses the whole time profile of the terahertz pulse can be traced.
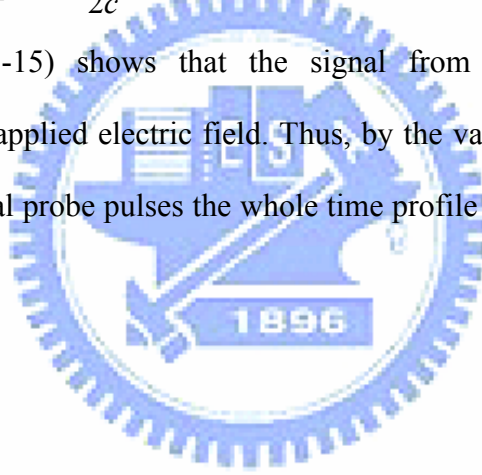
3.4.2 Orientation dependence of terahertz detection in ZnTe

Equation (3-15) indicated the measured dependence on the crystal's azimuthal angle α of the detected terahertz electric field between the probe beam polarization and the terahertz polarization. Interestingly, a comparison of the maximum signals between the terahertz polarization and the probe beam polarization shows that the maximum signal is obtained for $\varphi = \alpha + 90^o$ or $\varphi = \alpha$ [75]. Thus, in our case, $\varphi = \alpha$, we get

$$\Delta I(\alpha) = I_p \frac{\omega n^3 E_{THz}\gamma_{41}L}{2c}(\cos\alpha\sin 2\alpha + 2\sin\alpha\cos 2\alpha),\qquad\text{Eq. (3-16)}$$
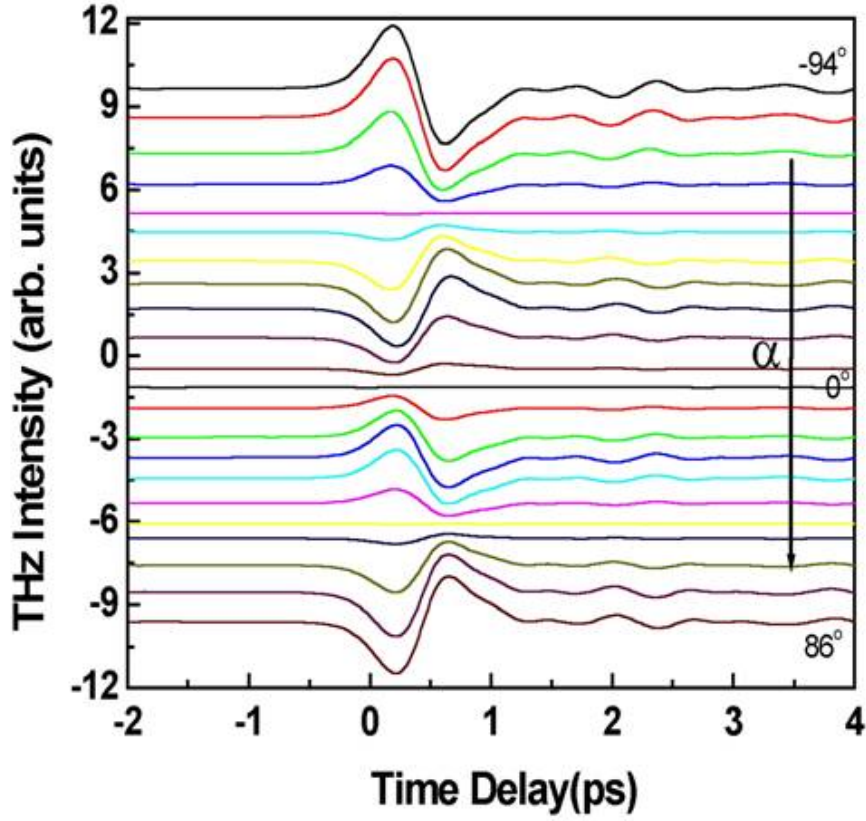
FIG. 3-11. *The measured pulse shapes of the terahertz pulses with respect to the crystal's azimuthal angle* α.

The measured results of the terahertz pulses with respect to the crystal's azimuthal angle α is illustrated in Fig. 3-11. The terahertz pulse shape keep unchanged, but the intensity of the signal and the polarity will vary with the angle α. Figure 3-12 shows the measured maxima of the terahertz amplitude as a function of the azimuthal angle α when the probe beam polarization is parallel to the terahertz beam polarization. As $\alpha = \varphi = 90^{o}$, in our case, we can get the maxima signal

$$\Delta I(\alpha,\varphi) = I_p \frac{\omega n^3 E_{THz} \gamma_{41} L}{c} \quad , \qquad\qquad \text{Eq. (3-17)}$$

The orientation dependence of terahertz beam detection in ZnTe was accomplished by using an undoped SI-GaAs photoconductive switch [78]. The

33

calculation is based on Eq. (3-16) and is in excellent agreement with the measurements, showing the correct maxima and minima in the terahertz detection efficiency as a function of the azimuthal angle [see Fig. 3-12]. These results show the optimal operating parameters for terahertz pulse detection using the ZnTe crystal.
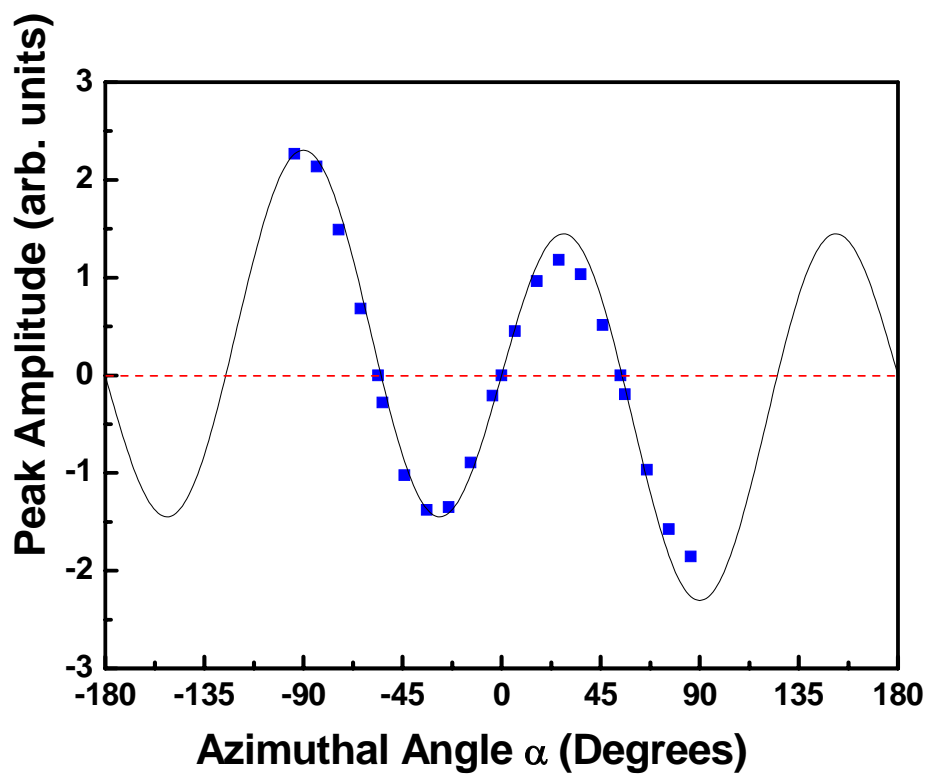

FIG. 3-12. *The measured maxima of the terahertz amplitude as a function of the (110)-oriented ZnTe crystal's azimuthal angle α when the probe beam polarization is parallel to the terahertz beam polarization, where the terahertz measurements (square) and fit curve [Eq. (3-16)] (solid line).*

3.4.3 Transmission characteristics of terahertz detection in the optimum orientation of

ZnTe crystal

Here, we will focus on the calculation of the refractive-index ellipsoid of the terahertz radiation as operating in the optimal parameters. From the results of the Fig. 3-12, one can measure maxima intensity of the terahertz signal as the angles satisfied $\alpha = \varphi = 90^o$. The polarization of both the terahertz and optical probe beams are aligned parallel to the [1,-1,0] direction of (110) oriented ZnTe sensor crystal. The ellipsoid of the Eq. (3-5) will then rewritten as

$$\frac{x'^2}{n^2} + \frac{y'^2}{n^2} + \frac{z'^2}{n^2} + 2E_{THz}\gamma_{41}y'z' = 1 \qquad \text{Eq. (3-18)}$$

where, $E_{THz,z} = E_{THz}\cos 90^o = 0$ and $E_x = -E_y = (1/\sqrt{2})E_{THz}\sin 90^o = (1/\sqrt{2})E_{THz}$.

In addition, from the Eq. (3-9), the angle θ of the second coordinate transformation is obtained of value 45°. From the remaining mixed $y'z'$ term in Eq. (3-18) we deduce that a final rotation of the (x',y',z') system with the x' axis is needed to align the coordinate system with the main axes of the index ellipsoid. Taking the angle over which the coordinate system is rotated to be $\theta = 45^o$, we can write for the transformation

$$x' = x'' ,$$

$$y' = y''\cos 45^o - z''\sin 45^o = \frac{1}{\sqrt{2}}y'' - \frac{1}{\sqrt{2}}z'' , \qquad \text{Eq. (3-19)}$$

$$z' = y''\sin 45^o + z''\cos 45^o = \frac{1}{\sqrt{2}}y'' + \frac{1}{\sqrt{2}}z'' ,$$

Equation (3-19) transform the ellipsoid into the form

$$\frac{x''^2}{n^2} + y''^2(\frac{1}{n^2} + E_{THz}\gamma_{41}) + z''^2(\frac{1}{n^2} - E_{THz}\gamma_{41}) = 1 , \qquad \text{Eq. (3-20)}$$

Equation (3-20) shows that x'', y'', and z'' are indeed the principal axes of the

ellipsoid when the terahertz and optical probe beams are aligned parallel to the [1,-1,0], y' axis, direction of (110) oriented ZnTe sensor crystal. According to Eq. (3-20), the length of the y'' axis of the ellipsoid is $2n_{y''}$, where

$$\frac{1}{n_{y''}^2} = \frac{1}{n^2} + E_{THz}\gamma_{41},$$

Eq. (3-21)

Assume $\gamma_{41}E_{THz} << 1/n^2$ and using the differential relation

$$dn = -(n^3/2)d(1/n^2),$$

gives

$$n_{y''} = n + \frac{n^3}{2}E_{THz}\gamma_{41},$$

Eq. (3-22)

and, similarly,

$$n_{z''} = n - \frac{n^3}{2}E_{THz}\gamma_{41},$$

Eq. (3-23)

A wave polarized in the y'' direction propagates with a different phase velocity than a wave polarized in the z'' direction. In propagating through the length of the modulator crystal, the y'' and z'' polarization components will thus acquire the phase shift Γ:

$$\Gamma = \frac{\omega}{c}(\Delta n)L = \frac{\omega}{c}\left[n_{y''} - n_{z''}\right]L,$$

Eq. (3-24)

we have form

$$\Gamma = \frac{\omega n^3 E_{THz}\gamma_{41}L}{c},$$

Eq. (3-25)

which is known as the retardation.

Considering the principle of the free-space electro-optic sampling, as shown in Fig. 3-13, it consists of an electro-optic crystal, a quarter-wave plate, and a Wollaston polarizer. The quarter-wave plate is oriented with its slow axis and fast axis parallel to y'' and z'' axes, respectively. Then an extra phase difference $\pi/2$ will be introduced and the total retardation is the sum of the retardation due to the $\lambda/4$ plate and the

terahertz electric field induced one. The terahertz electric field modulates the birefringence of the ZnTe (110) sensor crystal. This in turn modulates the polarization ellipticity of the optical probe beam passing through the crystal. The ellipticity modulation of the optical probe beam can then be analyzed to provide information on both the amplitude and phase of the applied electric field [72].

As known that the polarization of both the terahertz and optical probe beams are aligned parallel to the y' axis at the input face of the crystal. Thus the field of the probe beam before incident the crystal, we have

$$\vec{E}_{in} = E_p \hat{y}',$$ · Eq. (3-26)

From Eq. (3-19), we can write for the transformation

$$\vec{E}_{in} = \frac{E_p}{\sqrt{2}}(\hat{y}'' - \hat{z}'').$$ Eq. (3-27)

Upon emerging from the output face, the y'' and z'' components have acquired, according to Eq. (3-25), a relative phase shift (retardation) of Γ radians. The total field emerging from the output face of the ZnTe crystal is

$$\vec{E}_{out} = \frac{E_p}{\sqrt{2}}(\hat{y}'' - \hat{z}'' e^{i\Gamma}),$$ Eq. (3-28)

After passing through the Wollaston polarizer, the two mutually orthogonal linearly polarized beams, $E_{out,y'}$ and $E_{out,z'}$, can be separated:

$$E_{out,y'} = (\vec{E}_{out} \cdot \hat{y}')$$

$$= [\frac{E_p}{\sqrt{2}}(\hat{y}'' - \hat{z}'' e^{i\Gamma}) \cdot (\frac{1}{\sqrt{2}}\hat{y}'' - \frac{1}{\sqrt{2}}\hat{z}'')]$$

$$= \frac{E_p}{2}(e^{i\Gamma} + 1),$$ Eq. (3-29)

$$E_{out,z'} = (\vec{E}_{out} \cdot \hat{z}')$$

$$= [\frac{E_p}{\sqrt{2}}(\hat{y}'' - \hat{z}'' e^{i\Gamma}) \cdot (\frac{1}{\sqrt{2}}\hat{y}'' + \frac{1}{\sqrt{2}}\hat{z}'')]$$

$$= \frac{E_p}{2}(e^{i\Gamma} - 1),$$

Eq. (3-30)

The transmission in y' and z' axe can be express as:

$$t_{y'} = \frac{\left|E_{out,y'}\right|^2}{\left|E_{in}\right|^2} = \frac{1}{2}(\cos\Gamma + 1),$$

Eq. (3-31)

$$t_{z'} = \frac{\left|E_{out,z'}\right|^2}{\left|E_{in}\right|^2} = \frac{1}{2}(1 - \cos\Gamma) = \sin^2(\frac{\Gamma}{2}),$$

Eq. (3-32)

The transmission as a function of the retardation Γ is plotted in Fig. 3-14. Owing to the small terahertz electric fields ($\Gamma \ll 1$), we used a quarter-wave plate to impart a $\Gamma_B = \pi/2$ optical bias to the probe beam, which allows the system to be operated in the linear range. Finally the transmission is thus

$$t_{y'} = \frac{1}{2}[\cos(\Gamma + \Gamma_B) + 1] \cong \frac{1 - \Gamma}{2},$$

Eq. (3-33)

$$t_{z'} = \sin^2(\frac{\Gamma + \Gamma_B}{2}) \cong \frac{1 + \Gamma}{2},$$

Eq. (3-34)

If the incident optical intensity is I_p, then, the corresponding output intensity in y' and z' axe can be express as:

$$I_{y'} \cong (\frac{1 - \Gamma}{2})I_p,$$

Eq. (3-35)

$$I_{z'} \cong (\frac{1 + \Gamma}{2})I_p,$$

Eq. (3-36)

The optical intensity modulation using balanced photodiodes denoted by ΔI is detected as following:

$$\Delta I = I_{z'} - I_{y'} = \Gamma I_p,$$

Eq. (3-37)

Upon Eq. (3-25) substitution in Eq. (3-37), yield

$$\Delta I = I_p \frac{\omega n^3 E_{THz} \gamma_{41} L}{c},$$

Eq. (3-38)

Equation (3-38) shows that the signal from the balanced detectors is proportional to the applied terahertz field. Thus, by the variation of the delay between

terahertz and optical probe beams the whole time profile of the pulse can be traced.
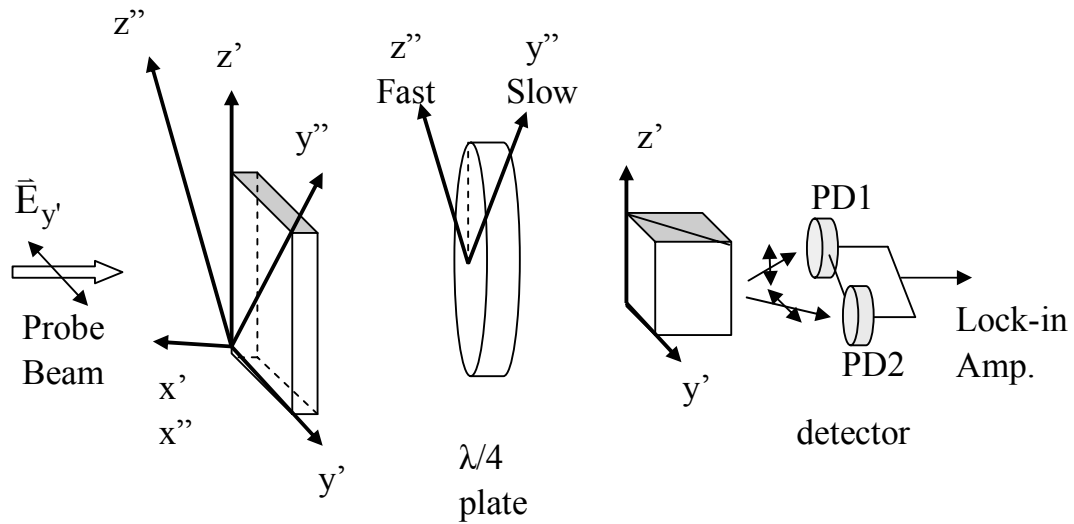
FIG. 3-13 *Experimental setup for detection of the electric field of terahertz pulse. Both the terahertz beam and the probe beam are focused on a ZnTe crystal. After passing through the ZnTe sensor crystal, the probe beam then passes through a quarter-wave plate and a polarizing beam splitter. A differential detector measures the signal difference, which is proportional to the terahertz electric field.*
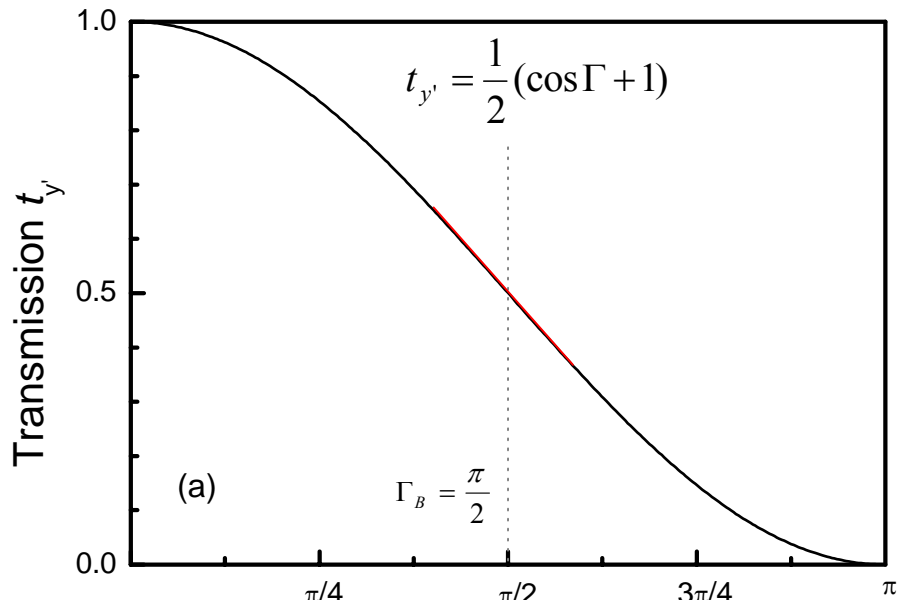
FIG. 3-14(a) and (b) *The transmission as a function of the retardation* Γ.

3.5 Summary
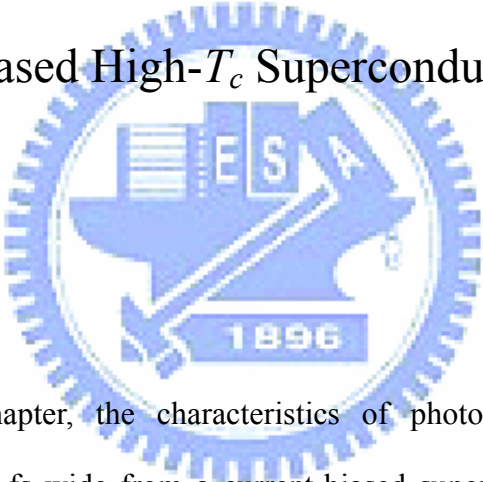
The characteristics of the optically induced bipolar terahertz radiation from biased semi-insulating GaAs photoconductive switches were investigated using a free-space electro-optic sampling technique. The emitted radiation shows a nearly symmetrical waveform with a broad-band frequency spectrum spanning over 0.1–3 THz. It was observed that the bipolar nature 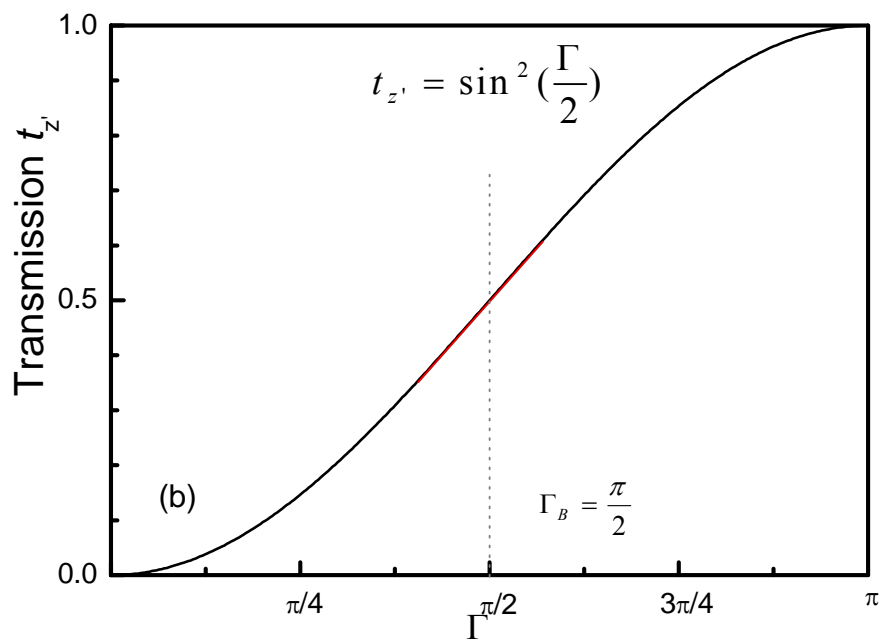and the emitted frequency spectrum distribution remained unchanged on varying the optical excitation fluence, strength of the biased field and the emitter gap spacing. The dynamics of the emitted terahertz transient is in agreement with the optically induced ultrafast charge transport process driven by the biased field.

We have performed measurements and calculations that shown how the efficiency of terahertz detection strongly depends on the orientation of the terahertz polarization with respect to the crystal (001) axis and on the angle between the probe beam polarization and the terahertz polarization.

Chapter 4

Characterization of Photogenerated Terahertz Radiation in Current-Biased High-T_c Superconductors

4.1 Introduction

In this chapter, the characteristics of photogenerated terahertz pulses radiation about 450 fs wide from a current-biased superconducting YBCO bow-tie antenna were investigated using a FSEOS technique. As discussed in the previous chapter, the polarization change of the probe beam occurs when the ZnTe sensor crystal, based on the Pockels effect, is irradiated by the applied terahertz electric field. The terahertz-induced phase retardation of the probe beam is converted into an intensity modulation and detected by using balanced photodiodes. Picosecond electromagnetic pulses were observed [68]. We investigated the performances of the terahertz radiation by measuring the dependence of terahertz radiation on excitation power, bias current, and ambient temperature. The dynamics of the quasiparticles optically induced by the ultrafast laser pulse then determines the performance of the

transient terahertz radiation generated under different operating parameters. Since the terahertz electric field is measured at the backside of substrate, the pulse may be reshaped by the kinetic inductance of the superconducting charge carriers before reaching the detector. By taking into account of the effect of kinetic inductance on the pulse reshaping, our results demonstrate the direct connection between the quasiparticle dynamics and the detected terahertz radiation. Indeed, by transforming the pulse shape back to the original circumstance, the time integral of the original terahertz pulse reveals a fast decreasing component of about 1.0 ps and a slower recovery process, with a value of 2.5 ps for the optically induced supercurrent modulation, consistent with that obtained from the optical reflectivity measurements. These results not only remove the discrepancies just mentioned in chapter 1, but also indicate that the terahertz generation is a direct manifestation of quasiparticle dynamics in response of the optical excitations.
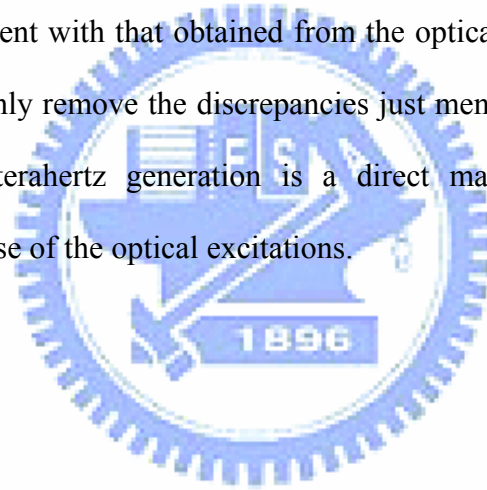
4.2 Experimental setup

Schematic illustration of the experimental setup of terahertz generation in YBCO thin films are shown in Fig. 4-1(a). Other details were described in chapter 2.
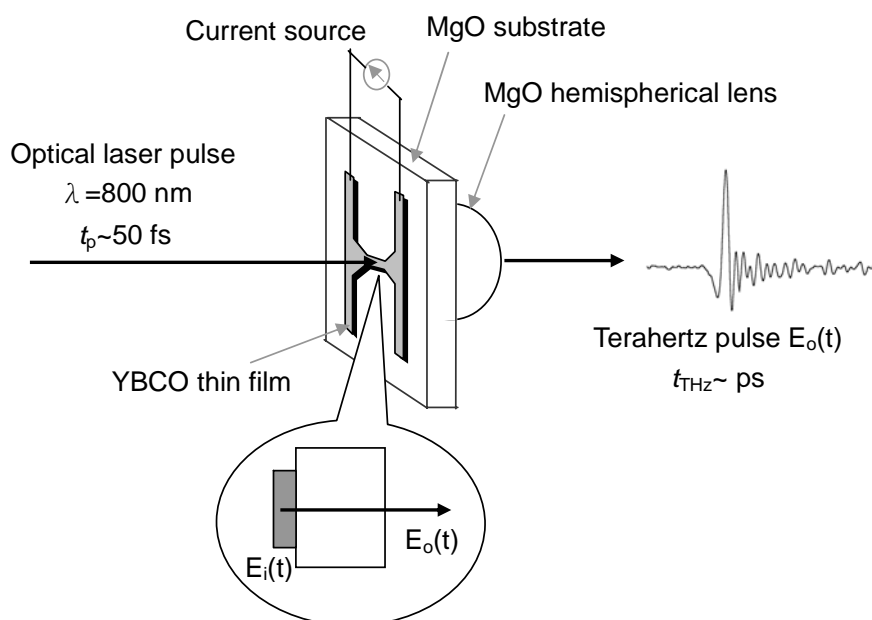
FIG. 4-1(a). *Schematic diagram of the free-space terahertz generation in the experimental setup in which t_p and t_{THz} with pulse durations of laser and terahertz pulse, respectively. The enlarged portion denotes the matter of the original terahertz pulses $E_i(t)$ and the reshaping of terahertz pulses $E_o(t)$ that transmission through the superconducting YBCO film and substrate in the time domain.*

The generation and detection of terahertz radiation was realized by using FSEOS technique [Fig. 4-1(b)]. A cw argon-laser-pumped, compact, mode-locked Ti:sapphire laser (Femtosource C20) provides 20-fs optical pulses at 800 nm (1.55 eV) with a 75 MHz repetition rate. The pump beam focused into a spot size about 50 μm in diameter was modulated by a mechanical chopper which operated at 1.3 kHz and incident normal to the center bridge of YBCO bow-tie antenna. The electric field of the terahertz pulse was sampled by scanning the delay between the pump and probe beam. The superconducting YBCO bow-tie antenna, triggered by femtosecond optical laser pulses, radiates the terahertz signals. The terahertz radiation emitted through the

backside of the MgO substrate was collimated by an MgO hemispherical lens with a diameter of 5 mm attached to the backside of the substrate. The terahertz radiation was then passed through a 3-mm-thick vacuum window made of Teflon^{TM} and focused by a pair of off-axis paraboloidal mirrors onto the 1.0-mm-thick ZnTe (110) sensor crystal. For low-temperature measurements, the samples were cooled using a Janis flow-through cold-finger cryostat. In the detection segment, the orientation dependence of terahertz beam detection in ZnTe crystal was accomplished by using an undoped SI-GaAs photoconductive switch (as discussed in chapter 3). The shape of terahertz pulses remains, but the peak amplitude of the signal and the polarity vary with the probe beam polarization and the terahertz beam polarization with respect to the (001) axis of the (110)-oriented ZnTe crystal. The results were then used to determine the optimal operating parameters for our terahertz detection setup [79].
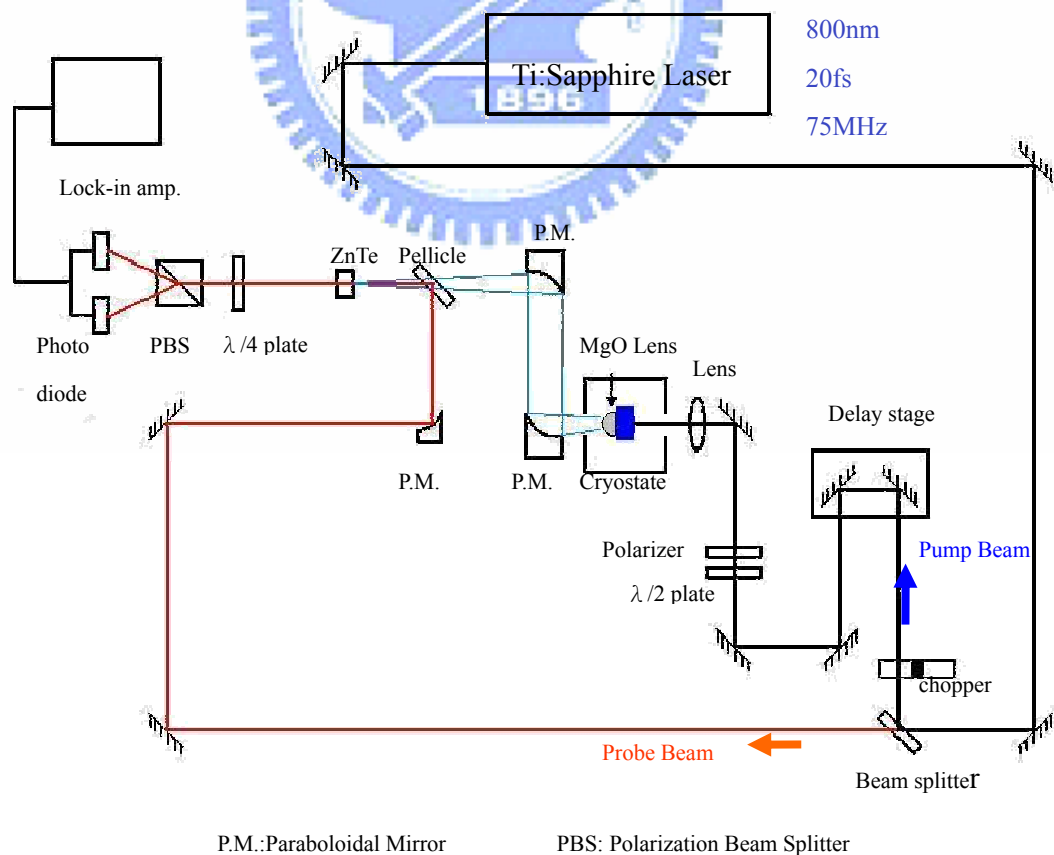

FIG. 4-1(b). *Experimental setup of the generation and detection of terahertz radiation.*

4.3 Photogenerated transient terahertz radiation

4.3.1 Typical time profile and frequency spectrum of terahertz pulse

The freely propagating terahertz pulses generated from optically excited superconducting YBCO thin films were measured by free-space electro-optic sampling system. The typical photogenerated terahertz radiation (terahertz electric field pulse) as a function of the scanning delay time obtained from a current-biased superconducting YBCO bow-tie antenna measured at 60 K was showed in Fig. 4-2. The optical excitation power (I_{power}) and biased current (I_b) were 100 mW and 180 mA, respectively. A sharp pulse about 450 fs wide is observed. Above T_c, the terahertz radiation cannot be observed due to the high electrical resistance of the antenna. A representative amplitude spectrum derived by Fourier transform of the terahertz waveforms is shown in Fig. 4-3. The radiation frequency spectrum extends from 0.1 to 4 THz with its peak intensity at 0.83 THz. The bandwidth at half-maximum (BWHM) of the frequency spectrum is around 1.2 THz. The corresponding atmospheric water vapor absorption at 1.1, 1.4, and 1.7 THz was observed.
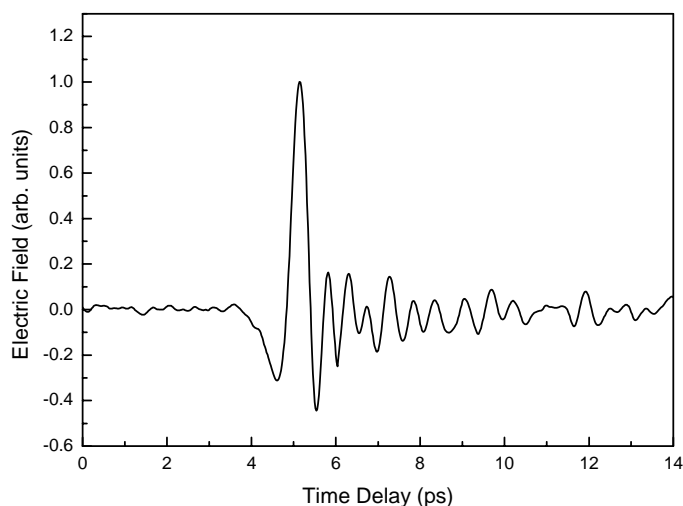
FIG. 4-2. *Measured transient terahertz radiation from superconducting YBCO bow-tie antenna at 60 K. The excitation power and bias current were 100 mW and 180 mA, respectively.*

FIG. 4-3. *Corresponding frequency spectrum by Fourier transform of the terahertz waveforms. The inset shows the log scale of the spectrum.*

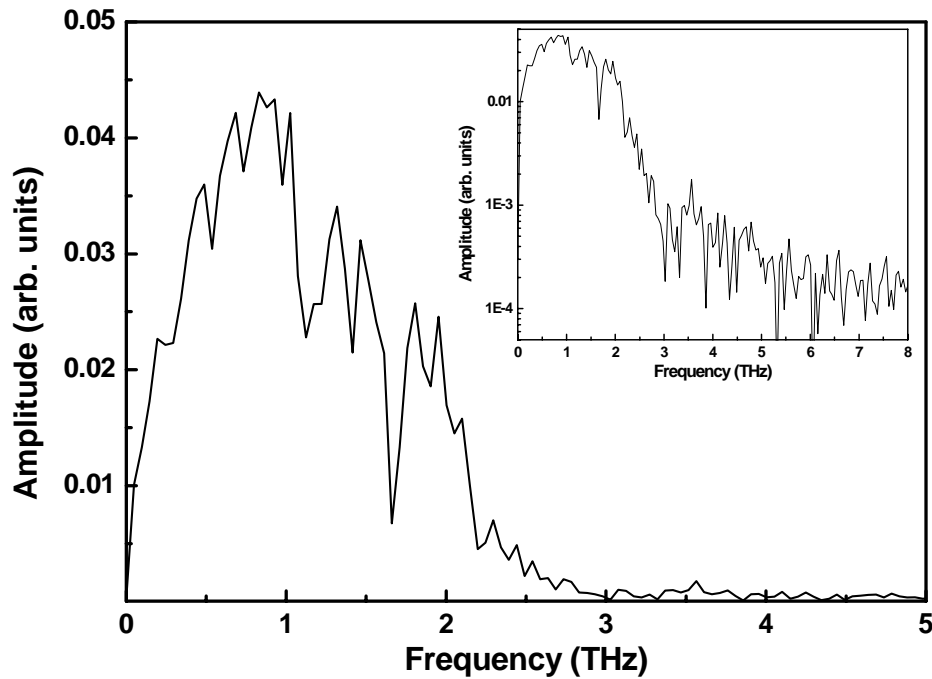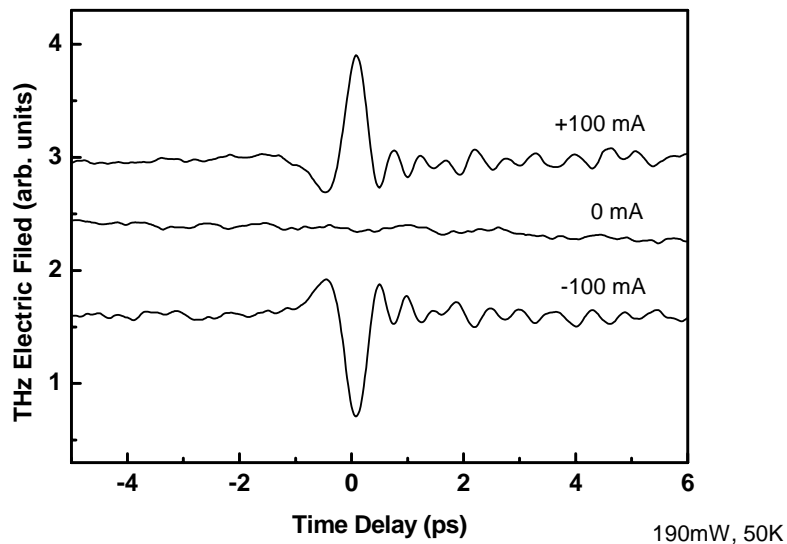FIG. 4-4. *Measured transient terahertz radiation from superconducting YBCO bow-tie antenna at 50 K. The polarity of the terahertz waveforms measured with bias current of +100 mA and –100 mA. No signal is observed when no bias current is applied.*

4.3.2 Polarity of the terahertz waveforms

Figure 4-4 shows the terahertz radiation waveforms measured with bias current of +100 mA, 0 mA, and −100 mA. The excitation power is 190 mW at 50 K. The figure shows that the polarity of the terahertz electric field is reversed by reversing the bias current direction, and that no signal is observed when no bias current is applied, revealing the essentiality of the optically induced transient supercurrent density. This consequence can be understood from Eq. (1-1), in which the change of photocurrent with time can be treated as the supercurrent transient in superconductors.

4.3.3 Radiation mechanism of superconductors

We note that in order to describe the generation of the terahertz radiation, two major points have to be clarified. The first one is the carrier dynamics giving rise to the generation of the terahertz electric field pulse, and the other one is the output coupling of the radiation from the superconducting thin films.

As far as classical electromagnetic dynamics is concerned, a far-field radiated terahertz electric field is proportional to the time derivative of the net current as indicated in Eq. (1-1). From the results just presented, it is natural to suggest that the terahertz electric field E_{THz} from YBCO films is generated by the temporal modulation of the supercurrent density $\partial J_s / \partial t$. Within the framework of the two-fluid model, the bias current density J_s can be described as

$$J_s = e n_s v_s,$$ Eq. (4-1)

Where e is the charge of the carrier, n_s is the density of the supercarriers (equal to the twice of the Cooper pairs density) and v_s is the velocity of the Cooper pairs. J_s is

expected to change when an optical transient is illuminated at the bridge region. The optical-induced transient of the supercurrent density with time in the illuminated region of the superconducting bridge can be expressed as

$$\frac{dJ_s}{dt} = n_s e \frac{\partial v_s}{\partial t} + e v_s \frac{\partial n_s}{\partial t} , \qquad \text{Eq. (4-2)}$$

The first term in the right-hand side of the equation corresponds to the acceleration of the supercarriers by the field of the kinetic inductance, which operates so as to keep the current constant against the reduction of supercarriers, can be ignored due to the small affect in the subpicosecond region expected (since the optical excitation does not produce an intense charge imbalance in the excited area) [80]. The second term in the right-hand side of the equation describing the photoexcitation of the Cooper pairs into hot quasiparticles and the avalanche generation of the quasiparticles by the hot quasiparticles through electron-electron and electron-phonon interactions, and then the subsequent recovery of the supercurrent density results from quasiparticle recombination. Namely, the transient waveform can be interpreted as the first derivative of the supercurrent density n_s in the films.

$$E_{THz} \propto \frac{dJ_s}{dt} \propto e v_s \frac{dn_s}{dt} = \frac{J_s}{n_s} \frac{dn_s}{dt} , \qquad \text{Eq. (4-3)}$$

Thus, the peak amplitude of the emitted terahertz radiation is proportional to the transient of the supercurrent as well as the transient of the supercurrent density. It was ever been reported that using the method of the radiation power is proportional to the square of the bias current density at the laser spot position, the two-dimensional supercurrent distribution can be obtained form the intensity distribution of terahertz radiation by scanning the laser spot [81].

Based on the Eq. (4-3), the peak amplitude change in J_s and n_s can be expressed as

$$E_{THz}(peak) \propto \Delta J_s \cong ev_s \Delta n_s = \frac{J_s}{n_s} \Delta n_s \propto J_s \cdot I_{power} , \qquad \text{Eq. (4-4)}$$

Where Δn_s is proportional to the optical excitation power I_{power} and n_s (The broken Cooper pairs is proportional to fraction of the supercarriers). The formula suggested that the peak amplitude of the emitted terahertz radiation will proportional to the optical excitation power and the bias current.

4.4 Performances of transient terahertz radiation generated under different operating parameters

4.4.1 Optical excitation power dependence

Figure 4-5 shows plots of a series of transient terahertz waveforms as a function of excitation power for the superconducting YBCO bow-tie antenna. Obviously, the terahertz amplitude of emitted fields increased with increasing the excitation power and the pulse shapes have no significant excitation power dependence. The peak amplitude of emitted terahertz fields increases linearly with optical excitation power shown in Fig. 4-6. The results show that the peak strength of the terahertz fields is proportional to the transient shrinkage of the density of the supercarriers. Namely, it suggested that the transient shrinkage of the density of the supercarriers is considered to be proportional to the optical excitation power [as indicated in Eq. (4-4)]. The peak frequency and the BWHM of the frequency spectrum derived by Fourier transforming the picosecond pulses (in this case, I_{power}=200 mW and I_b=100 mA at 30K) are the same as the earlier results.

In addition, it is evident that the modulation after the main pulse is always present over the whole range of optical excitation power studied, showing that the modulation behaviors have no relationship with the optical excitation power.
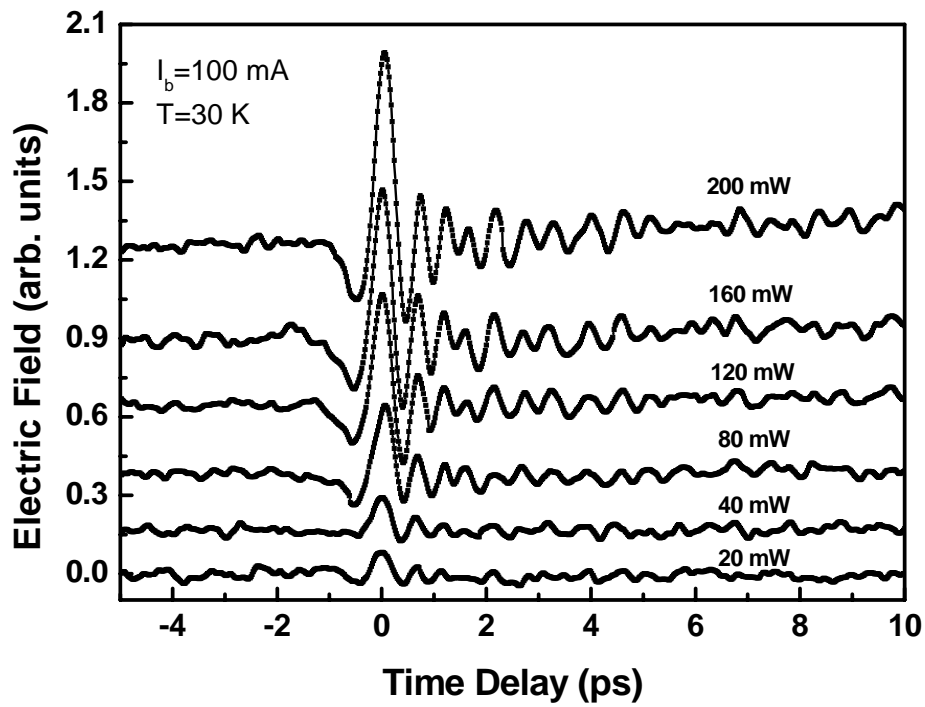
FIG. 4-5. *Series of detected transient terahertz waveforms as a function of excitation power.*
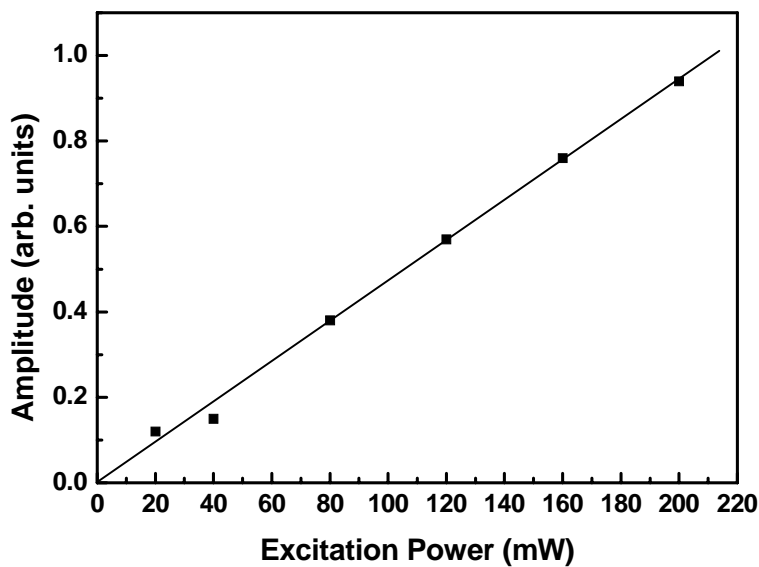
FIG. 4-6. *The peak amplitude of emitted terahertz fields increases linearly with optical excitation power (the solid line is a guideline).*

4.4.2 Biased current dependence

　　Here, we primarily concentrate on the analysis of the radiation waveform behaviors under different bias current parameters. At lower measuring temperature, the bias current dependence of the generated terahertz radiation is illustrated in Fig. 4-7. The optical excitation power and temperature were 190 mW and 30 K, respectively. Similarly, as well as the excitation power, the amplitude of terahertz electric fields increased with increasing the bias current. The peak strength of the transient terahertz radiation increases linearly with bias current as shown in Fig. 4-8. The fact that the performances of the dependence on excitation power and·bias current, corresponding to the observation of the transient change in the density of the supercarriers, evidencing the superradiant character of the emission [8].
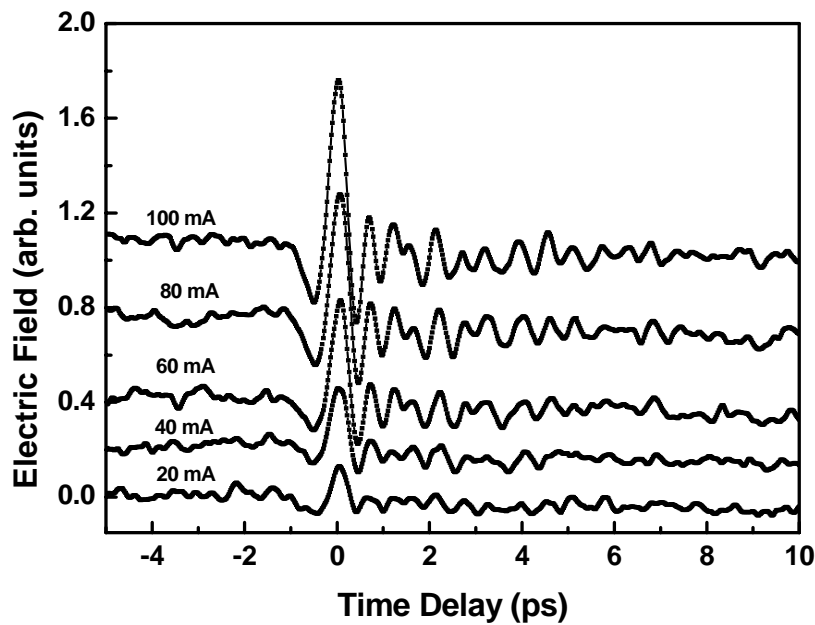
FIG. 4-7. *The bias current dependence of the generated terahertz radiation. The excitation power is 190 mW measured at 30 K.*
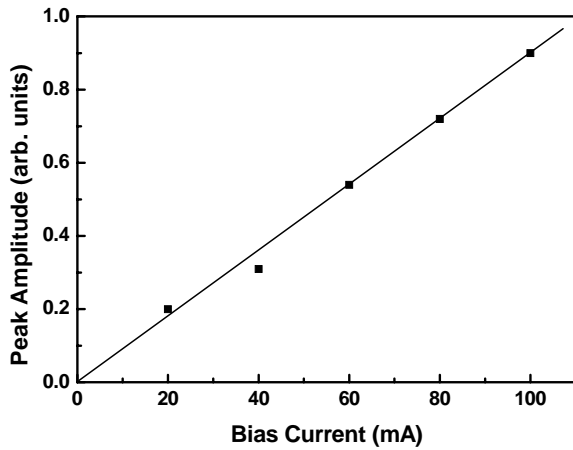
FIG. 4-8. *Bias current dependent of detected terahertz peak amplitude. The solid line is drawn to indicate the trend.*
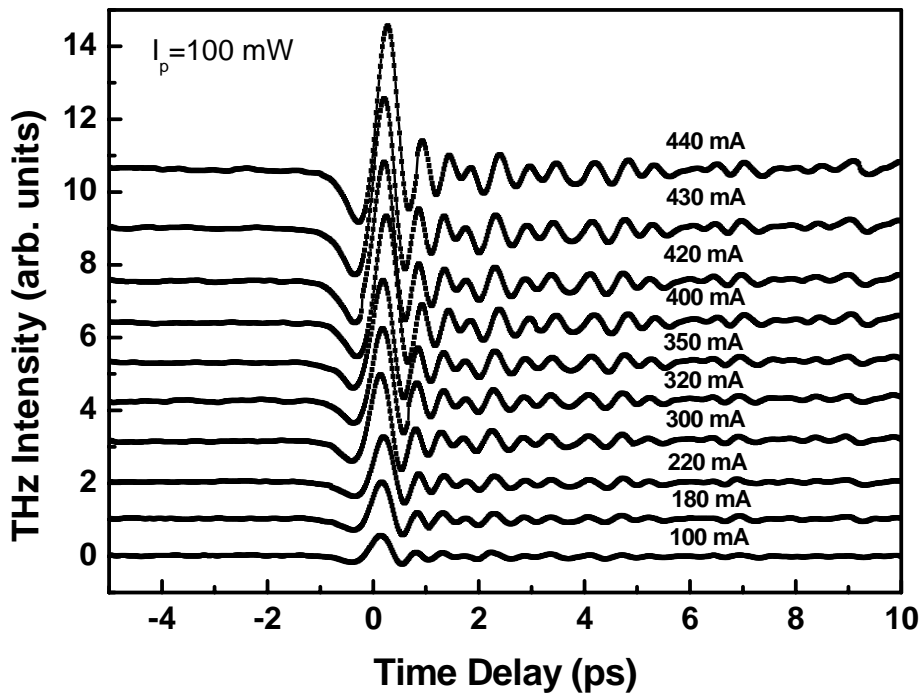
FIG. 4-9. *The results of the bias current dependence of the transient terahertz radiation with higher measuring temperature 60 K.*

With regard to the higher measuring temperature, the results of the bias current dependence of transient terahertz radiation is illustrated in Fig. 4-9 (I_{power}=100

mW at 60 K). The amplitude of terahertz fields increased rapidly with increasing the bias current. The peak amplitude of the radiation increases in proportion to the bias current up to about 200 mA as shown in Fig. 4-10. Beyond this value, thought it is still much less than the critical current I_c (I_c=650 mA at 60 K), the peak amplitude increases rapidly with the bias current. The reason induced the deviation from the linear dependence of the peak strength of the radiation on bias current may be attributed to the flux flow effect [82]. The resistive state resulted from laser heating or flux flow would produce a normal region that weakens the screening effect and absorption in the YBCO films and hence increases the emission efficiency of the terahertz radiation.

FIG. 4-10. *The bias current dependence of the peak amplitude of the radiation at different measure temperature. The straight line is a guideline.*

Finally, the bias current dependence of the peak amplitude of the radiation at different temperature were shown in Fig. 4-10. At lower measuring temperature, excitation power was 100 mW at 30 K, the peak amplitude of the radiation increases in proportion to the bias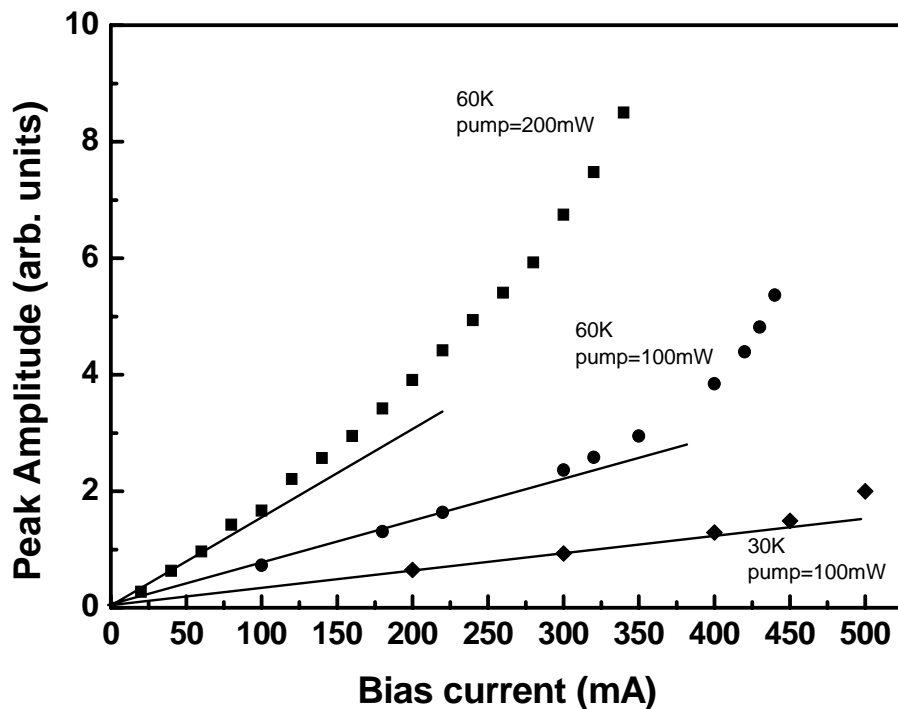 current up to about 400 mA. As measuring temperature increased to the 60 K, the bias current in the linear operating region was up to about 200 mA. Beyond this value, the peak amplitude increases rapidly with the bias current as discussed earlier. Furthermore, higher measuring temperature will yield higher peak amplitude of the radiation even under the same excitation power and bias current (will be discussed in the next section). In addition, as the excitation power was 200 mW at 60 K, the maximum of the linear operating region of the bias current will drop lower to about 60 mA. In a word, the tunable range of the linear region of the peak amplitude of the radiation varied with the bias current will be related to the excitation power and ambient temperature.
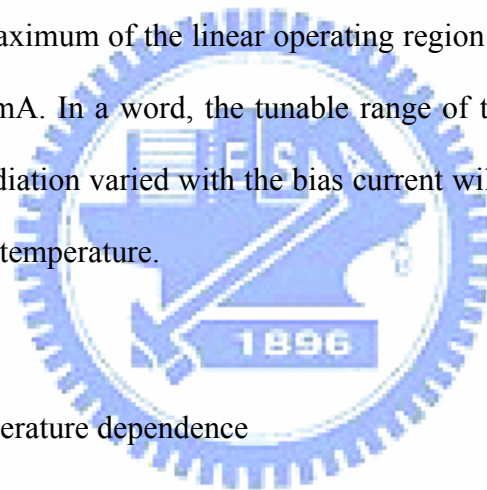
4.4.3 Ambient temperature dependence

The dynamics of the emitted terahertz transient related to the nonequilibrium superconductivity is investigated by measuring the dependence of the radiation on optical excitation power, and bias current. The peak strength of the transient terahertz radiation was found to increase linearly with optical excitation power as well as the bias current, indicating the superradiant character of the emission. Next, it would be interesting to see whether the pulse shape changes with ambient temperature. Fig. 4-11 shows a series of emitted terahertz pulses obtained at several temperatures. The phase and the shape of the transient change significantly at different ambient temperatures. It is evident that the shape of the transient terahertz pulses is almost the same in each case, except for the 70 K results, in which the shape after the main pulse

followed a slower component with a characteristic time of about 2.5 ps. It is noted that the phase of the pulse also shifts with increasing the temperature. With regard to the peak amplitude of terahertz signals, the radiation amplitude rapidly increases with increasing temperature. This phenomenon has been attributed to the reduced superconductor energy gap and associated temperature dependent transmission and absorption coefficients [8,83].
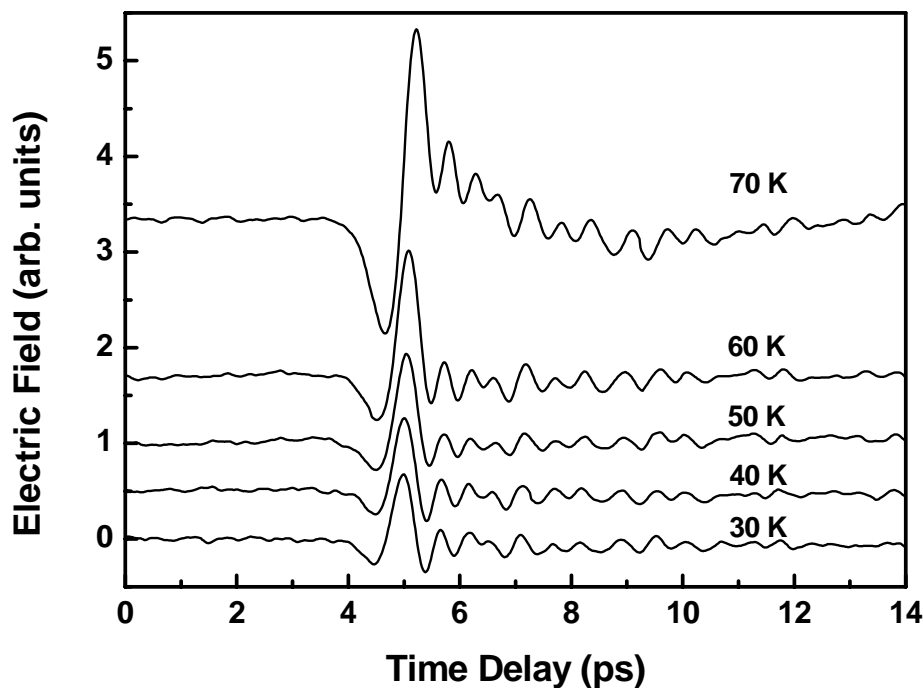
FIG. 4-11. *Temperature dependence of emitted terahertz waveforms. The excitation power is 190 mW. The dramatic change in pulse shape is shown in the figure.*

Usually, the optical reflectivity measured by the optical pump-probe method has femtosecond time response while the gap opening is manifested by a rapid increase in the amplitude of the photogenerated transient reflectance in the superconducting state. The ultrafast rise of the reflectivity after excitation of the YBCO at t=0 ps is attributed to Cooper pairs breaking and the subsequence decrease

of the reflectivity results from quasiparticle recombination [19-21]. The recombination time, which has the value of 1.5-2.5 ps as reported by Jaekel *et al.*, shows a crucial increase (faster quasiparticle dynamics at low temperatures) up to the value of 2.5 ps as the ambient temperature increases toward T_c [8].

Recently, Demsar *et al.*, demonstrated that the transient reflectivity change has identified two distinct characteristic relaxation times in the superconducting state [13], As shown in Fig. 4-12, it displayed the real-time measurements of the quasiparticle relaxation dynamics of YBCO with femtosecond time-domain spectroscopy. It reveals a break in the slope near $t = 3$ ps, indicating the presence of two distinct relaxation times, one with $\tau_B \approx 0.5$ ps and the other with $\tau_A \approx 3$ ps. The divergent performance of the quasiparticle recombination is generally attributed

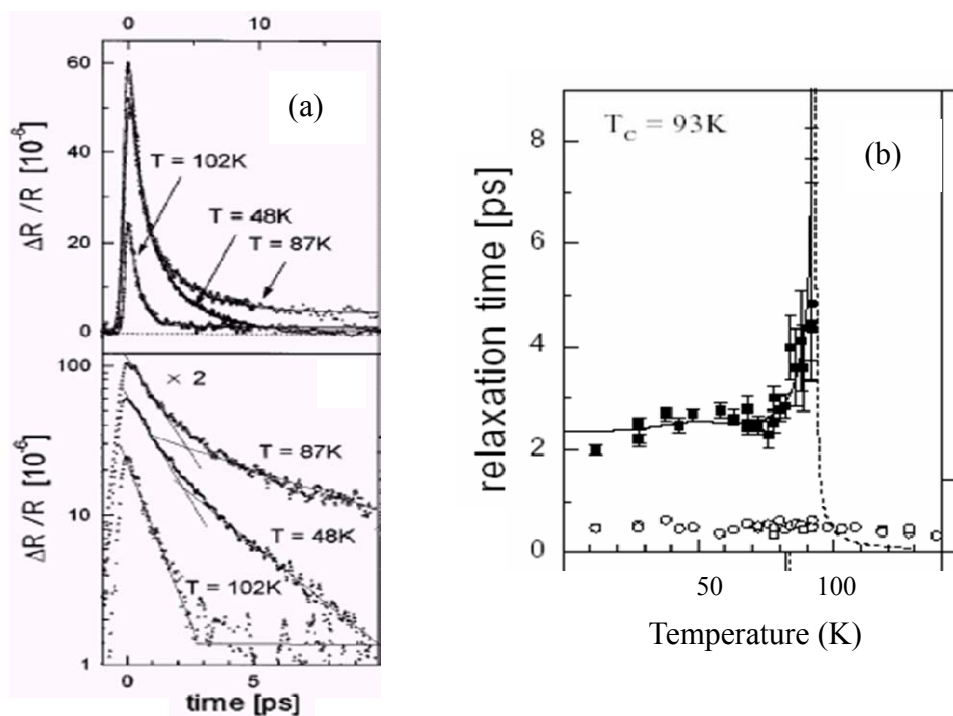FIG. 4-12. *(a) The photoinduced reflection as a function of time. The break in the slope indicate the presence of two distinct relaxation times, one with ~0.5 ps and the other with ~2.5 ps, (b) The relaxation times as a function of temperature.*

to the manifestation of superconducting gap. Besides, Williams *et al.* demonstrated the superposition of the kinetic-inductive and the resistive hot-electron photoresponse mechanisms to explain the transformation of the voltage transient single-picosecond bipolar waveform to a broad photoresponse pulse at higher optical powers near T_c [84].

In the present case, we interpret the emitted transient terahertz radiation as the ultrafast supercurrent modulation. The transient waveform can be interpreted as the time derivative of the supercurrent in the films, and the time integral of the observed *E*-field amplitude correspondently gives the current transient in the time domain. As can be seen, the decrease in the current is determined by multiple excitation of the quasiparticles due to hot-carrier thermalization. The decrease in the number of Cooper pairs results in the decrease in the supercurrent. The current recovery may be explained in terms of the recombination of quasiparticles into Cooper pairs. The performance of the recovery processes is nearly the same well below T_c indicated that there exists a similar characteristic time of the quasiparticle recombination. An unphysical time scale was obtained, however, if one interprets the transient waveforms shown in Fig. 4-11 as direct manifestation of $\partial J_s / \partial t$. The response time obtained this way appears to be too fast for supercurrent transient associated with quasiparticle dynamics. Similar difficulties have been encountered when trying to assign the subpicosecond recovering time to quasiparticle recombination response time [9,29], which is about an order of magnitude shorter than normally conceived values [13,14]. The discrepancies mentioned will be discussed in the next section.

4.5 The origin of photogenerated terahertz radiation emitted from current-biased superconducting YBa$_2$Cu$_3$O$_{7-\delta}$ thin films

4.5.1 Kinetic inductance-induced pulse reshaping effect

In the two-fluid model we have treated the frequency-dependent conductivity of superconductor, obtained by the current flow at a point response to an applied field, as composed of two parts: one that is due to normal carriers whose motion is governed by the Drude equation and one that is due to superconducting carriers whose motion is determined by the London equation. Each carrier type has its own frequency-dependent conductivity and that the total conductivity is given by the sum of the normal and superconducting parts,

$$\sigma(\omega,T) = \sigma_n(\omega,T) + \sigma_s(\omega,T) , \qquad \text{Eq. (4-5)}$$

where the subscripts n and s refer to normal and superconducting, respectively. The temperature T sets the relative ratio of the normal and superconducting carrier densities, $n_n(T)$ and $n_s(T)$, respectively. The expression for the frequency-dependent conductivity of the superconducting carriers moved in accordance with the London equation is given as,

$$\sigma_s(\omega) = i \frac{n_s e^2}{m^* \omega} , \qquad \text{Eq. (4-6)}$$

We note that the conductivity is pure imaginary. The resistivity is therefore also imaginary and is linearly proportional to ω, responding like a reactive inductance to an applied field. The frequency-dependent conductivity $\sigma_s(\omega)$ of the superconducting carriers is purely imaginary, indicating that the superconducting films may act as an ideal inductor. This property is referred to as kinetic inductance, since the effect is a consequence of the superconducting carrier's kinetics [18,28,29,66]. In general, the kinetic inductance of charge carriers is neglected since

the intrinsic impedance is usually dominated by the resistance (in normal state). In a superconducting state, however, the kinetic inductance becomes more significant and must be considered as an important parameter. Thus, the phase sensitivity of the terahertz pulse spectrometer allows us to observe directly the kinetic inductance of the carriers.

The experimental results are illustrated in Fig. 4-13 which shows the time-domain spectroscopy taken on the YBCO film. Notice that there is a dramatic change of the pulse shape in Figs 4-13(a) and 4-13(c) for results measured at 50 K and 70 K, respectively. This pulse reshaping is a direct result of the superconductor's kinetic inductance. The pulse reshaping effect can be understood with the aid of a transmission line analog [Fig. 4-14]. The superconducting film can be modeled as a shunt inductor having complex impedance given by the film's surface impedance
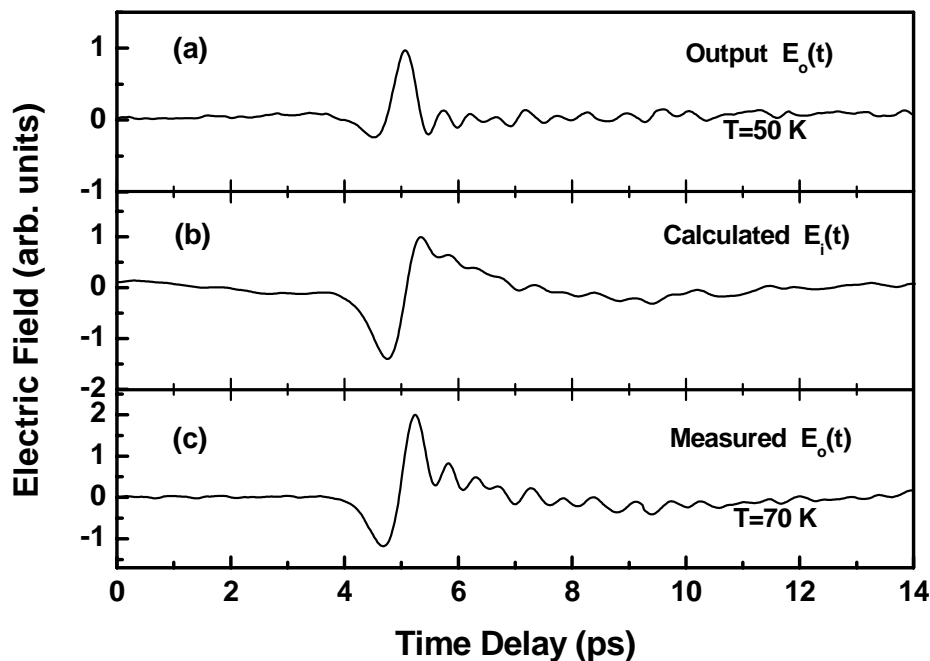

FIG. 4-13. *(a) Measured (output) terahertz pulse $E_o(t)$ at 50 K; (b) original terahertz pulse $E_i(t)$ obtained by Eq. (4-7) using the data in (a); (c) measured terahertz pulse at 70 K.*
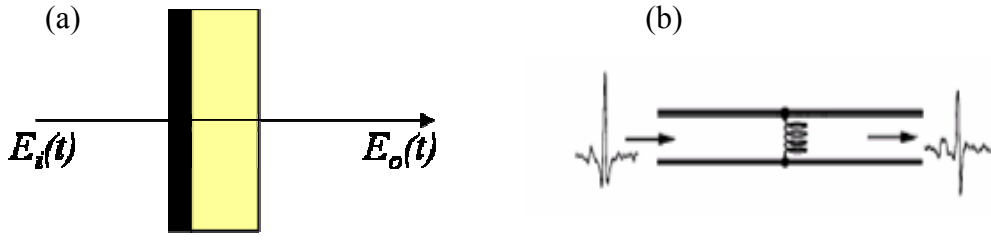
FIG. 4-14. *(a) Schematic representation of structure of the samples. The thin superconducting film (~110 nm) lies on top of the 0.5-mm-thick MgO substrate, (b) Transmission line analog to the transmission of a terahertz pulse through a superconducting thin film. The terahertz pulse enters from the left, travels past the shunt inductance (representing the superconductor's kinetic inductance), and exits on the right [32].*

$Z = -i\omega L$ [32], it acts as a high-pass filter. It presents a short circuit for low frequencies, whereas high frequencies can pass unattenuated. The output (measured) electric field of the terahertz pulse is determined by the response of the film and the dielectric properties of the substrate. MgO substrate turns out to be an excellent material with sufficiently low loss to allow for the extended propagation of subpicosecond electromagnetic pulses. The influence of the substrate on pulse shape can be neglected. In order to yield the original terahertz pulse [$E_i(t)$ denoted in the enlarged graph of Fig. 4-1(a)], which emitted from the superconducting microbridge, propagated through the superconducting film itself, pass through the substrate, and lens, and then transmitted to the free space, the output terahertz electric field $E_o(t)$ is transformed via a transfer function. The transfer function $T(\omega)$, relating the original pulse $E_i(\omega)$ and output pulse $E_o(\omega)$, is expressed as [32]

$$T(\omega) = \frac{E_o(\omega)}{E_i(\omega)} = \frac{2}{2 + Z_0/Z} \propto (-i\omega),$$ 　　　　Eq. (4-7)

where Z_o is the characteristic impedance of the transmission line and set to equal to the vacuum impedance. In the terahertz spectral range $Z_o \gg Z$, yielding

62

$T(\omega) \propto (-i\omega)$. The pulse $E_o(t)$ is Fourier transformed to get $E_o(\omega)$, divided by $(-i\omega)$, and inversely Fourier transformed to yield $E_i(t)$.

The calculated pulse $E_i(t)$ (the original one) is shown in Fig. 4-13(b). *This original pulse has the shape of the initial terahertz electric field that is not affected by the kinetic inductance of superconducting film itself.* It is interesting to note that the recovered pulse [Fig. 4-13(b)] has a waveform similar to the 70 K result [Fig. 4-13(c)]. It is indicative that for the 70 K result, due to having fewer participating superconducting charge carriers, the effect of kinetic inductance is insignificant. (With the excitation power illuminated in the region of the superconducting bridge, a rise of about 10 K is estimated to drive the actual sample temperature to near T_c.) It appears that the pulse reshaping is a direct result of the superconductor's kinetic inductance. Moreover, the phase of the transient also changes significantly in the time domain and is consistent with that reported earlier [35].

As can be seen in Fig. 4-11, the phase shift of the propagated transient is roughly 240 fs below T_c. Taking the absorption coefficient $\alpha = 1.1 \times 10^{-5}$ cm^{-1} for YBCO thin films, an optical penetration depth of $\delta = 1/\alpha \sim 90$ nm above T_c is estimated. [85] The value of δ will rapidly reduce upon decreasing temperature below T_c due to the variations in the heat capacity as well as the temperature transient irradiated by the laser pulse.

We note that, in the more established coherent terahertz time-domain spectroscopy technique as shown in Fig. 4-15 [1], which uses SI-GaAs photoconductive switch as the terahertz radiation source, similar pulse reshaping of transient terahertz was observed [Fig. 4-16] from a 30-nm-thick YBCO film deposited on NdGaO$_3$ substrate. We take the applicability of the transmission line analog by using a measured terahertz pulse transmitted through the YBCO film for T=90 K [Fig.
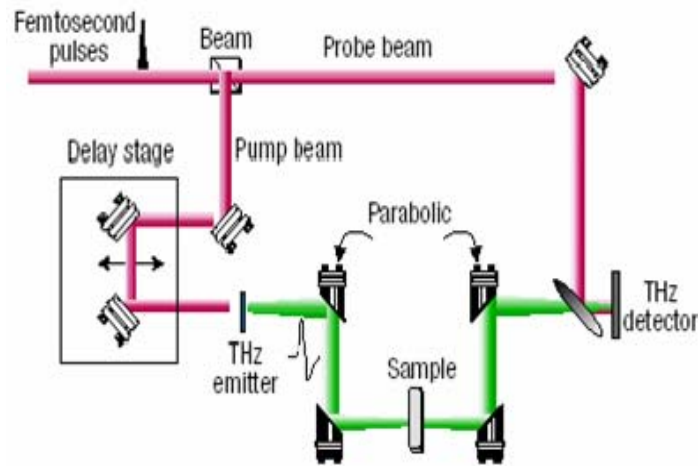
FIG. 4-15. *Illustration of a THz-TDS pump probe system. The ultrafast laser beam is split into pump and probe beams. The pump beam is incident on the terahertz emitter to generate terahertz pulses, and the terahertz pulses are collimated and focused on the target using parabolic mirrors. After transmission through the target, the terahertz pulse is collimated and re-focused on the terahertz electro-optic sampling detector and measure the instantaneous terahertz electric field. A delay stage is used to offset the pump and probe beams and allow the terahertz temporal profile to be iteratively sampled [1].*

4-16(a)] as the input pulse $E_i(t)$. Because this pulse propagates through normal-state YBCO, it follows the same optical path as one through superconducting YBCO but is not modified by the superconducting transfer function [Eq. (4-7)]. The pulse is Fourier transformed, multiplied by $(-i\omega)$, and inverse transformed to yield $E_o(t)$ [Fig. 4-16(b)]. The calculated pulse agrees very well with the experimentally observed pulse, which has been transmitted through the sample in the superconducting state at 70 K [Fig. 4-16(c)]. Hence, the kinetic-inductance induced pulse reshaping effect is existed as the terahertz pulse propagated through superconducting films.
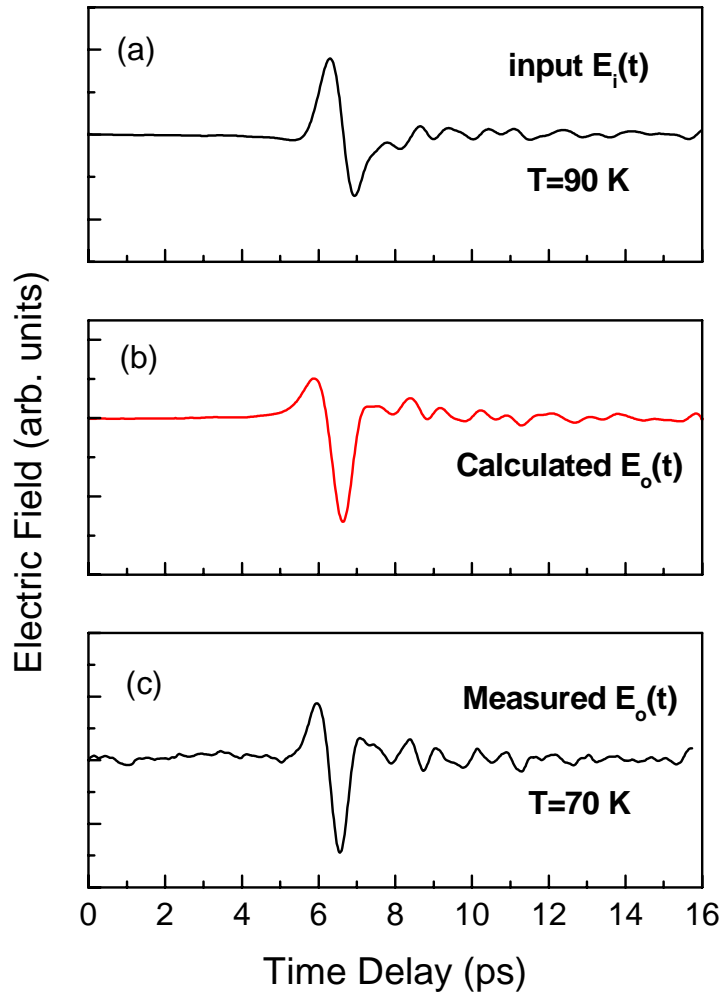
FIG. 4-16. *(a) Measured (output) terahertz pulse* $E_o(t)$ *at 90 K; (b) original terahertz pulse* $E_i(t)$ *obtained by Eq. (4-7) using the data in (a); (c) measured terahertz pulse at 70 K.*

4.5.2 Temperature dependence of the original terahertz pulses from YBCO films

In principle, the inductance L as a function of temperature must be taken into account in the transfer function $T(\omega)$ in Eq. (4-7). In particular, since YBCO is known to have *d*-wave pairing, the nodal regions can lead to strong temperature dependence of the kinetic inductance even well below *Tc* [86]. However, in our case

[Fig. 4-17], although *L* may affect the absolute pulse amplitude, it does not change the genuine characteristics of the radiation. This explains the essentially similar behaviors observed for temperatures below 60 K. For the 70 K result, the influence of temperature dependent inductance and the enhanced optical penetration depth in the superconductor sets in, leading to a very different behavior shown in Fig. 4-11.

Following the previous discussion, the temperature dependence of the original terahertz pulses from YBCO films are obtained and shown in Fig. 4-18. The fact that all the recovered pulses exhibit almost the same behavior not only lends strong support to our previous conjectures, but also is indicative of one essential underlying mechanism.
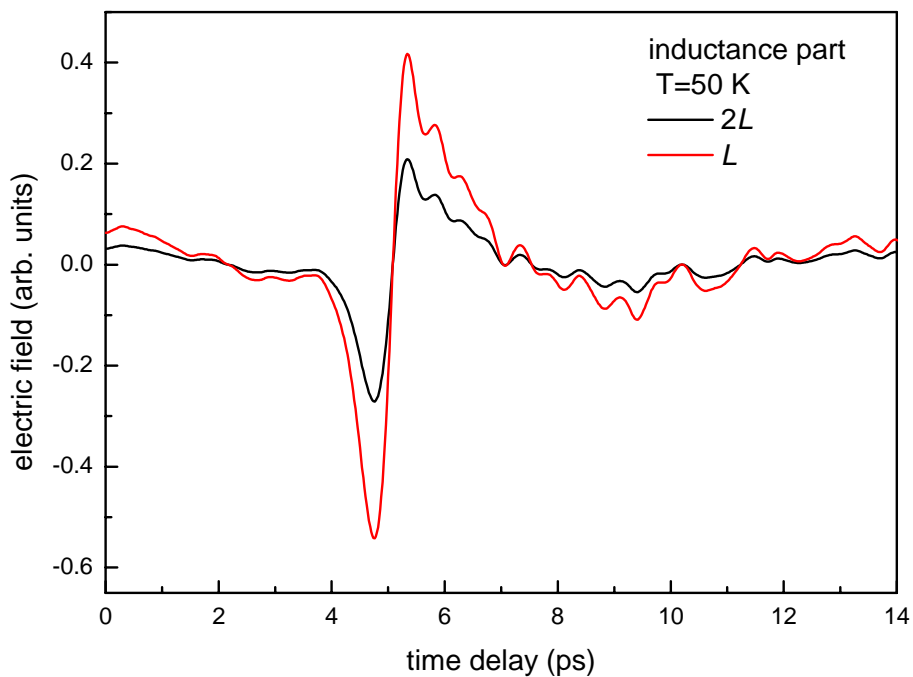
FIG. 4-17. *The magnitude in inductance L may affect the absolute pulse amplitude, it does not change the genuine characteristics of the radiation.*
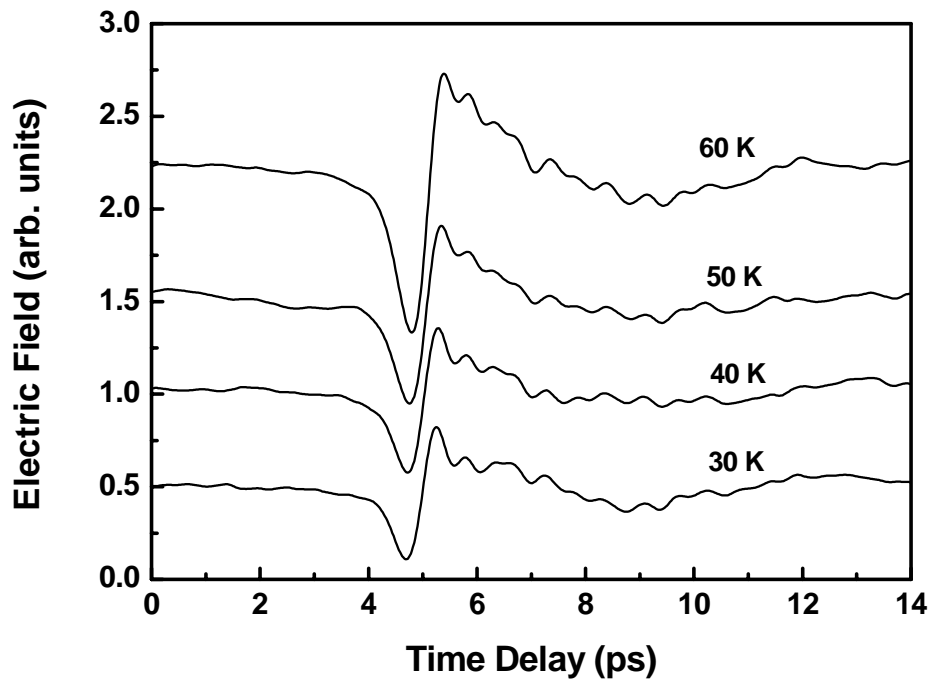
FIG. 4-18. *Temperature dependence of the recovered terahertz pulses calculated from the data in FIG. 4-11 and the transfer function.*

4.5.3 Optically induced supercurrent modulation

Since Eq. (1-1) implies that the optically induced transient of the supercurrent density in the time domain can be subsequently obtained by integrating the recovered emitted electric field pulses as long as the supercurrent transient is the only prominent mechanism giving rise to the observed radiation. In Fig. 4-19, we briefly recap the main observations described so far. With no bias current, no terahertz radiation is observed [Fig. 4-19(a)], indicating again the important role played by the supercurrent density. Figure 4-19(b) shows the pulse directly detected which presumably has been reshaped by the kinetic inductance. By using the transfer function expressed in the form of Eq. (4-7), the recovered pulse is depicted in Fig. 4-19(c). Finally, the irradiated *E*-field pulse is integrated over the sampling time to obtain the supercurrent

density transient ΔJ_s. As is evident from Fig. 4-19(d), ΔJ_s apparently exhibits two

characteristic time scales: a descending time of about 1 ps and a rising time of about

2.5 ps. If we attribute ΔJ_s to be associated mainly with quasiparticle dynamics, the

two characteristic times should correspond to multiple excitation of hot-carrier

thermalization-induced supercarrier reduction and to quasiparticle recombination to

recover supercarriers, respectively. The latter usually is related to the superconducting
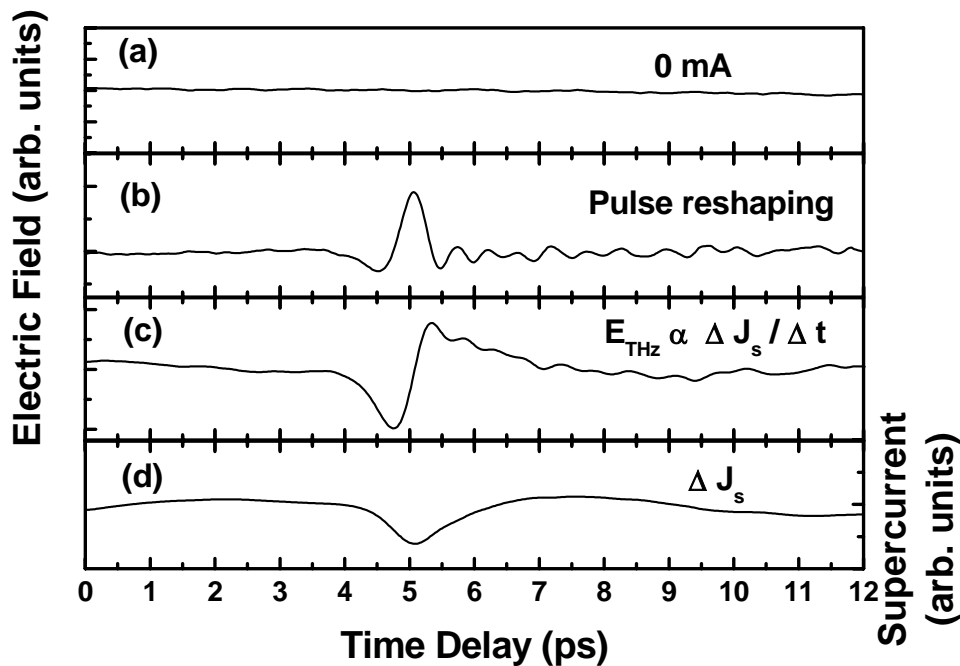
FIG. 4-19. *A recap of terahertz generation related to nonequilibrium superconductivity: (a) no terahertz signal with zero bias current; (b) the detected "raw" terahertz radiation; (c) the recovered terahertz radiation after removing kinetic inductance effect; (d) the "actual" supercurrent transient obtained by integrating the recovered radiation pulses.*

energy gap and has been employed ubiquitously in pump-probe measurements to infer

energy gap evolutions.

The transient change of optical reflectivity measured by the optical

pump-probe method with femtosecond time response reveals that the ultrafast rise of

the reflectivity after excitation of the YBCO is attributed to Cooper pairs breaking, and the subsequence decrease of the reflectivity results from quasiparticle relaxation. Below T_c, the logarithmic plots of $\Delta R/R$ reveal a break in slope near t=2.5 ps. Two relaxation processes [13,14] (fast component τ_1 and slow component τ_2) in our measured data can be clearly observed in YBCO films as shown in the Fig. 4-21. In this case, the two-component fit to the data yields two relaxation times with $\tau_1 \sim 0.7$ ps and $\tau_2 \sim 2.3$ ps at 60 K. Figure 4-20 shows the typical temperature dependence of relaxation times τ_1 and τ_2 for YBCO films obtained by pump-probe measurements. For comparison, we also include the quasiparticle recombination characteristic time obtained from the recovered ΔJ_s curves at various temperature [★ in Fig. 4-20]. The consistency between the two independent measurements is remarkable. It is noted that the fast relaxation process of about 1.0 ps in pump-probe $\Delta R/R$ is also very close to the present ΔJ_s descending time scale.

Finally, we turn our attention to the 70 K result [Fig. 4-13(c)]. The pulse appears to be only slightly modified by kinetic inductance due to drastic suppression of superconducting carriers when $T \rightarrow T_c$. Thus, it is difficult to identify an appropriate transfer process to remove the reshaping effect. Nonetheless, by comparing with the reshaped and recovered pulses at lower temperatures [Figs 4-13(a) and 4-13(b)], the oscillation tail following the main pulse is suggestive of a reshaping effect. The oscillation tails can be significantly suppressed by removing the kinetic inductance effect and may have arisen from the absorption of atmospheric water vapor [87,88].
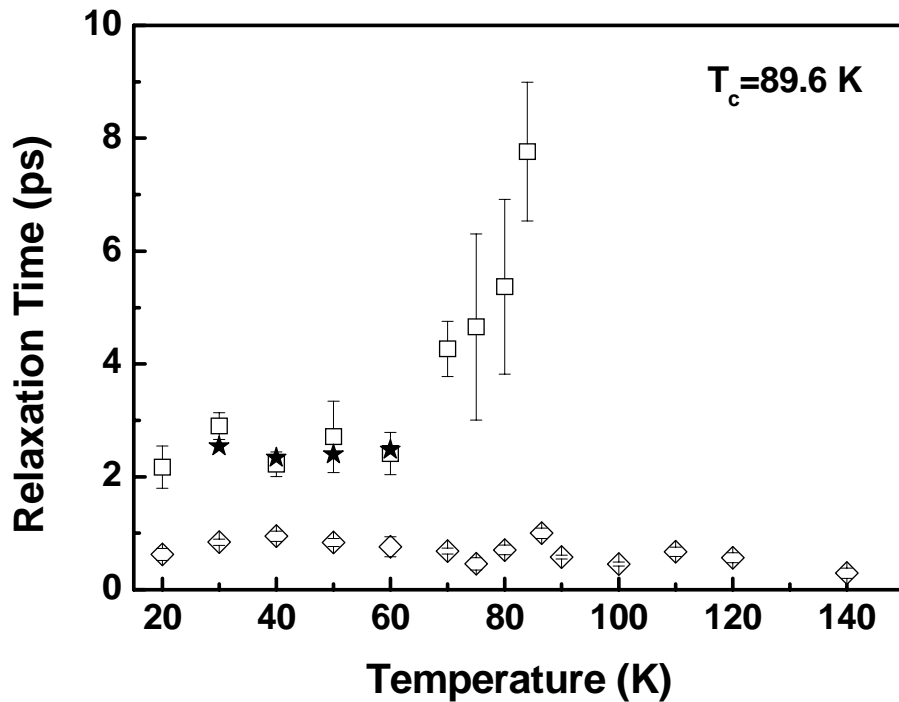
FIG. 4-20. *Temperature-dependent the two relaxation times obtained from optical reflectivity transient measurements in YBCO films. The fast component, τ_1 ($\diamond$) in subpicosecond range appears to be insensitive to temperature, while the slow component, τ_2 ($\square$) diverging near T_c is frequently attributed to gap opening. The characteristic time of quasiparticle recombination calculated from terahertz generation results (30-60 K) denoted by ($\bigstar$) is also included for comparison.*
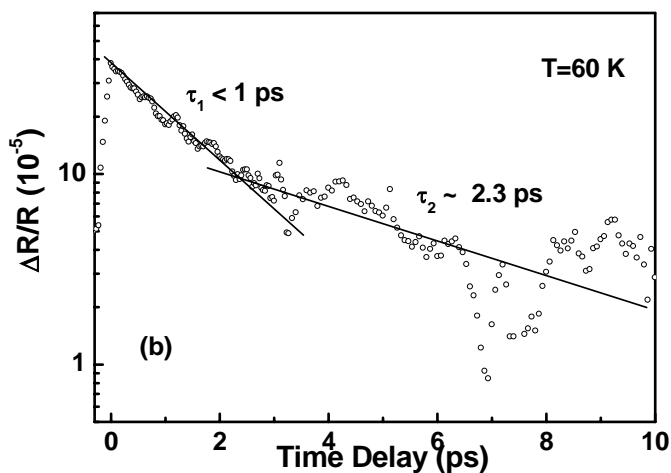
FIG. 4-21. *The typical reflectivity transient $\Delta R / R$ data used to obtain τ_1 and τ_2. The solid line is drawn to indicate the trend.*

4.6 Summary

The origin of photogenerated terahertz radiation pulse emitted from current-biased superconducting $YBa_2Cu_3O_{7-\delta}$ thin films excited by femtosecond optical laser pulses is delineated. The picosecond electromagnetic pulse (450-fs width), generated by the terahertz-field-induced phase retardation of the probe beam converted into an intensity modulation were obtained. The representative frequency spectrum derived by Fourier transform spans over 0.1-4 THz. The dynamics of the emitted terahertz transient related to the nonequilibrium superconductivity is investigated by measuring the dependence of the radiation on excitation power, bias current, and ambient temperature. The effect of the kinetic inductance originated from the superconducting charge carriers is identified to be solely responsible for the pulse reshaping of the original terahertz pulse. After recovering the original waveforms of the emitted terahertz pulses, the transient supercurrent density directly correlated to the optically excited quasiparticle dynamics is obtained. A fast decreasing component of about 1.0 ps and a slower recovery process with a value of 2.5 ps are unambiguously delineated in the optically induced supercurrent modulation. The distorted pulses inevitably result in unphysical time scales, which, in turn, have prevented a direct interpretation relating the supercurrent density transient-induced radiation to quasiparticle dynamics. By including a proper transfer function to remove the effect of kinetic inductance and to recover the original shape of the radiation pulses, we have been able to relate the quasiparticle dynamics associated with nonequilibrium superconductivity to the photogenerated terahertz radiation in a consistent and physically plausible fashion.

Chapter 5

Terahertz Optical Conductivity of Superconducting YBa$_2$Cu$_3$O$_{7-\delta}$ Thin Films

5.1 Principles of the terahertz time-domain spectroscopy

The essential concept of the terahertz time-domain spectroscopy (THz-TDS) can be briefly described as followings: The incident terahertz electric field is polarized parallel to the sample surface. A blank substrate identical to the one supporting the thin film is used as a reference. By doing the fast Fourier transform (FFT) of the temporal response data, we obtain simultaneously both the amplitude and the phase of the field transmitted through the thin-film/substrate composite in the frequency domain [5]. The experimental data usually exhibit a high signal-to-noise ratio; thus data smoothing is unnecessary for analysis. By analyzing the changes in the complex Fourier spectrum introduced by the sample, the spectrum of the index of refraction for the sample is obtained.

If we denote the Fourier transforms of the temporal profiles of the pulse

transmitted through a sample and the reference pulse as $E_f^*(\omega)$ and $E_{ref}^*(\omega)$, respectively, the complex transmittance of the sample can be expressed as:

$$T^*(\omega, n^*(\omega)) = \frac{E_f^*(\omega, n^*(\omega))}{E_{ref}^*(\omega)},$$
Eq. (5-1)

The frequency dependence of the complex index of refraction $n^*(\omega)$ of the sample can then be determined by numerically solving the Eq. (5-1). The temperature- and frequency-dependent complex index of refraction thus obtained are expected to offer the information of both the phase and amplitude of pulsed terahertz generation in HTSC films. Furthermore, the complex optical conductivity can also yield the information for the London penetration depth and the quasiparticle scattering rate with the aid of a two-fluid model.
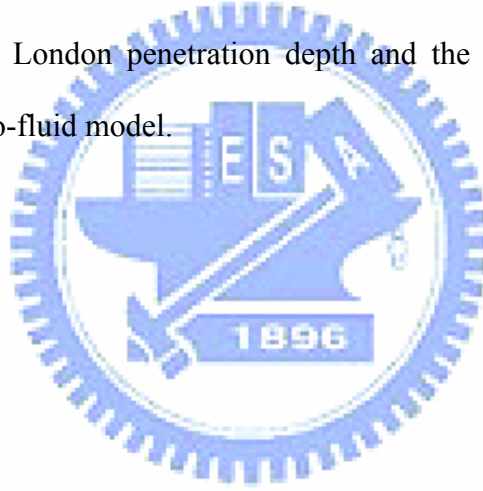
5.2 Theoretical treatment of the complex transmittance

In this section, we will focus on the data processing of the complex transmittance for thin film and substrate separately.

Analysis of substrate complex transmittance:

In this case, the substrate is regarded as the sample signal and air is used as the reference to determine the complex index of refraction of substrate by numerically solving the Eq. (5-1). Figure 5-3(a) schematically illustrates the circumstance of the transmission geometry. Ignoring the multiple reflections inside substrate, the complex transmission coefficient of substrate can be written as

$$t(\omega) = t_s t_s{'}\exp[-i(k_s - k_0)d],$$
$\qquad$ Eq. (5-2)

where d is the thickness of substrate, $t_s = 2n_s/(1+n_s)$ is the transmission coefficient from substrate to air, $t_s{'} = 2/(n_s + 1)$ is the transmission coefficient from air to substrate, k_s the wave number of substrate, k_0 the vacuum wave number, and n_s the complex index of refraction of substrate, respectively. Hence, the complex transmission coefficient can be expressed directly as [89]

$$T*(\omega) = \frac{t(\omega)}{t'(\omega)} = \frac{E^{*}_{substrate}(\omega)}{E^{*}_{air}(\omega)} = \frac{4n_s e^{-i(n_s - 1)\omega d/c}}{(1+n_s)^2},$$
$\qquad$ Eq. (5-3)

where $t'(\omega)$ is the transmission coefficient of vacuum. The experimental terahertz signals of the substrate and vacuum in the frequency domain is denoted as

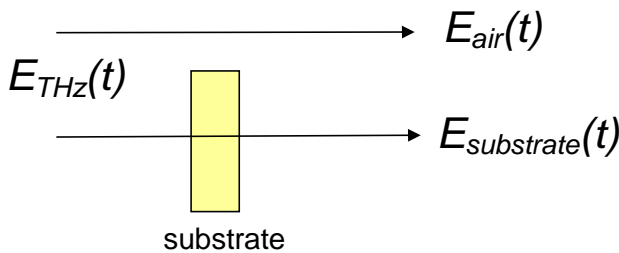FIG. 5-3(a). *Schematic representation of the transmission geometry of the sample. The terahertz temporal profile enters from the left, travels past the substrate or nothing, and exits on the right.*

$E_{THz}(t)$ $E_{air}(t)$ $E_{substrate}(t)$ substrate

$E^*_{substrate}(\omega)$ and $E^*_{air}(\omega)$, respectively. The complex index of refraction of substrate $n^*_s(\omega, T)$ can be determined by minimizing the difference between the experimental data and the theoretical one on the right side of Eq. (5-3) at each frequency.

The case of thin films:

In this case, we regard the sample as a homogeneous dielectric films, and ignore reflections from the rear substrate/air interface, since reflections from this interface are widely separated in time from the leading pulse. Since we are interested only in the leading pulse, the expression for the complex transmission of the air/superconducting film/substrate system at normal incidence [as illustrated in Fig. 5-3(b)] can be written as [90]

$$t(\omega) = \frac{t_{12}t_{23}\exp[in_2(\omega/c)d]}{1 + r_{12}r_{23}\exp[2in_2(\omega/c)d]},$$
<div align="right">Eq. (5-4)</div>

Here, condition $n_2 \gg 1$ is assumed. $t_{ij} = 2n_i/(n_i + n_j)$ is the field transmission coefficient at the ij interface and $r_{ij} = (n_i - n_j)/(n_i + n_j)$ is the field reflection coefficient. In our geometry n_1 represents vacuum, n_2 is the index of the superconducting layer, and n_3 is the index of the substrate, which is to be determined by a separate measurement. Equation (5-4) accounts for multiple
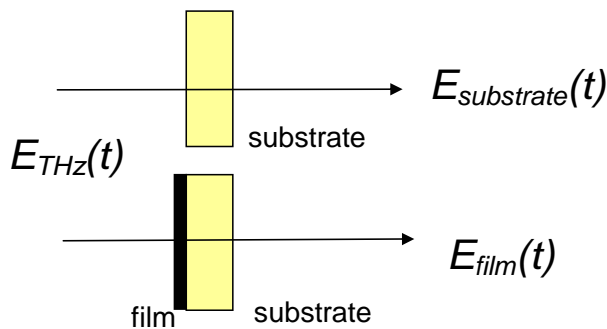
FIG. 5-3(b). *Schematic representation of the transmission geometry of the film. The terahertz temporal profile enters from the left, travels past the substrate or film/substrate, and exits on the right.*

reflections within the superconducting layer but neglects reflections from the back of the substrate.

In addition, the expression of the transmission coefficient of the air/substrate can be written as

$$t'(\omega) = \frac{2n_1}{n_1 + n_3},$$ Eq. (5-5)

Hence, the complex transmittance of the thin film $T*(\omega)$ is obtained by dividing the experimental result of the component of thin film, $E^*_{film}(\omega)$, with that of substrate, $E^*_{substrate}(\omega)$, and can be written as:

$$T*(\omega) = \frac{t(\omega)}{t'(\omega)} = \frac{E^*_{film}(\omega)}{E^*_{substrate}(\omega)} = \frac{2n_2(1+n_3)}{(n_1+n_2)(n_2+n_3)e^{-in_2\omega d/c} + (n_1-n_2)(n_2-n_3)e^{in_2\omega d/c}}$$

Eq. (5-6)

From this one can directly determine the complex refractive index of thin film, $n_2 = n + ik$, by numerically minimizing the difference between the experimental data at each frequency [44].

5.3 Experimental setup

5.3.1 YBa$_2$Cu$_3$O$_{7-\delta}$ thin films preparation

For this study, YBCO thin films were deposited on 0.5-mm-thick NdGaO$_3$ (100) substrates by pulsed laser deposition. The excellent lattice match of NdGaO$_3$ to YBCO is a necessity. The substrate NdGaO$_3$ is specifically chosen because it remains transparent and non-dispersive over the entire spectral bandwidth of the incident pulses, as well as the entire range of temperatures investigated here. Owing to the strong reflection and absorption to the terahertz radiation of the superconducting films itself, the thinner superconducting films is required. In our experiments, the thickness of films about 30 ~ 50 nm is suitable. Thicker films will result in significant degradation in resolution and, hence, blurs the intrinsic characteristics of the sample.

We prepared two YBCO thin films with the same thickness of 30 nm. The critical temperature Tc's, as shown in Fig. 5-1, are 87.8 K (sample A) and 86.6 K (sample B), respectively. In Fig. 5-1, sample A's normal-state resistance of the YBCO film was linear in temperature and extrapolated to 0 Ω near T=0 K. Obviously, the sample A with higher Tc has better quality than sample B which is having higher residual resistance and noticeable deviation of linear temperature dependence in the normal-state resistance. In addition, for both samples, X-ray diffraction shown the presence of sharp (00l) peaks only; no traces of other phases can be detected.
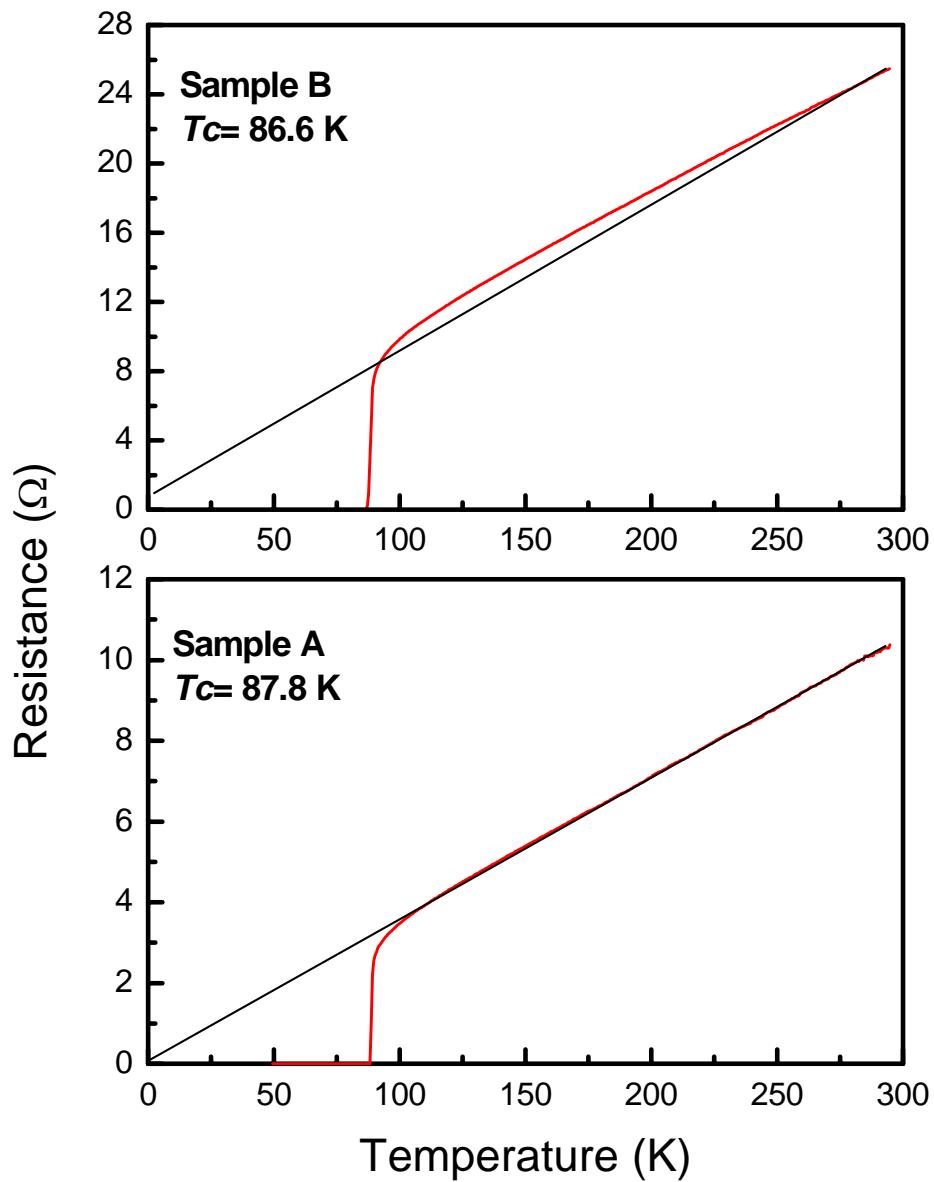
FIG. 5-1. *Temperature-dependent dc resistance of sample A and sample B.*

5.3.2 Optical setup of terahertz time-domain spectroscopy (THz-TDS)

The idea of the established coherent terahertz time-domain spectroscopy technique has been shown in chapter 4 [as shown in Fig. 4-15]. The details of the optical setup of THz-TDS sampling system for measuring the transmission spectra is illustrated in Fig. 5-2. This setup consists of three parts: the pump-probe system, the electro-optic sampling detection, and the cryostat for low temperature measurements. The ultrafast 20-fs optical pulse at 800 nm with a 75-MHz repetition rate is split into pump and probe beams. The pump beam is normally incident on the terahertz emitter to generate terahertz pulses. We use the SI-GaAs photoconductive switch as the terahertz radiation source. The terahertz pulses are collimated and focused on the sample (target) using a pair of off-axis paraboloidal mirrors. The samples are cooled using a Janis flow-through cold-finger cryostat. The terahertz radiation was passed through a 3-mm-thick vacuum window made of Teflon and focused on the sample. After the pulses passed and defocused through the sample and the vacuum window, the terahertz pulse is collimated and re-focused on the terahertz electro-optic sampling detector by using another pair of off-axis paraboloidal mirrors to measure the instantaneous terahertz electric field. The terahertz temporal profile was sampled by scanning the delay between the pump and probe beam. The principle of the electro-optic sampling detection has been described in the previous chapter.
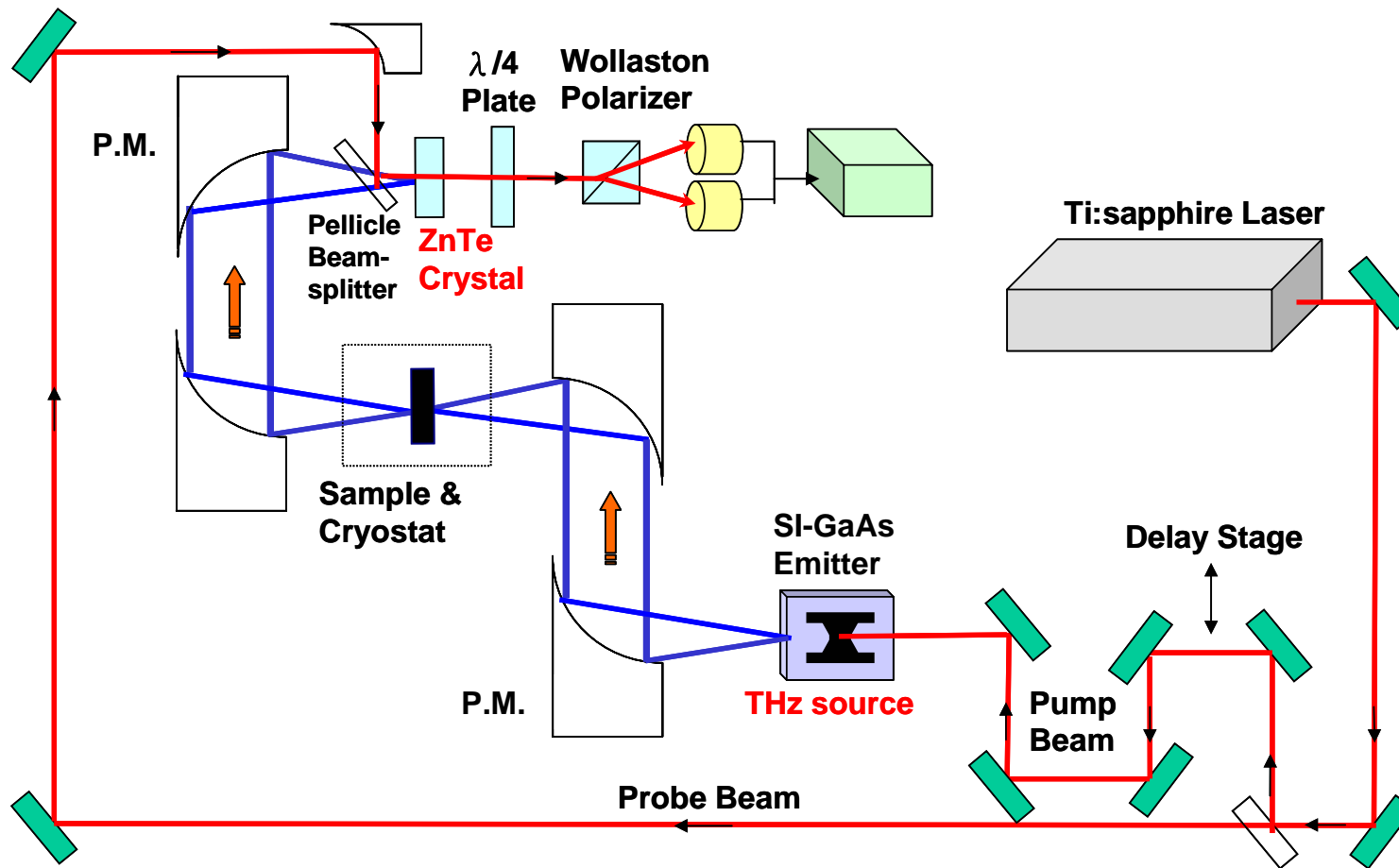
FIG. 5-2. *Illustration the optical setup of the coherent terahertz time-domain spectroscopy system. This setup is constructed from three parts: the pump-probe system、electro-optic sampling detection and the cryostat for low temperature measurements. Details are described in the text.*

5.3.3 Water vapor absorption in terahertz frequency region

The absorption of the terahertz radiation by air has already been mentioned in the previous works (there existed the deep absorption in the frequency spectrum of the terahertz pulses). The THz-TDS can be effectively applied to characterize gases that have significant absorption in terahertz frequency region [40,91]. As shown in Fig. 5-4, it is apparent that there exists sharp absorption of the terahertz radiation by water vapor contained in the laboratory air. Hall *et al.* attributed the deep absorption to H_2O molecule rotation transitions [91,92]. In order to suppress the humidity in the laboratory air, the THz-TDS system is put into a Plexiglas box and purged with dry nitrogen flow [as shown in Fig. 5-6]. Figs 5-4 and 5-5 display the influence of the water vapor absorption on the waveforms and spectra of terahertz pulses. The
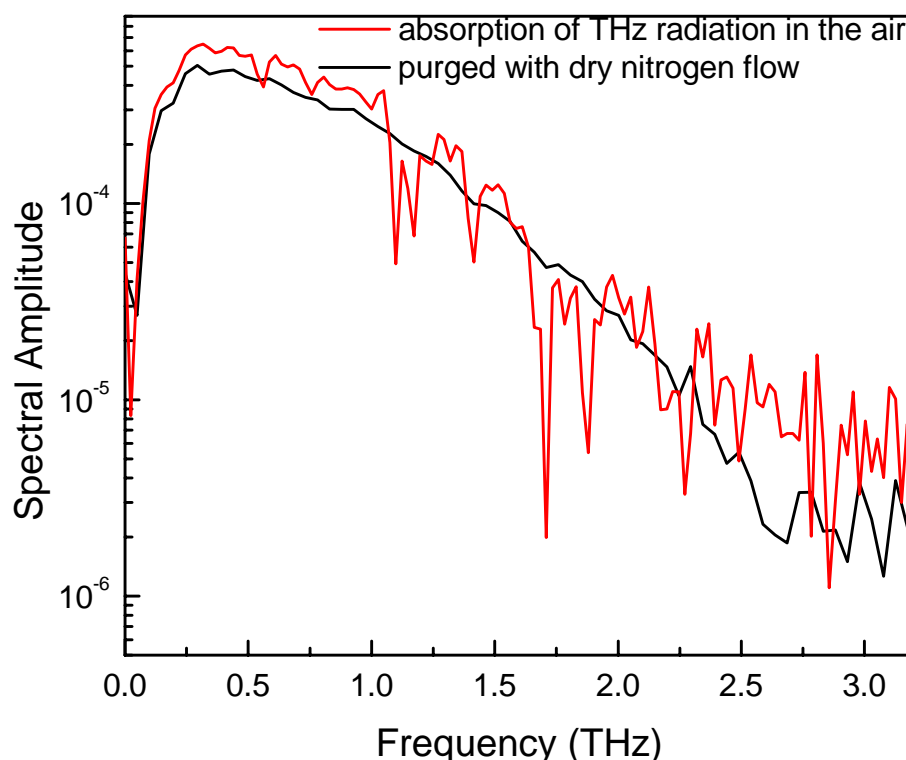

FIG. 5-4. *The absorption of terahertz radiation in the laboratory air compared to the frequency spectrum purged with dry nitrogen flow (dark line). The deep absorption in spectral amplitude is described in the text.*

oscillation tail in the temporal time profile apparently is caused by the water vapor absorption.

In general, the abrupt absorption at several frequencies will result in large errors in the estimation of sample's intrinsic characteristics. It is essential that the influence of water vapor is minimized in order to obtain more precise information using the THz-TDS system. Table 5.1 shows the measured frequencies and wave numbers of the absorption lines compared to the results reported by Hall *et al.* [92]. The corresponding absorption lines located at 0.56 THz、0.76 THz、1.1 THz、1.4 THz and 1.7 THz are in good agreement with our data.
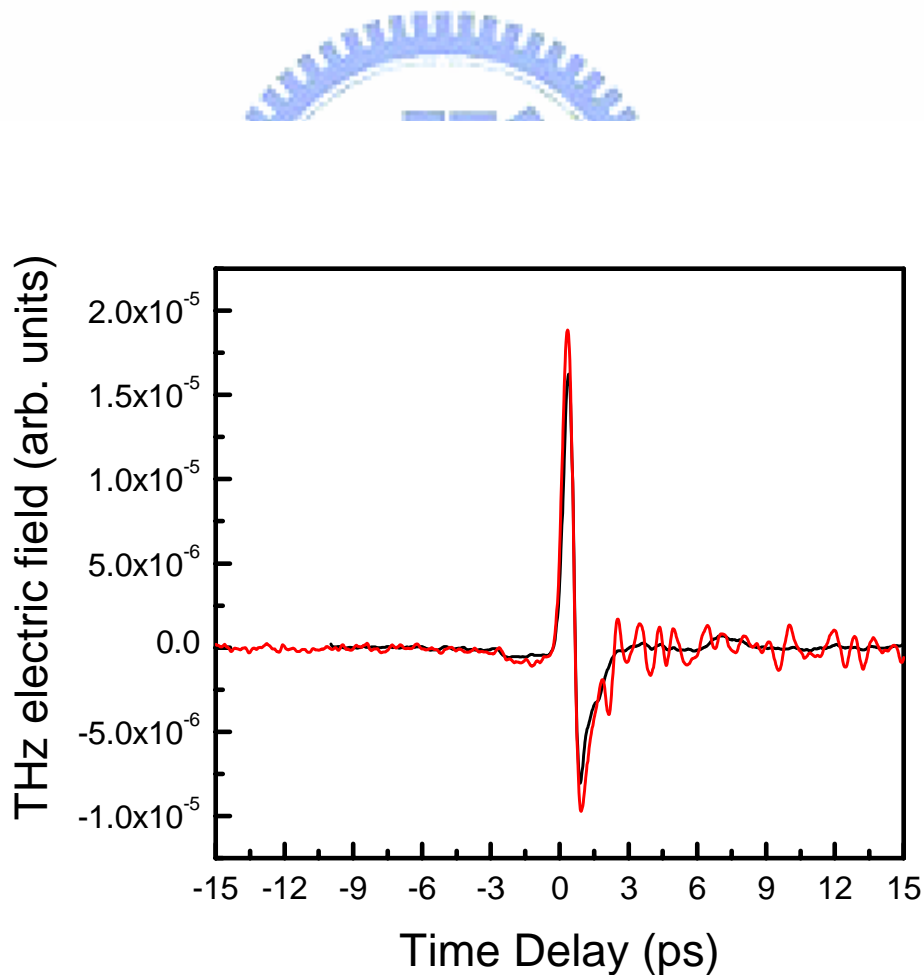
FIG. 5-5. *Illustration the influence of the water vapor absorption on the waveform of terahertz temporal profile (red line). After purged with dry nitrogen flow, the time profile displays no oscillation tail on the waveform (dark line).*
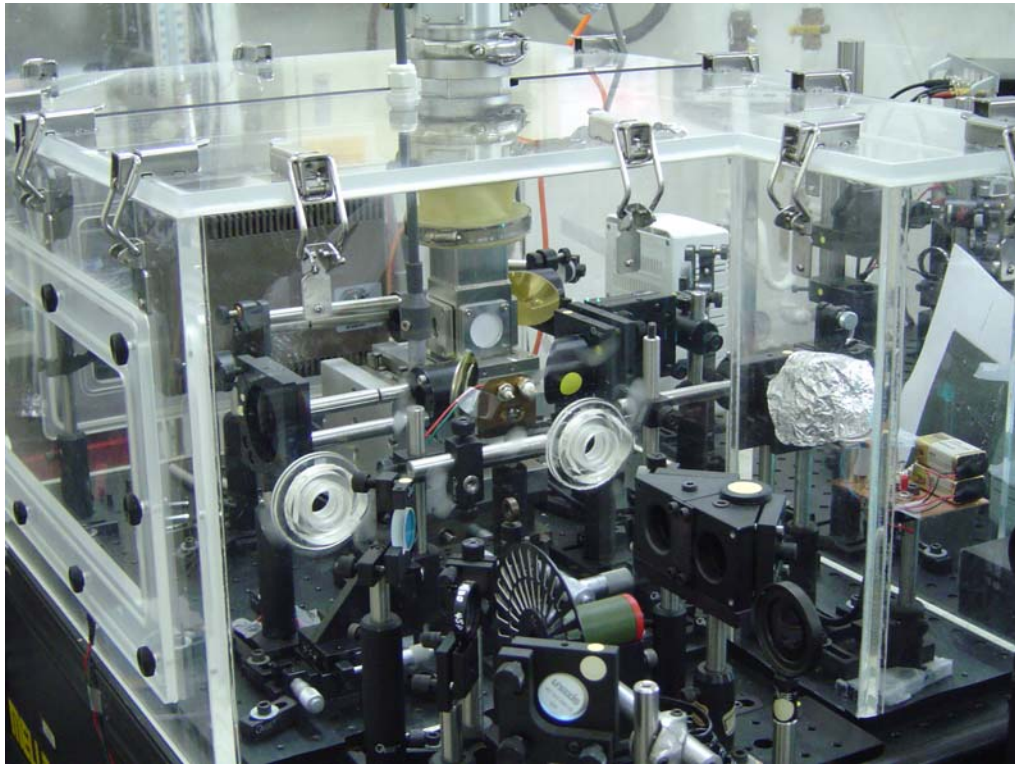
FIG. 5-6 *Display the experimental setup of terahertz time-domain spectroscopy in our laboratory. The system is put into a Plexiglas box and purged with dry nitrogen flow to suppress the humidity in the laboratory air.*

Table 5.1 Water vapor absorption lines in the terahertz range

Line #	1	2	3	4	5
f [THz] measured	0.56	0.76	1.10	1.17	1.42
f [cm^{-1}] measured	18.6	25.3	36.6	39	47.3
f [cm^{-1}] Hall *et al.* [92]	18.58	25.09	36.59	40.36	48.33

Line #	6	7	8	9	10
f [THz] measured	1.71	1.78	1.88	2.17	2.27
f [cm^{-1}] measured	57	59.3	62.6	72.3	75.6
f [cm^{-1}] Hall *et al.* [92]	57.29	59.68	62.24	72.2	75.52

5.3.4 Index of refraction of NdGaO$_3$ substrate in terahertz region

This section presents the THz-TDS measurements of the dielectric substrate NdGaO$_3$. Employing the method discussed previously, one can take the sample's signal (substrate) and the reference signal (air) to determine the index of refraction of the sample quite accurately. In the case of a homogeneous sample the complex refraction index of substrate $n_s* = n + ik$ can be then converted to complex dielectric function $\varepsilon* = \varepsilon_r + i\varepsilon_i$ using the relation $n_s* = \sqrt{\varepsilon*}$.

Figure 5-7 demonstrates the time-domain spectra for radiations through vacuum and NdGaO$_3$ substrate, respectively. The NdGaO$_3$ substrate causes a time delay relative to vacuum by $\Delta t = (n_s - 1)d/c$. Where d is substrate's thickness and c is the speed of light. The minor secondary signal appearing after about 15 ps delay of
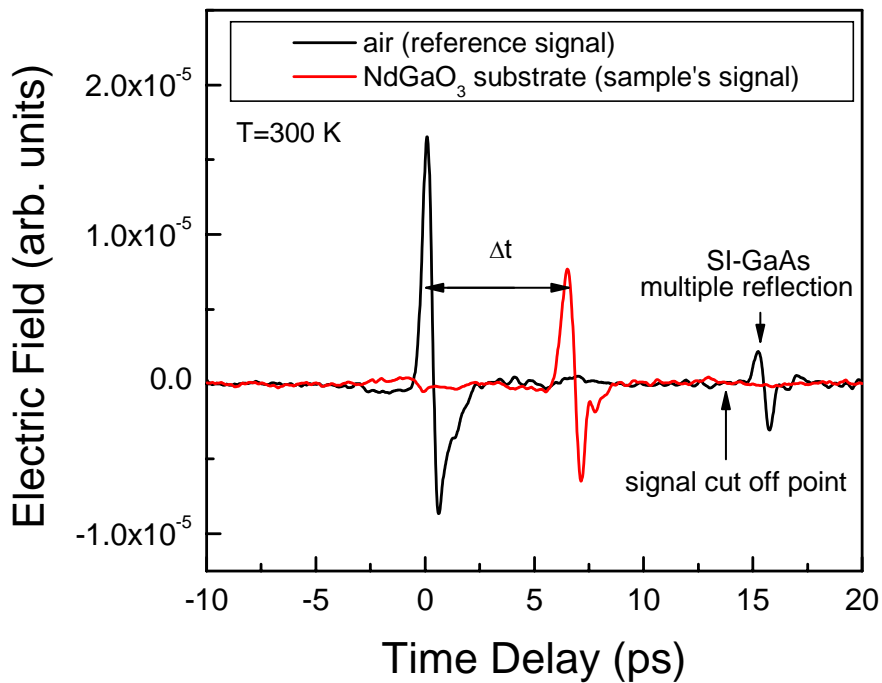

FIG. 5-7. *Demonstration the terahertz time-domain spectra obtained for radiation through vacuum and with NdGaO$_3$ substrate (red line).*

the main terahertz pulse is believed to arise from the substrate (SI-GaAs) multiple reflections. After Fourier transforming the pulse with longer time scanning (terahertz signals including the part of multiple reflection), the effect of the multiple reflection in the GaAs, as shown in the Fig. 5-8(a), is seen in the spectrum. The periodic oscillation hinders the data processing in obtaining the material's intrinsic characteristics. Hence, by losing some resolution, we choose a time scanning range which avoids the effect of the multiple reflection in the terahertz temporal profile. In Fig. 5-7, we collect the sampling range of time delay between -10 ps to 14 ps (Fig. 5-8(a) shown the Fourier transforms without the effect of multiple reflection). Then, according to Eq. (5-1) and by numerically solving Eq. (5-2), the amplitude of transmittance and the index of refraction of NdGaO$_3$ substrate are plotted as a function of frequency. In Fig. 5-8(b), where we plot transmission data taken on a bare 0.5-mm NdGaO$_3$ substrate at 300 K. The real part of the index of refraction n_s as a function of frequency is plotted in Fig. 5-9. The imaginary part, being nearly zero at all frequencies, is also plotted in Fig. 5-9. At 60 K, n varies slightly from 4.62 for low frequencies up to 4.7 for higher frequencies. The frequency dependence of the index of refraction remains approximately the same with temperature, displaying the linear dispersion. The value of index of refraction of substrate, for example at 0.5 THz, will vary with temperature from 4.65 at 60 K to 4.75 at 276 K. This variation must be taken into account in the data processing. Figure 5-10 shows the complex dielectric function as a function of frequencies for NdGaO$_3$ substrate. In this case, $k\sim0$ leads to $\varepsilon_i\sim0$ and $\varepsilon_r\sim n^2$ over the whole range of frequencies and temperatures. Similarly, the frequency dependence of the real part of the dielectric function remains approximately the same over the entire temperature range studied. The value ε_r varies from 21.5 for low frequencies up to about 22.4 for higher frequencies at 60 K, while changes with temperature from 21.6 [T=60 K] to 22.6 [T=276 K] at 0.5 THz.
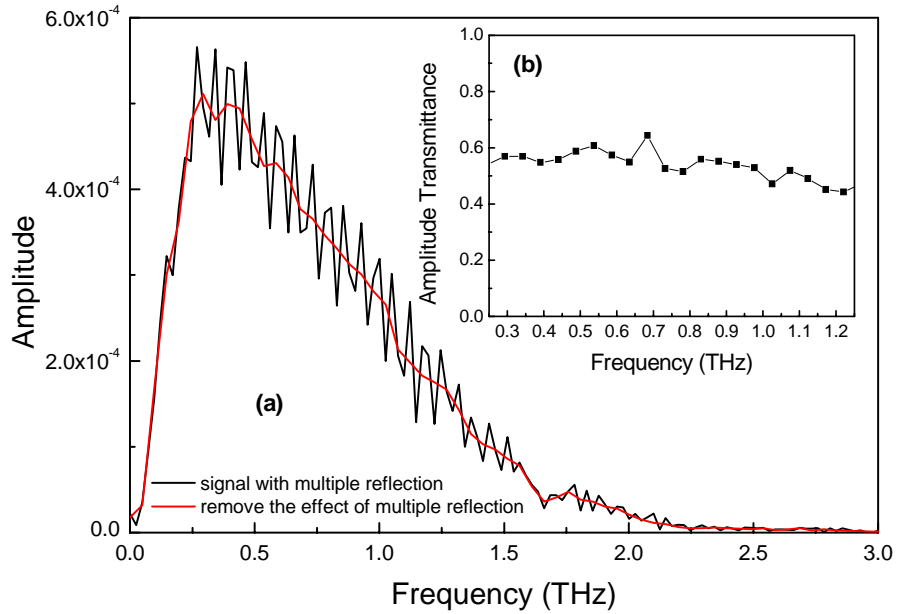
FIG. 5-8. *(a) corresponding frequency spectrum by Fourier transform for radiation through vacuum. The multiple internal reflection of the SI-GaAs substrate is presented in the frequency spectra. The sampling range in time profile is collected (denoted in Fig. 5-7) to avoid the effect of the multiple reflection and shown in the frequency-domain (red line); (b) frequency-dependent transmission spectra of the $NdGaO_3$ substrate at 300 K.*
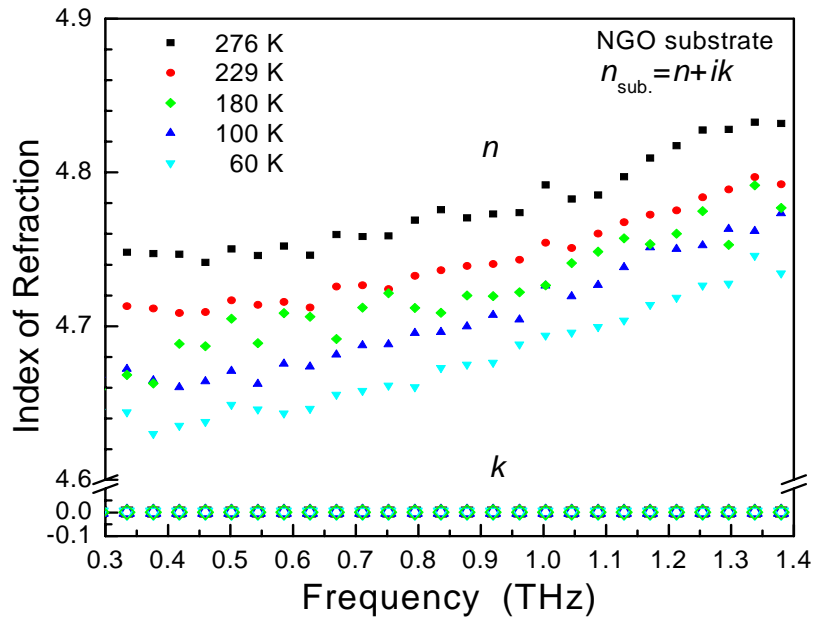
FIG. 5-9. *Calculated index of refraction of NdGaO₃ substrate at various temperatures. .*

FIG. 5-10 *Dielectric function of NdGaO₃ substrate versus frequency at various temperatures.*

5.4 Optical conductivity in superconducting YBa$_2$Cu$_3$O$_{7-\delta}$ thin films

5.4.1 Motivation

The measurements of the low-frequency electrodynamics in high-temperature superconductors has been very important. A detailed review in microwave spectroscopy measurements has been given by Bonn and Hardy [93]. Recently, microstrip ring resonators made of double-side YBCO films were fabricated to investigate the temperature- an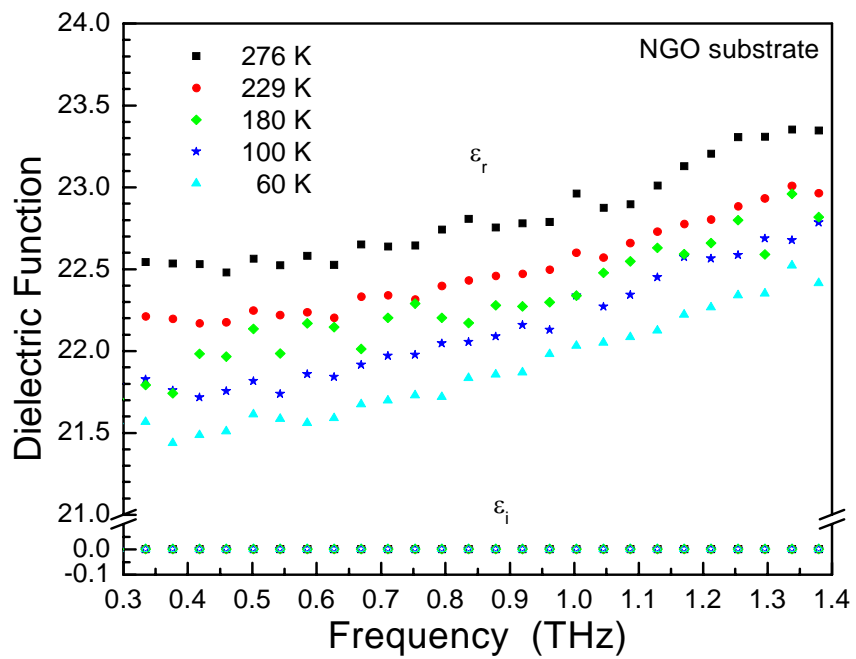d frequency-dependent penetration depth and microwave conductivity and furthermore to enlighten the properties of quasiparticles at microwave frequencies [94]. The optical conductivity $\sigma^*(\omega,T)$ in superconducting thin films at terahertz and submillimeter regime were carried out straight by using the newly developed technique of coherent terahertz time-domain spectroscopy [5,17,18,50,95-102]. However, the temperature dependence of the complex index of refraction $n^*(\omega,T)$ at terahertz frequencies is still not well characterized and it seems important to determine the spectral shape of the terahertz transmission temporal profile in the time-domain. Meanwhile, it seems that similar pulse reshaping phenomena have occurred in transmission spectra between the terahertz generation in FSEOS and the terahertz transmission in THz-TDS measurements by using YBCO thin films as sample. In addition, the method of the THz-TDS can also provide the necessary frequency-dependent information [103]. In particular, we are able to obtain the complex optical conductivity of the YBCO film and use it to directly extract the London penetration depth and the quasiparticle scattering rate with the aid of the two-fluid model.

5.4.2 Electrodynamics and the two-fluid model

Terahertz measurements can be satisfactorily analyzed by using a phenomenological two-fluid model that treats the conductivity of the superconductor as composed of two parts: one that is due to normal carriers whose motion is governed by the Drude equation and one that is due to superconducting carriers whose motion is determined by the London equation. Here, we assume that the carrier response to an applied field is local. The current flow at a point is proportional to the field at the same point satisfied $J = \sigma E$.

In the two-fluid model, each carrier type has its own frequency-dependent conductivity and that the total conductivity is given by the sum of the normal and superconducting part,

$$\sigma(\omega, \text{T}) = \sigma_n(\omega, T) + \sigma_s(\omega, T),$$
Eq. (5-7)

where the subscripts n and s refer to normal and superconducting, respectively. The temperature T sets the relative ratio of the normal to superconducting carrier densities, $n_n(T)$ and $n_s(T)$, respectively.

The normal conductivity is determined by the frequency-dependent Drude expression,

$$\sigma_n(\omega, T) = \frac{n_n e^2 \tau(T) / m^*}{1 - i\omega\tau(T)},$$
Eq. (5-8)

The expression for the frequency-dependent conductivity of the superconducting carriers is given,

$$\sigma_s(\omega, T) = \frac{i}{\mu_o \omega \lambda_L^2(T)},$$
Eq. (5-9)

We note that the conductivity of the superconducting carriers is pure imaginary. One can write the conductivity in terms of the temperature-dependent London penetration depth,

$$\lambda_L(T) = \left[\frac{m^*}{\mu_o n_s(T)e^2}\right]^{1/2}, \qquad \text{Eq. (5-10)}$$

where μ_o is the magnetic permittivity of free space. Physically, λ_L represents the distance that an electromagnetic field may penetrate into a superconductor.

The full expression for the temperature-dependent conductivity, thus, can be written as

$$\sigma(\omega,T) = \frac{n_n e^2 \tau(T)}{m^*(1+\omega^2\tau^2)} - i\left[\frac{n_n e^2 \omega\tau^2}{m^*(1+\omega^2\tau^2)} + \frac{n_s e^2}{m^*\omega}\right], \qquad \text{Eq. (5-11)}$$

where e is the charge of the normal carriers, m^* is their effective mass, and τ is the momentum relaxation time. The real part of the complex conductivity then can be expressed as follow,

$$\sigma_1(\omega,T) = \frac{n_n e^2 \tau(T)}{m^*(1+\omega^2\tau^2)}, \qquad \text{Eq. (5-12)}$$

The quasiparticle scattering rate $1/\tau(T)$ can be calculated directly by using Eq. (5-12) to fit the real part of the conductivity $\sigma_1(\omega,T)$ with frequencies (as called full Drude fit). Besides, the penetration depth $\lambda_L(T)$, based on the circumstance of $\omega^2\tau^2 < 1$, can be extracted from fitting the frequency-dependent imaginary part of complex conductivity and $\lambda_L(0)$ (or the plasma frequency ω_p) is obtained by the extrapolation of σ_2 to T=0 ($\omega_p = c/\lambda_L(0)$).

5.4.3 Terahertz transmission spectra

We have investigated the terahertz temporal profile and the frequency-dependent transmission spectra of the radiation of several YBCO thin films at various temperatures. As discussed in section 5.3.1, the terahertz signals of the sample A with higher film's quality was measured with exposing the THz-TDS system to the air (the humidity is about 42%) and sample B was measured with the system installed in a Plexiglas box and purged with dry nitrogen flow (the humidity is about ~10%).

Figure 5-11 demonstrates the time-domain spectra obtained for radiation through $NdGaO_3$ substrate and YBCO thin film deposited on $NdGaO_3$ substrate. The transmitted electric field of the terahertz pulse is determined by the response of the film and the dielectric properties of the substrate. The transmitted terahertz pulses are almost unchanged in amplitude and phase in whole measured temperature range [as shown in the Fig. 5-11(a)] showing that this substrate can be treated as a ideal material for our purposes. In Fig. 5-11(b), the transmitted terahertz pulses of YBCO thin film in normal state ($T \geq 90$ K) have the same waveform of radiation as like $NdGaO_3$ substrate data, excepting that the transmitted signal is reduced owing to the film's reflection and absorption. In superconducting state, however, besides a further decrease in amplitude, there is a radical change in pulse shape, implying a dramatic phase shift. The pulse reshaping effect can be regarded as a rapid decrease in the real part of the index of refraction of the YBCO films which will be discussed in the next section.

The changes of the transmitted field can be seen more clearly in the frequency-domain transmission by performing a Fourier transform on the time-domain data. The frequency-dependent amplitude transmittance of the YBCO thin film in the normal and superconducting states was shown in the Fig. 5-12. Above

Tc, the transmitted pulse is almost undispersed, as shown by the date taken at 300 K and 90 K, suggesting the metallic behavior (the intrinsic impedance is dominated by the resistance in normal state). The transmission, below *Tc*, abruptly drops implying a dominant response of the imaginary part of the conductivity. The overall transmission level falls with decreasing temperature as the density of superconducting carriers (Cooper pairs) increases. These paired electrons that generates a surface supercurrent and strongly screens the external electromagnetic field.

The time-domain transmission spectra for temperatures ranging from 6 K to 300 K in sample B were shown in Fig. 5-13. The dramatic change of the pulse shape, below *Tc*, can also be found. Figure 5-14 display the corresponding amplitude transmittance as a function of frequency for various temperatures. At room temperature, the frequency response is flat, consistent with metallic conductivity. The amplitude of the transmittance decreases slowly with decreasing temperature until *Tc*. Below *Tc*, there is a distinct drop in the transmission when the samples become superconducting and the Cooper pair density builds up. The noteworthy feature is that the transmission at low frequencies is suppressed more than at high frequencies, suggesting the film acts like a high-pass filter [18].
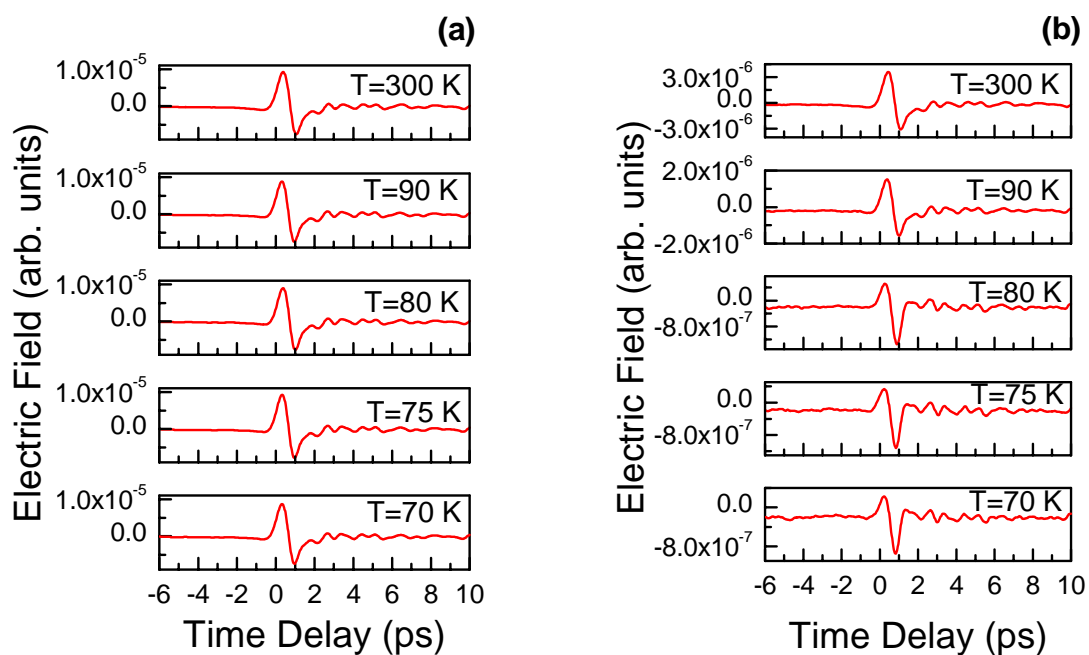
FIG. 5-11 *Transmission time-domain spectra obtained for radiation through (a) NdGaO₃ substrate and (b) YBCO thin film deposited on NdGaO₃ substrate.*

FIG. 5-12 *Frequency-dependent amplitude transmittance of the YBCO thin film (sample A) in the normal and superconducting states.*

FIG. 5-13 *Time-domain transmission spectra for temperatures ranging from 6 K to 300 K in sample B.*
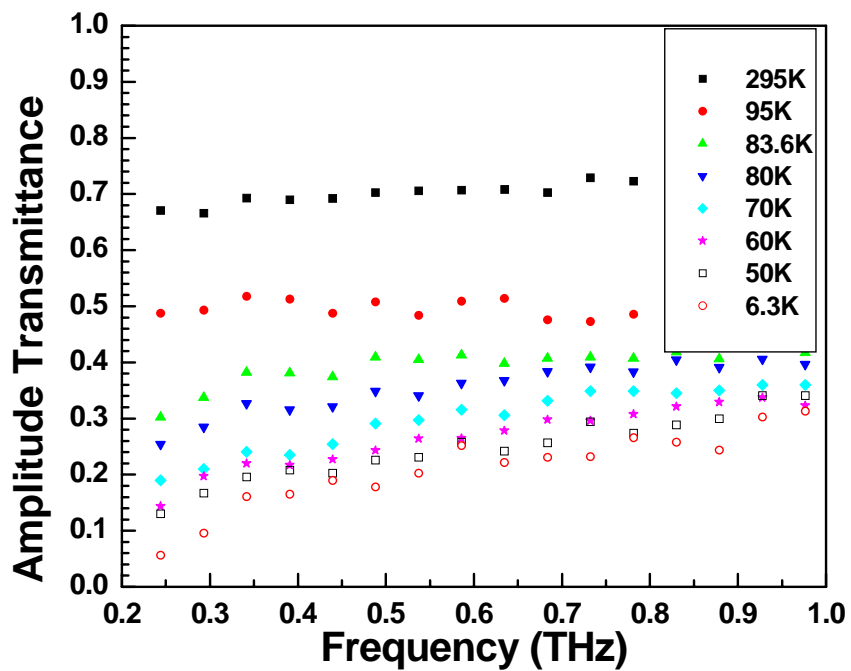
FIG. 5-14 *Corresponding amplitude transmittance as a function of frequency for various temperatures of YBCO thin film.*

5.4.4 The pulse reshaping effect in terahertz temporal profile

In section 5.4.3, we have seen the pulse reshaping effect in sample A, especially the dramatic phase shift in pulse shape. In fact, the pulse reshaping in the measured ter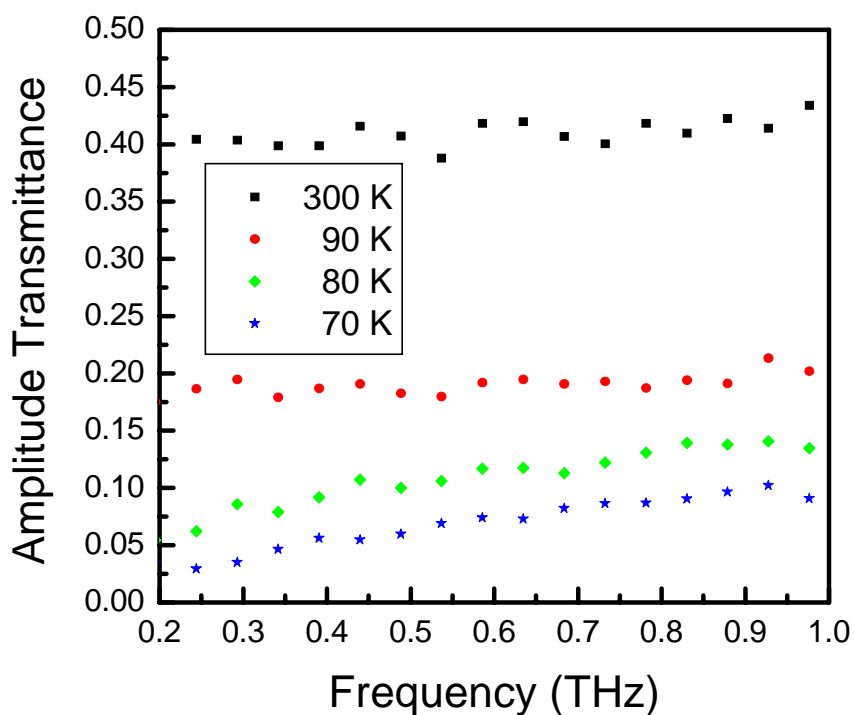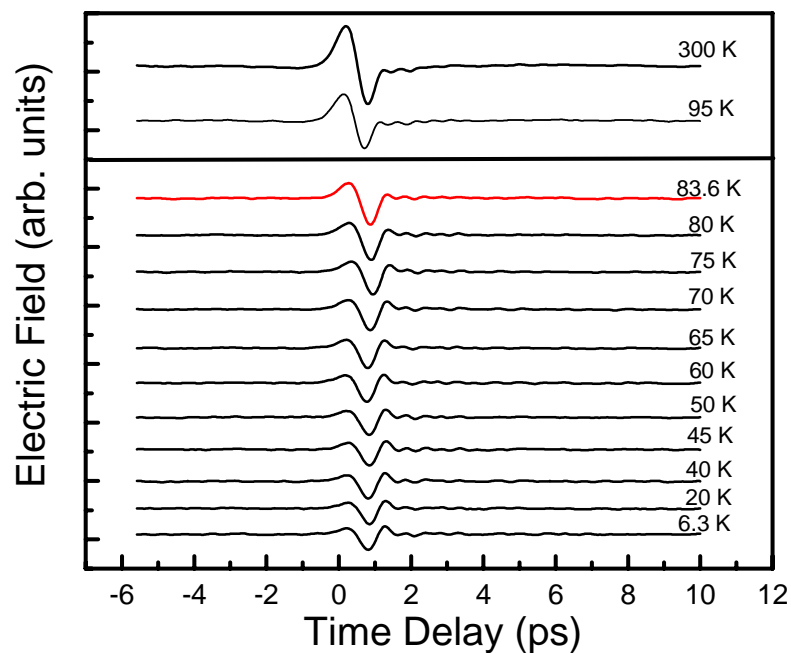ahertz electric field caused by the kinetic inductance of the superconducting charge carriers is identified. The kinetic inductance of charge carriers is neglected since the intrinsic impedance is usually dominated by the resistance. In a superconducting state, however, the kinetic inductance becomes more significance and must be considered as an important parameter. Figure 5-15 illustrated the pulse reshaping results in sample A. Details of the phenomenon of kinetic inductance induced pulse reshaping effect has been reported in Chapter 4, and the duplicate circumstance is present in this section.

FIG. 5-15 *(a) Measured (output) terahertz pulse $E_o(t)$ at 90 K; (b) original terahertz pulse $E_i(t)$ obtained by Eq. (4-7) using the data in (a); (c) measured terahertz pulse at 70 K.*

5.4.5 Optical constant and dielectric function
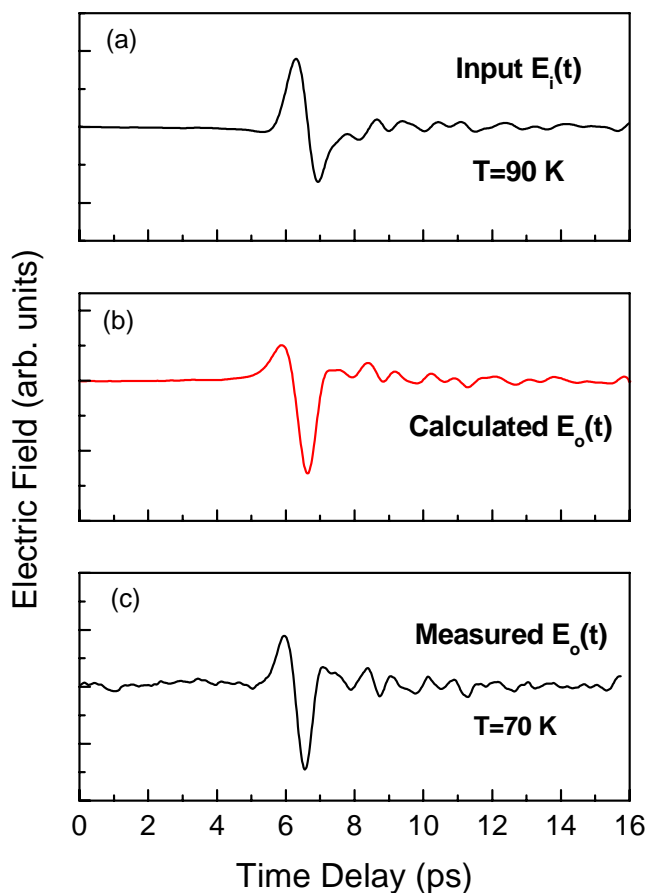
Terahertz time-domain spectroscopy proved a powerful probe for the experimental study of electromagnetic properties of high temperature superconducting thin films at THz-frequencies in basic and applied research. The determination of the index of refraction and dielectric function of superconducting thin films is using the THz-TDS measurements by numerically solving the observed complex transmittance without taking up Kramers-Kronig analysis. In our analysis, the complex index of refraction of the superconducting thin film $n_f* = n + ik$ is determined by numerically minimizing the difference between the experimental data and the theoretical one on the right side of Eq. (5-6) at each frequency [44]. Then the dielectric function $\varepsilon*$ and the optical conductivity $\sigma*$ can be carried out through the relationships

$$n_f^{*2} = \varepsilon* = \varepsilon_1 + i\varepsilon_2, \qquad\qquad \text{Eq. (5-13)}$$

$$\sigma* = \sigma_1 + i\sigma_2 = -i\omega\varepsilon_0\varepsilon*, \qquad\qquad \text{Eq. (5-14)}$$

where $\varepsilon_1 = n^2 - k^2$ and $\varepsilon_2 = 2nk$ represent the real part and imaginary part of the dielectric function, respectively. $\omega = 2\pi f$ is the angular frequency and ε_o is the dielectric function in vacuum space.

The real and imaginary part of the index of refraction of the YBCO thin film (sample B) as a function of temperature at various frequencies is displayed in Fig. 5-16 and Fig. 5-17. With decreasing temperature, the real part of the index of refraction decrease intensively below *Tc* demonstrated the circumstance of the dramatic change in phase shift in terahertz transmission temporal profile in time-domain. Further, it offers a clear manifestation in study the phase shift of the pulses of terahertz radiation that photogenerated from current-biased superconducting YBCO thin films itself mentioned in Fig. 4-11. Besides, in Fig. 5-17, the imaginary

part of the index of refraction strongly arises as cooled down the measured temperature indicating the strong absorption in YBCO thin films itself in terahertz frequencies. We found that the performances regarding to the peak amplitude of terahertz signals rapidly increases with increasing temperature which observed in Figs 4-11 and 5-13. Hence, the variety of the complex index of refraction with temperature and frequency will result in the differences in the output terahertz time-domain spectra. Whatever the investigation of the terahertz transmission in THz-TDS analysis or the terahertz generation in current-biased YBCO films by using the FSEOS detection, determination of complex index of refraction of terahertz broadband of films itself is significant.

According to the Eq. (5-13), one can calculate directly the dielectric function of YBCO thin films. The real part and imaginary part of the dielectric function of the YBCO thin film (sample B) as a function of temperature and frequency is displayed in Fig. 5-18 and Fig. 5-19. An increase in the real part of $\varepsilon*$ from 95 K down to 6.3 K by a factor of about 20 at 0.25 THz is observed, and the imaginary part of $\varepsilon*$ present the large broad peak in whole measured terahertz range. There, the tendency for the peak is to become smaller and to be shifted slightly to higher temperatures for increasing frequency.

FIG. 5-17 *The imaginary part of the index of refraction of the YBCO thin film (sample B) as a function of temperature at various frequencies.*

FIG. 5-16 *The real part of the index of refraction of the YBCO thin film (sample B) as a function of temperature at various frequencies. The solid line is drawn to indicate the trend.*

98

FIG. 5-18 *The real part of the dielectric function of the YBCO thin film (sample B).*
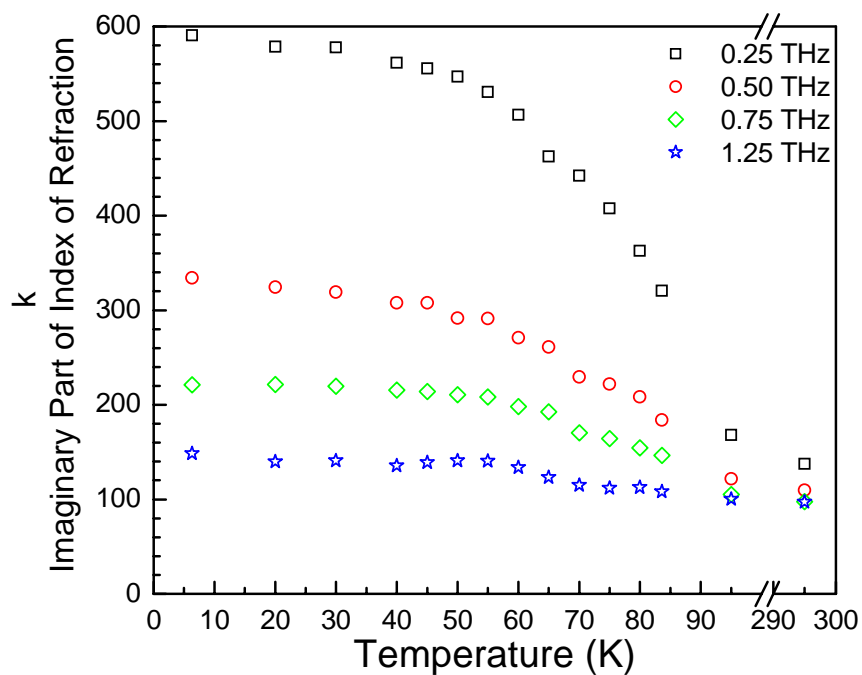

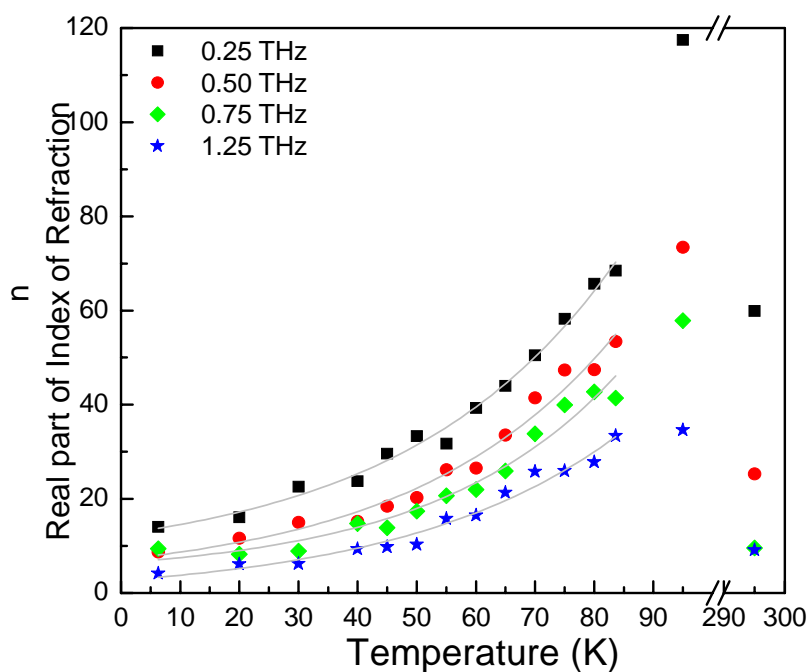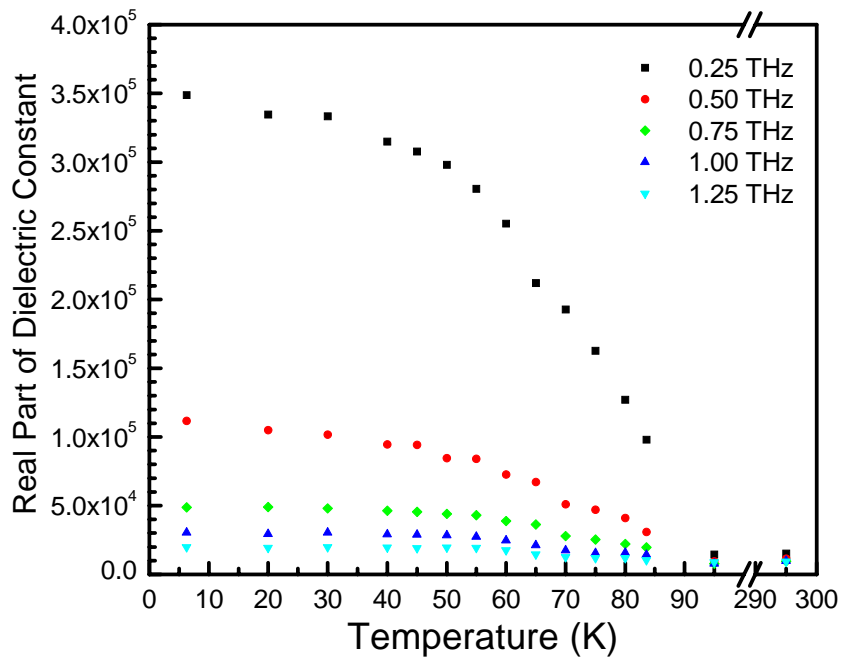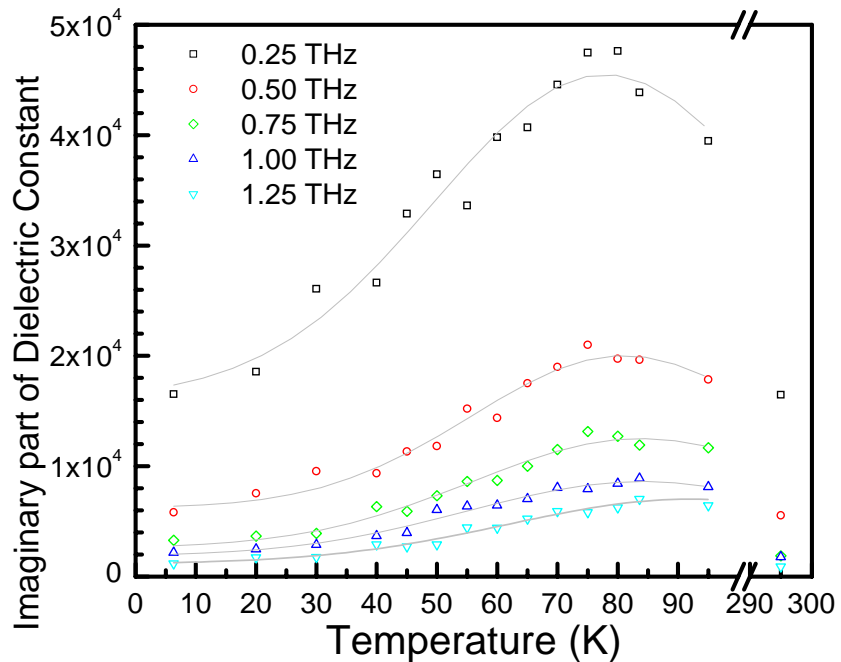FIG. 5-19 *The imaginary part of the dielectric function of the YBCO thin film (sample B) as a function of temperature at various frequencies. The solid line is drawn to indicate the trend.*

5.4.6 Frequency and temperature dependence of complex optical conductivity spectra

Now, based on the expression of the Eq. (5-14), the frequency and temperature dependence of complex optical conductivity can be obtained in sample B. Figs 5-20 and 5-21 display the frequency spectra of the real part and imaginary part of the complex conductivity for different temperatures. The real part of the optical conductivity depends weakly on frequency in normal state as data shown at 300 K and 95 K. However, as the temperature fall down below Tc, a frequency dependence of $\sigma_1(\omega)$ is observed, which becomes more pronounced as the temperature is lowered further. The imaginary conductivity $\sigma_2(\omega)$ below Tc followed $\sim 1/\omega$ dependence [indicated in Eq. (5-9)].

The temperature dependence of the real component of complex conductivity is shown in Fig. 5-22. All results at different frequencies display the similar behavior. There present the large broad peak in whole measured terahertz range, where the peak
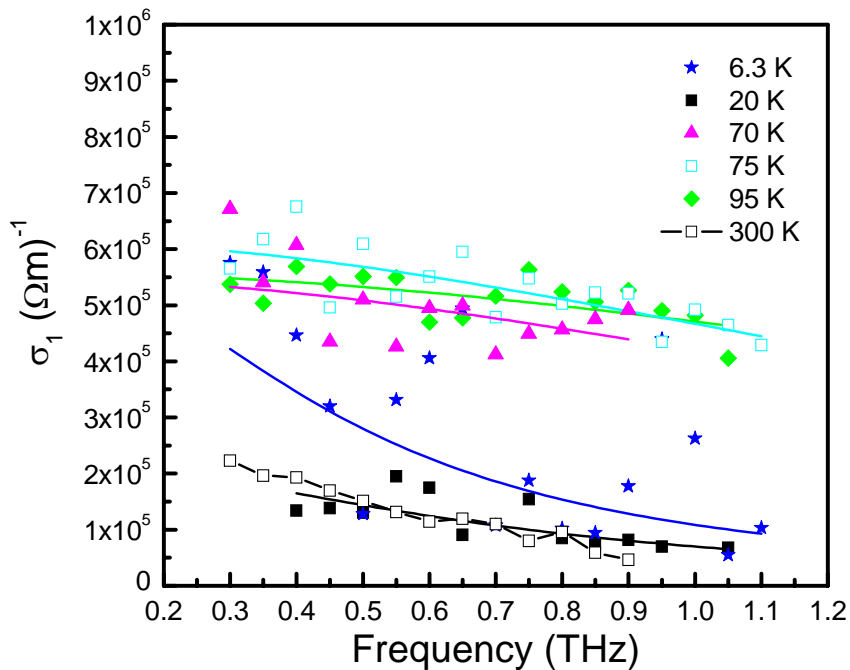
FIG. 5-20 *The frequency spectra of the real part of the complex conductivity for different temperatures.*

is to become smaller and to be shifted slightly to higher temperatures for increasing frequency as described in the imaginary part of dielectric function. The temperature-dependent imaginary conductivity as shown in Fig. 5-23 displayed the sharp rise below Tc and then the whole complex conductivity is dominated by σ_2 at lower temperature measurements, manifesting the electrodynamics in superconductivity (The starting point of the sharp rise will be close to the superconducting transition temperature).

The temperature dependence of $\sigma_1(T)$ is completely determined by the temperature dependence of the number of normal carriers and the scattering rate $1/\tau$ as depicted in the Eq. (5-12). The phenomenon of existence of the broad peak in $\sigma_1(T)$ is already present in microwave range [93,104,105]. The general trend is for the peak to become smaller and move to higher temperature as the frequency is increased. At terahertz frequencies, the same behavior of the peak is observed in our
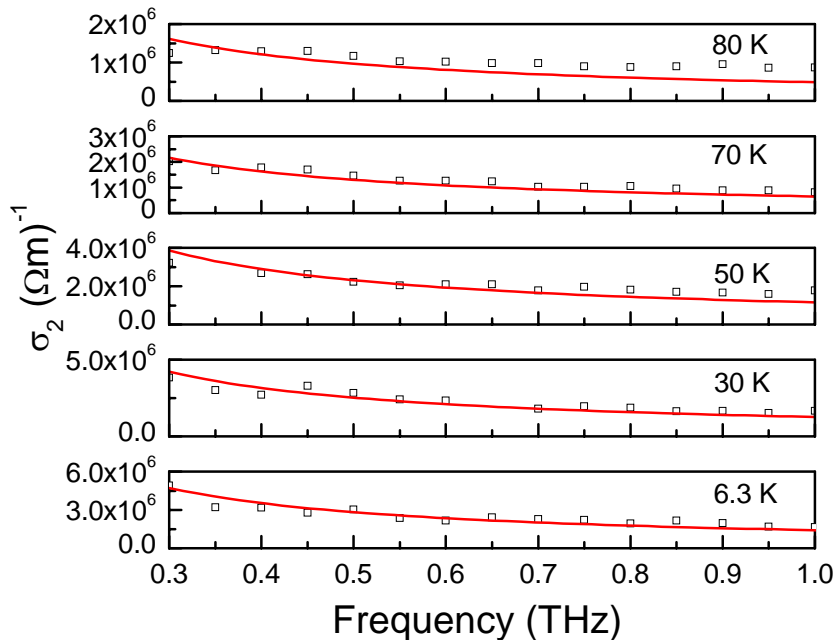

FIG. 5-21 *Frequency spectra of the imaginary part of the complex conductivity for different temperatures.*
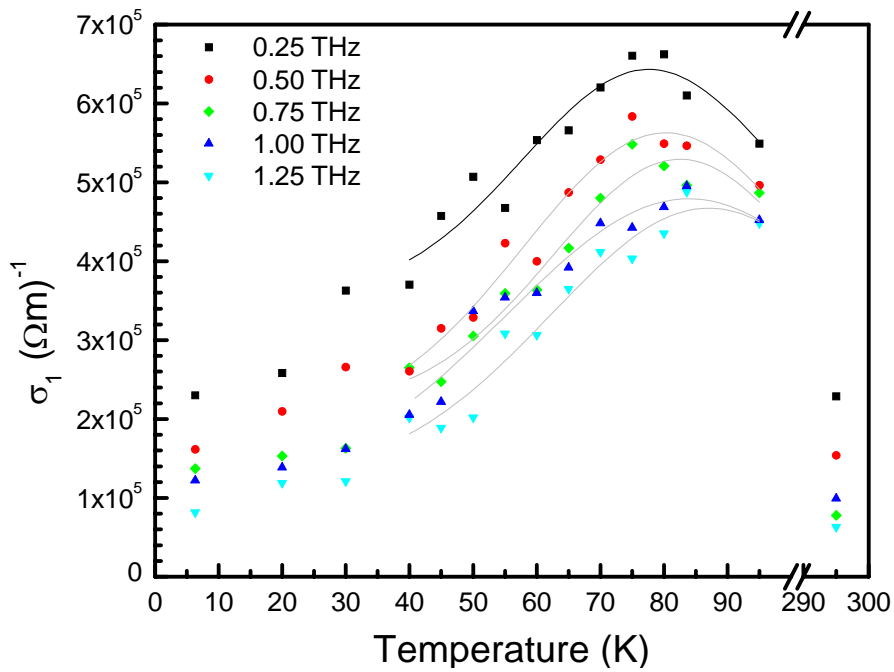
FIG. *5-22 The temperature dependence of the real component of complex conductivity. The solid line is drawn to indicate the trend.*
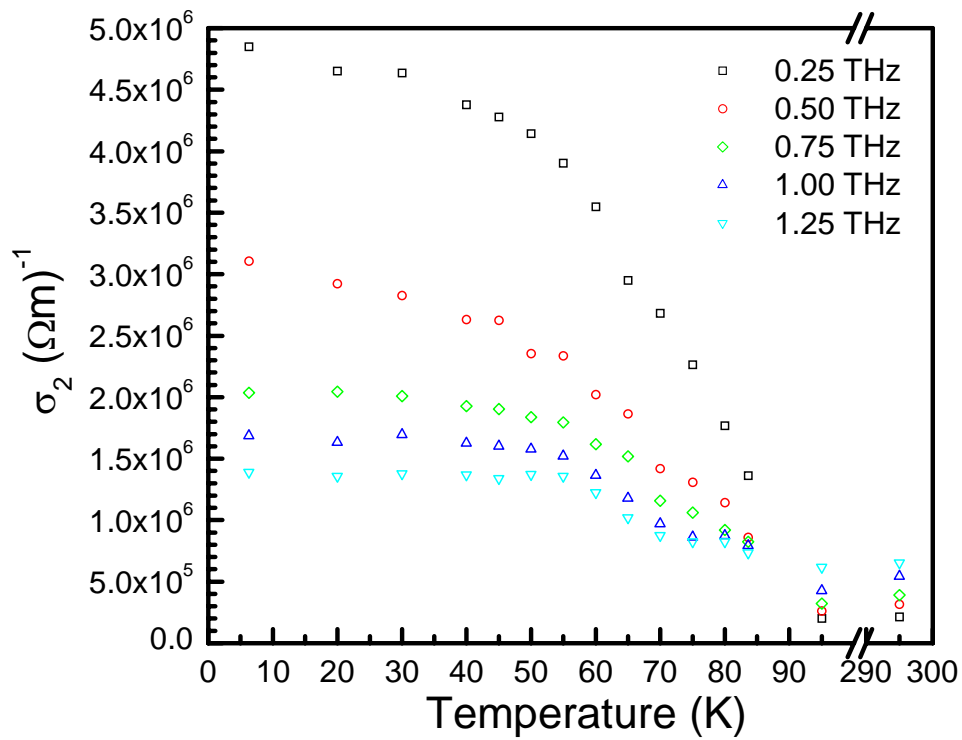
results and other groups [17,67,95,96,106]. Within the two-fluid model used here to extract the normal conductivity, the occurrence of the broad peak is attributed to a competition between an increase in the normal carrier relaxation time and a decrease in the number of normal carriers with decreasing temperature below Tc. The detailed origin of this peak remains a point of intense discussion, although rough arguments have been invoked to explain its existence. Measurements by Nuss *et al*. have revealed a similar peak in $\sigma_1(T)$ at terahertz frequencies that was also explained in terms of a rapidly falling scattering rate below Tc [66]. Those effects of temperature dependence can lead to a peak in the temperature dependence of $\sigma_1(T)$ and, consequently, in ε_2.

In addition, we also reported the imaginary part of the complex conductivity of YBCO thin film in sample A of higher quality varied with the frequency illustrated in Fig. 5-24. Above Tc, the imaginary conductivity is almost frequency independent. In the superconducting state, however, the imaginary conductivity spectra follow an $\sim 1/\omega$ dependence and satisfy the statement of Eq. (5-9). There, however, existed a discrepancy in the results of the imaginary complex conductivity between sample A

FIG. 5-24 *The imaginary part of the complex conductivity in sample A varied with the frequency. Solid lines indicate the fitting results.*

and sample B. We have mentioned that the sample A with higher Tc has great quality than sample B. Therefore, the difference of the absolute value of $\sigma_2(\omega, T)$ in these samples response apparently the characteristic of superconductivity.
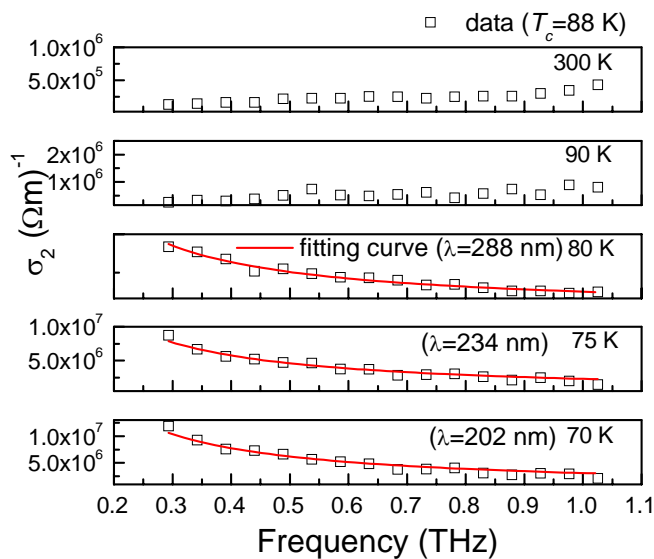
5.4.7 Penetration depth and scattering rate

Coherent terahertz time-domain spectroscopy allows us to investigate the temperature dependence of $\lambda_L(T)$ in an entirely new frequency regime. Further, since we obtain $\sigma(\omega)$ directly from the complex transmission, we obtain λ_L directly from our measurement [see Eq. (5-11)]. The λ_L is obtained from a $1/\omega$ fit to imaginary conductivity. The solid lines in Fig. 5-21 display fits by a $1/\omega$ relation. The London penetration depth as a function of temperature is shown in Fig. 5-15. The experimental determined value for the zero-temperature London penetration depth $\lambda_L(0)$ by extrapolating them to zero temperature in pure YBCO (sample B) is about 295 nm higher than the value typical for high-quality single-crystal samples (145 nm) [93]. But, in our experimental results in sample A, the London penetration depth is about 200 nm at 70 K, indicating the good film quality in our sample.

Figure 5-26 shows the temperature dependence of the scattering rate $1/\tau$ of YBCO films as determined using the simple Drude analysis [Eq. (5-11)] of the complex conductivity. The solid lines in Fig. 5-20 show the full Drude fits of the real part of the complex conductivity. The scattering rate collapses from a value close to 15 THz at Tc to 4.6 THz at 60 K and then remains slightly reduced for further decreasing temperatures. Similar behavior was reported in YBCO both at microwave and terahertz frequencies. Pimenov *et al*. demonstrated the behavior of observed $\sigma'(T)$ by using full Drude fits and clearly observed the plateau [17]. Finally, the effect of the surface defects of these YBCO thin films (sample A and B) may be

104

achieve the significant variation in the London penetration depth and the quasiparticle
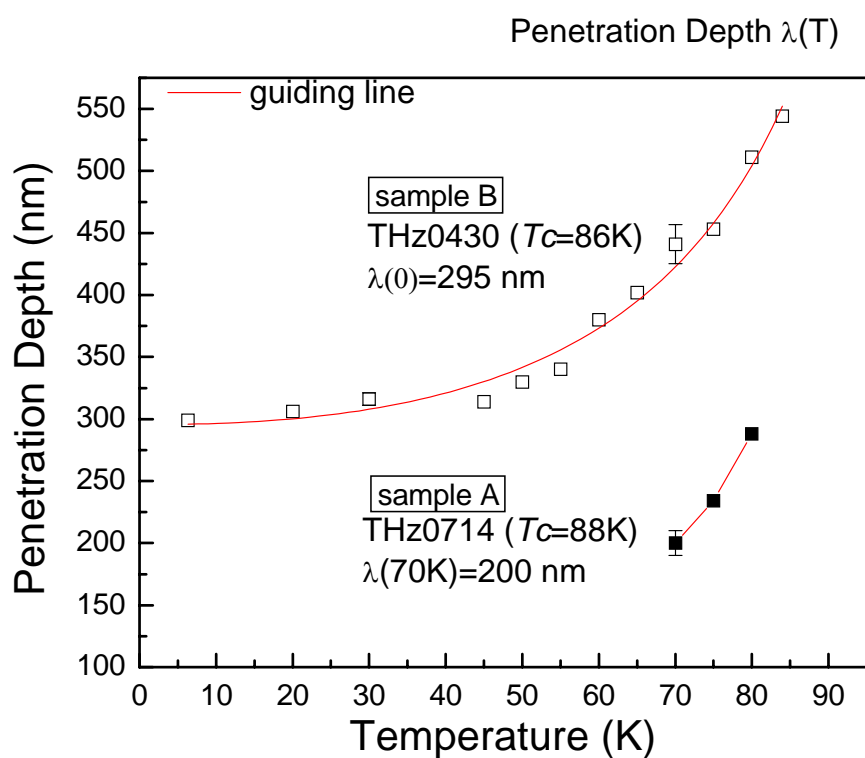
scattering rate as shown in Figs 5-25 and 5-26.

FIG. 5-25 *The London penetration depth as a function of temperature.*
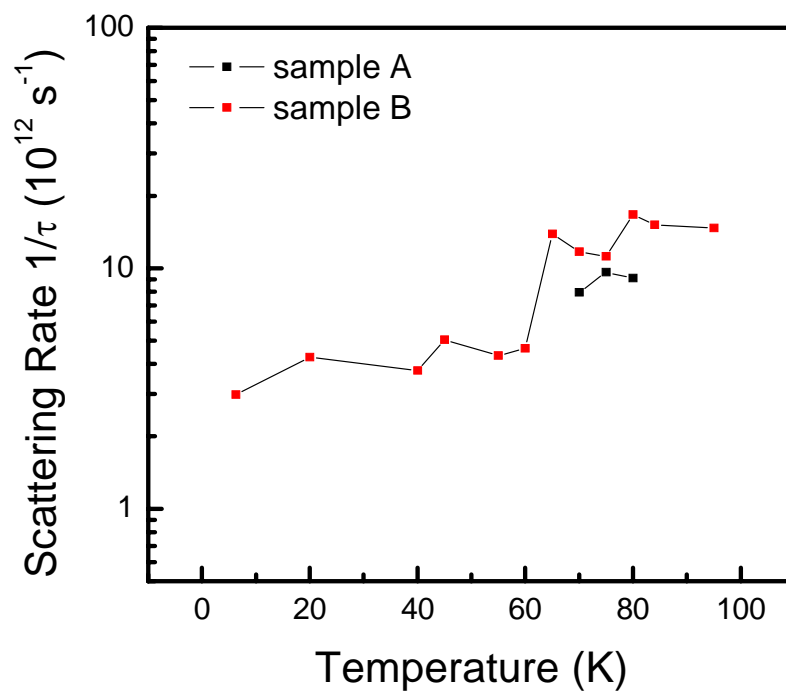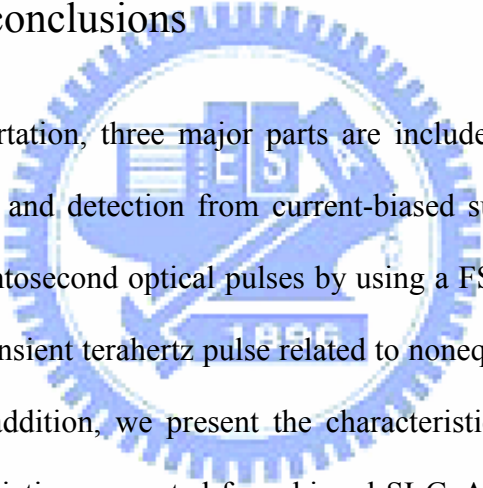
FIG. 5-26 *Temperature dependence of the scattering rate* $1/\tau$ *of YBCO films.*

5.5 Summary

We have used the established coherent terahertz time-domain spectroscopy technique to investigate the properties of the electrodynamics of superconductor at terahertz frequencies. Kinetic inductance-induced pulse reshaping effect was observed directly by measuring the terahertz temporal profile in time transmitted through a pure YBCO thin film which has been understood by using a simple electric circuit analogy in Chapter 4. The temperature- and frequency-dependent complex index of refraction of the materials, such as $NdGaO_3$ substrate and YBCO thin films, had already been determined by analyzing the complex transmittance, and further explained the results in studying the variation of the amplitude and phase of pulse shape of terahertz generation in current-biased YBCO thin film by using a FSEOS technique and in observing the effect of pulse reshaping of terahertz transmission in YBCO thin films by using the THz-TDS measurements. The temperature dependence of the real component of complex conductivity revealed a large broad peak in whole measured terahertz range and believed that it attributed to a competition between an increase in the normal carrier relaxation time and a decrease in the number of normal carriers with decreasing temperature below Tc. By fitting the measured complex optical conductivity $\sigma(\omega,T)$ with the aid of a two-fluid model, we have able to extract the temperature dependence of the London penetration depth, $\lambda_L(T)$ and the temperature dependence of quasiparticle scattering rate $1/\tau(T)$.

Chapter 6

Summary and conclusions

In this dissertation, three major parts are included. The first observation of terahertz generation and detection from current-biased superconducting YBCO thin films excited by femtosecond optical pulses by using a FSEOS technique is reported. The origin of the transient terahertz pulse related to nonequilibrium superconductivity is investigated. In addition, we present the characteristics of the optically induced bipolar terahertz radiation generated from biased SI-GaAs photoconductive switches and detected by using a FSEOS technique. In terahertz applications, we study the terahertz frequency response in YBCO thin films with the THz-TDS measurements.

The characteristics of optically induced bipolar terahertz radiation in biased photoconductive switches were investigated systematically by a free-space electro-optic sampling technique. The observed terahertz temporal profile were bipolar nature and the emitted frequency spectra remained unchanged on varying the optical excitation fluence, strength of the biased field and the emitter gap spacing (ranging from 10-500 μm). The external biased field drives the photogenerated carriers to form a transient photocurrent (an integrated pulse is sampled about 2.0 ps)

across the field region satisfied the expression: $E_{THz} \propto \partial J / \partial t$. These results suggest that the terahertz radiation obtained in the current setup originates from essentially the same mechanism as that associated with the ultrafast charge transport process during pulsed laser illumination.

We have performed measurements and calculations that show how the efficiency of terahertz detection strongly depends on the orientation of the terahertz polarization with respect to the crystal (001) axis and on the angle between the probe beam polarization and the terahertz polarization of the (110)-oriented ZnTe crystal. The terahertz pulse shapes keep unchanged, but the peak intensity of the signal and the polarity will vary with the angle. These results displaying the optimal operating parameters for terahertz pulse detection using the ZnTe crystal.

The origin of photogenerated terahertz radiation pulse emitted from current-biased superconducting $YBa_2Cu_3O_{7-\delta}$ thin films excited by femtosecond optical laser pulses is delineated. The picosecond electromagnetic pulse (450-fs width), generated by the terahertz-field-induced phase retardation of the probe beam converted into an intensity modulation were obtained. The representative frequency spectrum derived by Fourier transform spans over 0.1-4 THz. The dynamics of the emitted terahertz transient related to the nonequilibrium superconductivity is investigated by measuring the dependence of the radiation on excitation power, bias current, and ambient temperature. The effect of the kinetic inductance originated from the superconducting charge carriers is identified to be solely responsible for the pulse reshaping of the original terahertz pulse. After recovering the original waveforms of the emitted terahertz pulses, the transient supercurrent density directly correlated to the optically excited quasiparticle dynamics is obtained. A fast decreasing component of about 1.0 ps and a slower recovery process with a value of 2.5 ps are unambiguously delineated in the optically induced supercurrent modulation. The

distorted pulses inevitably result in unphysical time scales, which, in turn, have prevented a direct interpretation relating the supercurrent density transient-induced radiation to quasiparticle dynamics. By including a proper transfer function to remove the effect of kinetic inductance and to recover the original shape of the radiation pulses, we have been able to relate the quasiparticle dynamics associated with nonequilibrium superconductivity to the photogenerated terahertz radiation in a consistent and physically plausible fashion.

We have used the established coherent THz-TDS technique to investigate the properties of the electrodynamics of superconductor at terahertz frequencies. Kinetic inductance-induced pulse reshaping effect was observed directly by measuring the terahertz temporal profile in time transmitted through a pure YBCO thin film which has been understood by using a simple electric circuit analogy. The temperature- and frequency-dependent complex index of refraction of the materials, such as NdGaO$_3$ substrate and YBCO thin films, had already been determined by analyzing the complex transmittance, and further explained the results in studying the variation of the amplitude and phase of pulse shape of terahertz generation in current-biased YBCO thin film by using a FSEOS technique, and in observing the effect of pulse reshaping of terahertz transmission in YBCO thin films by using the THz-TDS measurements. The temperature dependence of the real component of complex conductivity revealed a large broad peak in whole measured terahertz range and believed that it attributed to a competition between an increase in the normal carrier relaxation time and a decrease in the number of normal carriers with decreasing temperature below Tc. By fitting the measured complex optical conductivity $\sigma(\omega,T)$ with the aid of a two-fluid model, we have able to extract the temperature dependence of the London penetration depth, $\lambda_L(T)$ and the temperature dependence of quasiparticle scattering rate $1/\tau(T)$.

References

[1] B. Ferguson, and X.-C. Zhang, Natural Materials **1**, 26 (2002).

[2] C. Zandonella, Nature, **424**, 721 (2003).

[3] C. A. Schmuttenmaer, Chem. Rev. **104**, 1759 (2004).

[4] D. H. Auston, K. P. Cheung, and P. R. Smith, Appl. Phys. Lett. **45**, 284 (1984).

[5] D. Grischkowsky, S. Keiding, M. V. Exter, and Ch. Fattinger, J. Opt. Soc. Am. B **7**, 2006 (1990).

[6] Q.Wu, M. Litz, and X.-C. Zhang, Appl. Phys. Lett. **68**, 2924 (1996).

[7] C. Winnewisser, P. Uhd Jepsen, M. Schall, V. Schyja, and H. Helm, Appl. Phys. Lett. **70**, 3069 (1997).

[8] C. Jackel, H. G. Roskos, and H. Kurz, Phys. Rev. B **54**, R6889 (1996).

[9] M. Hangyo, S. Tomozawa, Y. Murakami, M. Tonouchi, M. Tani, Z. Wang, K. Sakai, and S. Nakashima, Appl. Phys. Lett. **69**, 2122 (1996).

[10] J.-H. Son, T. B. Norris, and J. F. Whitaker, J. Opt. Soc. Am. B **12**, 2519 (1994).

[11] Y. S. Lai, E. E. Funk, W. L. Gao, C. H. Lee, Z.-Y. Shen, P. Pang, D. J. Dountz, and W. L. Holstein, Appl. Phys. Lett. **65**, 1048 (1994).

[12] M. C. Nuss, P. M. Mankiewich, R. E. Howard, B. L. Straughn, T. E. Harvey, C. D. Brandle, G. W. Berkstresser, K. W. Goossen, and P. R. Smith, Appl. Phys. Lett. **54**, 2265 (1989).

[13] J. Demsar, B. Podobnik, V. V. Kabanov, Th. Wolf, and D. Mihailovic, Phys. Rev. Lett. **82**, 4918 (1999).

[14] C. W. Luo, M. H. Chen, C. C. Chiu, S. P. Chen, K. H. Wu, J.-Y. Lin, J. Y. Juang, T. M. Uen, and Y. S. Gou, J. Low Temp. Phys. **131**, 767 (2003); C. W. Luo, "Anisotropic ultrafast dynamics in $YBa_2Cu_3O_{7-\delta}$ probed by polarized femtosecond spectroscopy", Ph. D. dissertation, National Chiao-Tung University, Hsinchu, Taiwan, R.O.C. (2003).

[15] B. B. Hu, and M. C. Nuss, Opt. Lett. **20**, 1716 (1995).

[16] T. Kiwa, Y. Kamata, M. Misra, H. Murakami, and M. Tonouchi, IEEE Trans. Appl. Supercond. **13**, 3675 (2003).

[17] A. Pimenov, A. Loidl, G. Jakob, and H. Adrian, Phys. Rev. B **59**, 4390 (1999).

[18] S. D. Brorson, R. Buhleier, I. E. Trofimov, J. O. White, Ch. Ludwig, F. F. Balakirev, H.-U. Habermeier, and J. Kuhl, J. Opt. Soc. Am. B **13**, 1979 (1996).

[19] S. G. Han, Z. V. Vardeny, K. S. Wong, O. G. Symko, and G. Koren, Phys. Rev. Lett. **65**, 2708 (1990).

[20] G. L. Eesley, J. Heremans, M. S. Meyer, G. L. Doll, and S.H. Liou, Phys. Rev. Lett. **65**, 3445 (1990).

[21] S. G. Han, Z. V. Vardeny, O. G. Symko, and G. Koren, Phys. Rev. Lett. **67**, 1053 (1991).

[22] G. L. Eesley, J. Heremans, M. S. Meyer, and G. L. Doll, Phys. Rev. Lett. **67**, 1054 (1991).

[23] J. M. Chwalek, C. Uher, J. F. Whitaker, G. A. Mourou, J. Agostinelli, and M. Lelental, Appl. Phys. Lett. **57**, 1696 (1990).

[24] A. Frenkel, Phys. Rev. B **48**, 9717 (1993).

[25] R. A. Kaindl, M. Woerner, T. Elsaesser, D. C. Smith, J. F. Ryan, G. A. Farnam, M. P. McCurry, and D. G. Walmsley, Science **287**, 470 (2000).

[26] C. W. Luo, M. H. Chen, S. P. Chen, K. H. Wu, J. Y. Juang, J.-Y. Lin, T. M. Uen, and Y. S. Gou, Phys. Rev. B **68**, 220508 (2003).

[27] N. Bluzer, Phys. Rev. B **44**, 10222 (1991).

[28] N. Bluzer, J. Appl. Phys. **71**, 1336 (1992).

[29] C. Willams, R. Adam, Q. Xie, R. Sobolewski, and O. Harnack, Supercond. Sci. Technol. **12**, 843 (1999).

[30] F. A. Hegmann, D. J. Perkins, C.-C. Wang, S. H. Moffat, R. A. Hughes, J. S. Preston, M. Currie, P. M. Fauchet, T. Y. Hsiang, and R. Sobolewski, Appl. Phys. Lett. **67**, 285 (1995).

[31] C. J. Stevens, G. Bianchi, and J. F. Ryan, Appl. Phys. Lett. **82**, 4014 (2003).

[32] S. D. Brorson, R. Buhleier, J. O. White, I. E. Trofimov, H.-U. Habermeier, and J. Kuhl, Phys. Rev. B **49**, 6185 (1994).

[33] F. Gao, J. F. Whitaker, Y. Liu, C. Uher, C. E. Platt, and M. V. Klein, Phys. Rev. B **52**, 3607 (1995).

[34] H.-Y. Zhai, M. Paranthaman, and D. H. Lowndes, Phys. Rev. Lett. **88**, 27003 (2002).

[35] M. C. Nuss, K. W. Goossen, P. M. Mankiewich, and M. L. O'Malley, Appl. Phys. Lett. **58**, 2561 (1991).

[36] C. Jaekel, C. Waschke, H. G. Roskos, H. Kurz, W. Prusseit, and H. Kinder, Appl. Phys. Lett. **64**, 3326 (1994).

[37] D. H. Auston, K. P. Cheung, J. A. Valdmanis, and D. A. Kleinman, Phys. Rev. Lett. **53**, 1555 (1984).

[38] Ch. Fattinger, and D. Grischkowsky, Appl. Phys. Lett. **53**, 1480 (1988).

[39] M. V. Exter, and D. Grischkowsky, Phys. Rev. B 41, 12140 (1990).

[40] D. M. Mittleman, R. H. Jakobsen, R. Neelamani, R. G. Baraniuk, and N. C. Nuss, Appl. Phys. B **67**, 379 (1998).

[41] L. Duvillaret, F. Garet, and J.-L. Coutaz, Appl. Opt. **38**, 409 (1999).

[42] P. Kuzel, and J. Petzelt, Ferroelectrics **239**, 949 (2000).

[43] N. Kida, M. Hangyo, and M. Tonouchi, Phy. Rev. B **62**, R11965 (2000).

[44] I. Wilke, M. Khazan, C. T. Rieck, P. Kuzel, T. Kaiser, C. Jaekel, and H. Kurz, J. Appl. Phys. **87**, 2984 (2000).

[45] R. D. Averitt, A. I. Lobad, C. Kwon, S. A. Trugman, V. K. Thorsmolle, and A. J. Taylor, Phys. Rev. Lett. **87**, 17401 (2001).

[46] M. Khazan, I. Wilke, and C. Stevens, IEEE Trans. Appl. Supercond. **11**, 3537 (2001).

[47] M. Hangyo, T. Nagashima, and S. Nashima, Meas. Sci. Technol. **13**, 1727 (2002).

[48] R. A. Kaindl, M. A. Carnahan, J. Orenstein, D. S. Chemla, H. M. Christen, H.-Y. Zhai, M. Paranthaman, and D. H. Lowndes, Phys. Rev. Lett. **88**, 27003 (2002).

[49] T. J. Yen, W. J. Padilla, N. Fang, D. C. Vier, D. R. Smith, J. B. Pendry, D. N. Basov, and X. Zhang, Science **303**, 1494 (2004).

[50] I. Francois, C. Jaekel, G. Kyas, D. Dierickx, O. V. der Biest, R. M. Keeres, V. V. Moshchalkov, Y. Bruynseraede, K. G. Roskos, G. Borghs, and H. Kurz, Phys. Rev. B **53**, 12502 (1996).

[51] H. Murakami, T. Kiwa, M. Tonouchi, T. Uchiyama, I. Iguchi, and Z. Wang, Physica C **367**, 322 (2002).

[52] D. Grischkowsky, and S. Keiding, Appl. Phys. Lett. **57**, 1055 (1990).

[53] R. Ramesh, D. Hwang, T. S. Ravi, A. Inam, J. B. Barner, L. Nazar, S. W. Chan, C. Y. Chen, B. Dutta, T. Venkatesan, and X. D. Wu, Appl. Phys. Lett. **56**, 2243 (1990).

[54] H. Y. Zhai, and W. K. Chu, Appl. Phys. Lett. **76**, 3469 (2000).

[55] C. C. Hsu, Master thesis, Department of Electrophysics, National Chiao-Tung University, Hsinchu, Taiwan, R.O.C. (1996).

[56] K. H. Wu, S. P. Chen, J. Y. Junag, T. M .Uen, and Y. S. Gou, Physica C **289**, 230 (1997).

[57] K. H. Wu, M. H. Li, J. Y. Juang, T. M. Uen, Y. S. Gou, and R. T. Kao, Chinese J. Phys. **31**, 1091 (1993).

[58] K. H. Wu, M. C. Hsieh, S. P. Chen, S. C. Chao, J. Y. Juang, T. M. Uen, Y. S. Gou, T. Y. Tseng, C. M. Fu, J. M. Chen, and R. G. Liu, Jpn. J. Appl. Phys. **37**, 4346 (1998).

[59] J. W. Ekin, A. J. Panson, and B. A. Blankenship, Appl. Phys. Lett. **52**, 331 (1988).

[60] J. T. Darrow, X.-C. Zhang, D. H. Auston, and J. D. Morse, IEEE J. Quantum Electron. **28**, 1607 (1992).

[61] P. R. Smith, D. H. Auston, and M. C. Nuss, IEEE J. Quantum Electron. **24**, 255 (1988).

[62] P. U. Jepsen, R. H. Jacobsen, and S. R. Keiding, J. Opt. Soc. Am. B **13**, 2424 (1996).

[63] M. Tani, S. Matsuura, K. Sakai, and S. I. Nakashima, Appl. Opt. **36**, 7853 (1997).

[64] B. B. Hu, E. A. de Souza, W. H. Knox, J. E. Cunningham, M. C. Nuss, A. V. Kuznetsov, and S. L. Chuang, Phys. Rev. Lett. **74**, 1689 (1995).

[65] J. E. Pedersen, V. G. Lyssenko, J. M. Hvam, P. Uhd Jepsen, S. R. Keiding, C. B. Sorensen, and P. E. Lindelof, Appl. Phys. Lett. **62**, 1265 (1993).

[66] M. C. Nuss, P. M. Mankiewich, M. L. O'Malley, E. H. Westerwick, and P. B. Littlewood, Phys. Rev. Lett. **66**, 3305 (1991).

[67] B. Parks, S. Spielman, J. Orenstein, D. T. Nemeth, F. Ludwig, J. Clarke, P. Merchant, and D. J. Lew, Phys. Rev. Lett. **74**, 3265 (1995).

[68] Z. G. Lu, P. Campbell, and X.-C. Zhang, Appl. Phys. Lett. **71**, 593 (1997).

[69] G. Rodriguez, and A. J. Taylor, Opt. Lett. **21**, 1046 (1996).

[70] Y. Cai, I Brener, J. Lopata, J. Wynn, L. Pfeiffer, J. B. Stark, Q. Wu, X.-C. Zhang, and J. F. Federici, Appl. Phys. Lett. **73**, 444 (1998).

[71] S. G. Park, M. R. Melloch, and A. M. Weiner, Appl. Phys. Lett. **73**, 3184 (1998).

[72] Q. Wu, and X.-C. Zhang, Appl. Phys. Lett. **67**, 3523 (1995).

[73] E. Budiarto, N. W. Pu, S. Jeong, and J. Bokor, Opt. Lett. **23**, 213 (1998).

[74] X.-C. Zhang, Y. Jin, D. Ware, X. F. Ma, A. Rice, D. Bliss, J. Larkin, and M. Alexander, Appl. Phys. Lett. **64**, 622 (1994).

[75] P. C. M. Planken, H. K. Nienbuys, H. J. bakker, and T. Wenckebach, J. Opt. Soc. Am. B **18**, 313 (2001),

[76] Q. Chen, M. Tani, Z. Jiang, and X.-C. Zhang, J. Opt. Soc. Am. B **18**, 823 (2001).

[77] A. Yariv, "*Quantum Electronics*", 2nd ed. (Wiley, New York, 1975).

[78] P. I. Lin, S. F. Chen, K. H. Wu, J. Y. Juang, T. M. Uen, and Y. S. Gou, Jpn. J. Appl. Phys. **41**, L1158 (2002).

[79] P. I. Lin, K. H. Wu, J. Y. Juang, J.-Y. Lin, T. M. Uen, and Y. S. Gou, IEEE Trans.

Appl. Supercond. **13**, 20 (2003).

[80] M. Hangyo, S. Tomozawa, Y. Murakami, M. Tonouchi, M. Tani, Z. Wang, and K. Sakai, IEEE Tran. Appl. Supercond. **7**, 2909 (1997).

[81] S. Shikii, T. Kondo, M. Yamashita, M. Tonouchi, M. Hangyo, M. Tani, and K. Sakai, Appl. Phys. Lett. **74**, 1317 (1999).

[82] M. Tonouchi, M. Tani, Z. Wang, K. Sakai, S. Tomozawa, M. Hagyo, Y. Murakami, and S. I. Nakashima, Jpn, J. Appl. Phys. **35**, 2624 (1996).

[83] M. Tani, M. Tonouchi, M. Hangyo, Z. Wang, N. Onodera and K. Sakai, Jpn. J. Appl. Phys. **36**, 1984 (1997).

[84] C. Williams, Y. Xu, R. Adam, M. Darula, O. Harnack, J. Scherbel, M. Siegel, F. A. Hegmann, and R. Sobolewski, IEEE Trans. Appl. Supercond. **11**, 578 (2001).

[85] F. A. Hegmann, and J. S. Preston, Phys. Rev. B **48**, 16023 (1993).

[86] A. V. Sergeev and M. Y. Reizer, Int. J. Mod. Phys. **10**, 635 (1996).

[87] M. V. Exter, Ch. Fattinger, and D. Grischkowsky, Opt. Lett. **14**, 1128 (1989).

[88] R. A. Cheville, and D. Grischkowsky, Opt. Lett. **20**, 1646 (1995).

[89] Maxim A. Khazan, "Time-domain terahertz spectroscopy and its application to the study of high-*Tc* superconductor thin films", Ph. D. dissertation, Hamburg University, Hamburg, Germany (2002).

[90] M. Born, and E. Wolf, "*Principle of Optics*" (MacMillan, New York, 1964).

[91] R. A. Cheville, and, D. Grischkowsky, J. Opt. Soc. Am. B **16**, 317 (1999).

[92] R. T. Hall, D. Vrabec, and J. M. Dowling, Appl. Opt. **5**, 1147 (1966).

[93] D. A. Bonn, R. Liang, T. M. Riseman, D. J. Baar, D. C. Brewer, K. Zhang, P. Dosanjh, T. L. Duty, A. MacFarlane, G. D. Morris, J. H. Brewer, W. N. Hardy, C. Kallin, and A. J. Berlinsky, Phys. Rev. B **47**, 11314 (1993).

[94] L. H. Lai, H. K. Zheng, J. Y. Juang, K. H. Wu, T. M. Uen, J.-Y. Lin, and Y. S. Gou, to be published (2004).

[95] A. Frenkel, F. Gao, Y. Liu, J. F. Whitaker, C. Uher, S. Y. Hou, and J. M. Phillips, Phys. Rev. B **54**, 1355 (1996).

[96] C. Ludwig, Q. Jiang, J. Kuhl, and J. Zegenhagen, Physica C **269**, 249 (1996).

[97] R. D. Averitt, G. Rodriguez, J. L. W. Siders, S. A. Trugman, and A. J. Taylor, J. Opt. Soc. Am. B **17**, 327 (2000).

[98] A. V. Pronin, A. Pimenov, A. Loidl, and S. I. Krasnosvobodtsev, Phys. Rev. Lett. **87**, 97003 (2001).

[99] E. Knoesel, M. Bonn, J. Shan, and T. F. Heinz, Phys. Rev. Lett. **86**, 340 (2001).

[100] J. Demsar, R. D. Averitt, A. J. Taylor, V. V. Kabanov, W. N. Kang, H. J. Kim, E. M. Choi, and S. I. Lee, Phys. Rev. Lett. **91**, 267002 (2003).

[101] T. Kiwa, and M. Tonouchi, Physica C **362**, 314 (2001).

[102] T.-R. Tasi, C.-C. Chi, and S. F. Horng, Physica C **391**, 281 (2003).

[103] V. K. Thorsmolle, R. D. Averitt, M. P. Maley, L. N. Bulaevikii, C. Helm, and A. J. Taylor, Opt. Lett. **26**, 1292 (2001).

[104] A. Hosseini, R. Harris, S. Kamal, P. Dosanjh, J. Preston, R. Liang, W. N. Hardy, and D. A. Born, Phys. Rev. B **60**, 1349 (1999).

[105] S. Hensen, G. Muller, C. T. Rieck, and K. Scharnberg, Phys. Rev. **56**, 6237 (1997).

[106] F. Gao, G. L. Carr, C. D. Porter, D. B. Tanner, G. P. Williams, C. J. Hirschmugl, B. Dutta, X. D. Wu, and S. Etemad, Phys. Rev. B **54**, 700 (1996).

Biographical Notes

Personal Data ：

     Name   ： 林 博 瑛 （ Lin, Po-Iem ）

     Sex   ： Male

     Data of Birth   ： June 19, 1972

     E-mail   ： glinpi.ep87g@nctu.edu.tw

Education ：

   1992/09~1996/06   National Sun Yat-Sen University, Kaohsiung, Taiwan
                         BS. degree in Physics.

   1996/09~1998/06   National Sun Yat-Sen University, Kaohsiung, Taiwan
                         MS. degree in Physics.

   1998/09~2004/10   National Chiao Tung University, Hsinchu, Taiwan
                         Ph. D degree in Electrophysics.

Publication List ：

[Refereed Journals]

[1] **P. I. Lin**, C. W. Luo, H. S. Liu, S. F. Chen, K. H. Wu, J. Y. Juang, T. M. Uen, Y. S. Gou, and J.-Y. Lin "On the origin of photogenerated terahertz radiation from current-biased superconducting $YBa_2Cu_3O_7$ thin films", J. Appl. Phys. **95**, 8046 (2004).

    ※selected in Virtual Journal of Applications of Superconductivity, volume **7**, Issue 2, June 15, 2004.

    ※selected in Virtual Journal of Ultrafast Science, volume **3**, Issue 7, July, 2004.

[2] **P. I. Lin**, K. H. Wu, J. Y. Juang, J.-Y. Lin, T. M. Uen, and Y. S. Gou, "Free-space electro-optic sampling of terahertz radiation from optically excited superconducting $YBa_2Cu_3O_7$ thin films", IEEE Trans. Appl. Supercond. **13**, 20 (2003).

[3] **P. I. Lin**, C. W. Luo, H. S. Liu, K. H. Wu**,** J. Y. Juang, T. M. Uen, and Y. S. Gou, "Bipolar photogenerated terahertz radiation in biased photoconductive switches", Physica B **329-333**, 1651 (2003).

[4] T. Y. Cheng, **P. I. Lin**, S. F. Chen, S. J. Liu, J. Y. Juang, J.-Y. Lin, K. H. Wu, T. M. Uen, Y. S. Gou, R. L. Wang, and H. C. Li, "Superconducting $NdBa_2Cu_3O_7$ thin films grown on bare (1-102) sapphire by pulsed laser deposition", J. Low Temp. Phys. **131**, 557 (2003).

[5] S. F. Chen, **P. I. Lin**, J. Y. Juang, T. M. Uen, K. H. Wu, Y. S. Gou, and J. Y. Lin, "Metallic percolation in $La_{0.67}Ca_{0.33}MnO_3$ thin films", Appl. Phys. Lett. **82**, 1242 (2003).

[6] **P. I. Lin**, S. F. Chen, K. H. Wu, J. Y. Juang, T. M. Uen, and Y. S. Gou, "Characteristics of photogenerated bipolar terahertz radiation in biased photoconductive switches", Jpn. J. Appl. Phys. **41**, L1158 (2002).

[7] H. Chou, **P. I. Lin**, C. C. Hsu, and T. C. Chow, M. T. Hong and Y. C. Chen, J. R. Liu, and T. P. Tsai "Polishing effect of the plasma on the growth of $YBa_2Cu_3O_7$ films by radio frequency sputtering", J. Vac. Sci. Technol. A **20**, 441 (2002).
　　※selected in Virtual Journal of Applications of Superconductivity, volume 2, Issue 5, March 1, 2002.

[8] K. H. Wu, **P. I. Lin**, C. C. Hsieh, S. J. Liu, J. Y. Juang, T. M. Uen, J.-Y. Lin, and Y. S. Gou, "Superconducting YBCO films grown on TiO_2 buffer layers derived from various processes", Physica C **363**, 119 (2001).

[9] **P. I. Lin**, C. W. Liu, C. C. Hsieh, K. H. Wu, J. Y. Juang, T. M. Uen, J.-Y. Lin, Y. S. Gou, "Characteristics of YBCO thin films deposited on substrates buffered by various TiO_2 layers", Jpn. J. Appl. Phys. **40**, L377 (2001).

[Conference Papers]

[1] **P. I. Lin** *et al.*, "On the origin of photogenerated terahertz radiation from current-biased superconducting $YBa_2Cu_3O_7$ thin films" 2004 年美國物理年會 in Canada, March (2004).

[2] **P. I. Lin** *et al*., "On the origin of photogenerated terahertz radiation from current-biased superconducting YBa$_2$Cu$_3$O$_7$ thin films" 2004 年中華民國物理年會, February (2004).

[3] **P. I. Lin** *et al*., "Characterization of Photogenerated Terahertz Radiation in High-*Tc* Superconductors", 2003 CLEO Pacific Rim in Taiwan, December (2003).

[4] **P. I. Lin** *et al*., "Free-space electro-optic sampling of terahertz radiation from optically excited superconducting YBa$_2$Cu$_3$O$_7$ thin films" 2003 年中華民國物理年會, February (2003).

[5] **P. I. Lin** *et al*., "Bipolar Photogenerated Terahertz Radiation in Biased Photoconductive Switches" The 23rd international conference on Low Temperature Physics in Japan, August (2002).

[6] T. Y. Cheng, **P. I. Lin** *et al*., "NdBa$_2$Cu$_3$O$_{7-\delta}$ Superconducting Films on Sapphire for Microwave Devices" 2002 International Conference on Physics and Chemistry of molecular and Oxide Superconductors in Taiwan, August (2002).

[7] **P. I. Lin** *et al*., "High Critical Current Density YBa$_2$Cu$_3$O$_{7-\delta}$ Thin Films Deposited on SrTiO$_3$ Buffered MgO Substrates by Pulsed Laser Ablation" 2002 年中華民國物理年會, February, (2002).

[8] C. C. Hsieh, C. W. Liu, **P. I. Lin** *et al*., "Characterization of TiO$_2$ Thin Films Deposited by Various Processes" 光譜技術與表面科學研討會, July (2001).

[9] **P. I. Lin** *et al*., "Fabrication of Grain Boundary Series Josephson Junction Array by Selective Epitaxial Growth" ISEC'01 國際超導電子研討會 in Japan, June (2001).

[10] K. H. Wu, **P. I. Lin** *et al*., "Preparation of Various TiO$_2$ Buffer Layers for YBa$_2$Cu$_3$O$_7$ Thin Films" 2001 年美國物理年會, March (2001).

[11] **P. I. Lin** *et al*., "Characteristics of YBa$_2$Cu$_3$O$_7$ Thin Films Deposited on Substrates Buffered by Various TiO$_2$ Layers" 2001 年中華民國物理年會, February (2001).